INVESTIGATION OF THRUST MECHANISMS IN A WATER FED PULSED PLASMA THRUSTER

DISSERTATION

Presented in Partial Fulfillment of the Requirements for
The Degree Doctor of Philosophy in the Graduate
School of The Ohio State University

By

Carsten A. Scharlemann

****

The Ohio State University
2003

Dissertation Committee:

Professor Thomas M. York, Adviser

Professor Michael G. Dunn

Professor James N. Scott

Approved by

Adviser

Aeronautical and Astronautical Engineering Graduate Program

ABSTRACT

Analytic models predict the possibility of extending the range of performance parameters of Pulsed Plasma Thrusters (PPT) by using propellants other than the traditionally used Teflon. A theoretical and experimental effort was initiated at The Ohio State University to investigate the use of alternative propellants for PPT. Analytical and numerical calculations (MACH2) indeed indicate a significant broadening of the obtainable range of specific impulse and thrust-to-power ratios when alternative propellants such as lithium or water are utilized. Consequently, in an effort to investigate changes in physical phenomena and thruster performance experimentally, a hybrid thruster was designed and built, facilitating the use of alternatively water or Teflon. The thruster design includes a unique water propellant feed system, allowing the supply of the water propellant without detrimentally affecting the inherent simplicity of the PPT system.

The thruster operation and performance was investigated by several different diagnostic methods, including current and voltage measurements, Langmuir probes, and magnetic field probes. Furthermore, impact pressure measurements in the plume of the thruster allowed new insight into the plume structure and the accurate evaluation of impulse bits. Employment of the diagnostic methods for Teflon and water propellant enabled the unambigous identification of propellant related effects such as reduced electron temperature and higher exhaust velocites in the case of water propellant.

The electromagnetic nature of the water thruster was clearly identified. For 30 J discharge energy, the water thruster requires only 5% of the mass bit of a Teflon thruster to produce an impulse bit 30% of the magnitude of the Teflon thruster, suggesting greatly increased propellant efficiencies. In agreement with the plasma diagnostic results, a specific impulse for the water thruster of up to 8000 s and efficiencies of up to 16% were evaluated.

To my parents, for their support and love.

ACKNOWLEDGMENTS

This dissertation was only made possible thanks to the help of many people. Foremost I wish to thank Dr. Thomas York for his guidance and encouragement throughout this research effort. I would also like to thank my Committee members Dr. Dunn, Dr. Turchi, and Dr. Scott for their assistance and support.

The assistance of the staff of the Aeronautical and Astronautical Research Laboratory is gratefully acknowledged. Special thanks go to Tom Veit, Jeff Barton, Ken Cobley, and Cathy Luckhaupt. I would also like to thank Sandy Rhoads for the great help and support she gave me.

Very much appreciated was the help from Eric Pencil and Dr. H. Kamhawi of the NASA Glenn Research Center for performing the impulse bit measurements and providing equipment. Also greatly appreciated was the help of Dr. P. Mikellides with the numerical work involving MACH2.

Many thanks also to Ron Corey for his friendship during his time at The Ohio State University. The numerous discussions we had were always a source of motivation. Very special thanks go to Shawn Ryan for her patience and her understanding.

VITA

June 24, 1968………………………………	Born – Stuttgart, Germany
June, 1988 …………………………………	Abitur (B.S.), Königin-Katharina Stift, Stuttgart, Germany
April 1996 – November 1996……………..	Research Assistant, I. Physikalisches Institut, Giessen, Germany
November 1996……………………………	Diplom Ingenieur (M.S.) Technische Universität of München, Germany
February 1996 – August 1998……………....	Research Assistant Technische Universität of München, Germany
September 1998 – present.…………………	Research Associate The Ohio State University, Columbus, Ohio, USA

PUBLICATIONS/ CONFERENCE PAPERS

[1] “Pulsed Plasma Thruster Using Water Propelllant, Part I: Investigation of Thrust Behavior and Mechanism” C. A. Scharlemann, T.M. York, AIAA-03-5022, 39^{th} AIAA Joint Propulsion Conference, Huntsville, Alabama, July 2003

[2] “Pulsed Plasma Thruster Using Water Propelllant, Part II: Thruster Operation and Performance Evaluation” C. A. Scharlemann, T.M. York, AIAA-03-5022, 39^{th} AIAA Joint Propulsion Conference, Huntsville, Alabama, July 2003

[3] "Investigation of a PPT Utilizing Water as Component Propellant", C.A. Scharlemann, T.M. York, IEPC-03-112, International Electric Propulsion Conference, March 2003, Toulouse, France

[4] "Theoretical and Experimental Investigation of C_{60}-Propellant for Ion Propulsion". C. A. Scharlemann, Acta Astronautica, Vol. 51/12, pp 865-872, Nov. 2002

[5] "Alternative Propellants For Pulsed Plasma Thrusters", C.A. Scharlemann, T.M. York, P.J. Turchi, AIAA-2002-4270, 38th AIAA Joint Propulsion Conference, July 2002, Indianapolis, Indiana

[6] "Pulsed Plasma Thrusters Variations for Improved Mission Capabilities", C.A. Scharlemann, R. Corey, I.G. Mikellides, P.J. Turchi, P.G. Mikellides, AIAA-00-3260, 36th AIAA Joint Propulsion Conference, July 2000, Huntsville, Alabama

[7] "Very Long Range Exploration by Means of Electric Propulsion and Cometary Resource Utilization", P.J. Turchi, C.A. Scharlemann, IEPC-99-189, International Electric Propulsion Conference, Oktober, 1999, Japan

[8] "Von Mikrometeoriten zur Prozessorientierten Einpulstechnik" ("From Micrometeorites to the One-Pulse-Technology for Surfacetreatment"), E. Igenbergs, B. Dirr, M. Rott, F. Hepp, R. Graf, K. Kolbeck, C. A. Scharlemann Deutscher Luft- und Raumfahrtkongreß, München, 14-17 Oct., 1997, DGLR

FIELDS OF STUDY

Major Field:	Aeronautical and Astronautical Engineering
Specialization:	Propulsion and Power
Special Emphasis:	Electric Propulsion and High Temperature Gasdynamics

TABLE OF CONTENTS

LIST OF TABLES

LIST OF FIGURES

CHAPTER 1

INTRODUCTION

The various missions accomplished in the initial years of space exploration, e.g. earth-to-orbit flights and the manned moon missions, utilized mainly high thrust propulsion systems. For these kinds of missions, chemical propulsion systems were and are the appropriate choice. However, with increasing (Δv) requirements for missions following these early ones, it became increasingly important to lower the mass of the spacecraft in order to keep the mission cost and mission duration low. Since the propellant mass of a spacecraft employing a chemical propulsion system is a driving part of the mass budget, it was an obvious path to investigate propulsion systems with higher exhaust velocities and therefore higher propellant utilization efficiencies than chemical propulsion systems.

At this point in time the new concept of electric propulsion emerged. Propellant utilization efficiency is in general a function of the obtainable exhaust velocities of the utilized propulsion system. Exhaust velocities in chemical propulsion systems are mainly limited by the amount of chemical energy stored in the propellant and the conversion efficiency of the chemical energy into kinetic energy. To circumvent the energy content limitation of the chemical propellants, the concept of electric propulsion was introduced.

A general definition of the electric propulsion concept is given by Jahn[1]:

> *The acceleration of gases for propulsion by electrical heating and/or by electric and magnetic body forces.*

The physical concepts of electric propulsion had been recognized by R.H. Goddard as early as 1906 and were further outlined by H. Oberth in 1929 in his classic book on rocketry and space travel. Thanks to these and other visionaries, a whole family of electric propulsion system exists nowadays. In general, one distinguishes three different general propulsion concepts:

- Electrothermal
- Electromagnetic
- Electrostatic

All three of those concepts have a large number of derivatives, employing different concepts to generate and accelerate the plasma. Table 1.1 summarizes the performance parameters of some of the most important flight systems.

The present work is dealing with one member of the electromagnetic group, the Pulsed Plasma Thruster, usually abbreviated as PPT. The general concept of a breech-fed parallel-plate PPT is remarkably simple, as illustrated in Fig. 1.1. Two parallel electrodes constitute the acceleration channel. They are connected to a power storage unit and high

Concept	Specific impulse [s]	Input power [KW]	Thrust/Power [mN/kW]	Specific mass [kg/kW]	Propellant
Resistojet	269	0.5	743	1.6	N_2H_4
	299	0.9	905	1	N_2H_4
Arcjet	480	0.85	135	3.5	NH_3
	502	1.8	138	2.5	N_2H_4
	>580	2.17	113	2.5	N_2H_4
	800	26	N/A	N/A	NH_3
PPT	847	<0.03	20.8	195	Teflon
	1200	<0.02	16.1	85	Teflon
Hall	1600	1.5	55	7	Xenon
	1638	1.4	N/A	N/A	Xenon
	2042	4.5	55.3	6	Xenon
Ion	2585	0.5	35.6	23.6	Xenon
	2906	0.74	37.3	22	Xenon
	3250	0.6	30	25	Xenon
	3280	2.5	41	9.1	Xenon
	3400	0.6	25.6	23.7	Xenon

Table 1.1: Performance parameters of selected electric propulsion flight systems[2]

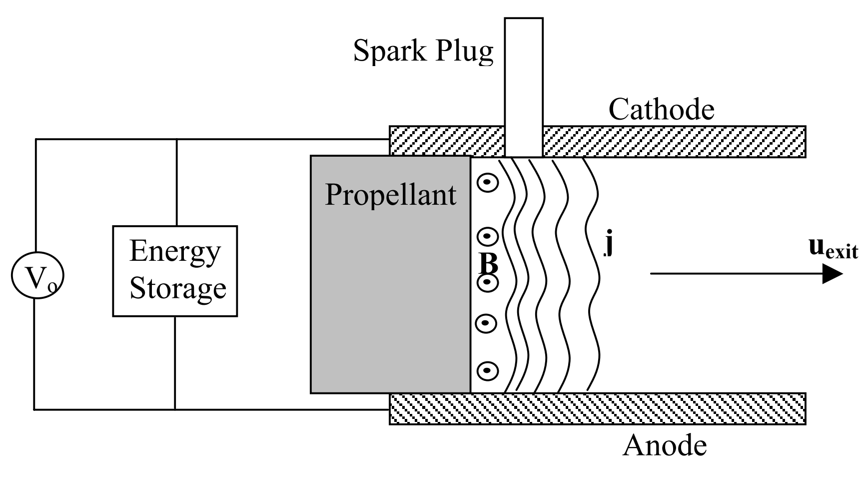

Fig. 1.1: Schematic of a Pulsed Plasma Thruster and its functional principle

voltage power source. The propellant, in general a solid block of polymer (traditionally polytetrafluroethylene (PTFE) also known as Teflon), is positioned between the two electrodes. After charging the power storage, a breakdown between the electrodes is initiated by means of a spark plug or a similar device. The breakdown occurs at a location of minimum inductance, namely in the vicinity of the polymer surface. Subsequently, a minuscule amount of propellant (typically in the range of several μg) is ablated from the surface. The discharge simultaneously dissociates and ionizes the propellant. Transforming the propellant into a plasma allows the acceleration of it by means of the Lorenz force (j x B) created by the self-induced magnetic field, B, interacting with the discharge current. The breech-fed, parallel-rail configuration is only one of many investigated in the last four decades. Others developments include the side-fed rectangular and the coaxial side- and breech-fed configurations.

The structural simplicity of the Pulsed Plasma Thruster was the reason that in 1964 a PPT was the first electric propulsion system ever flown on a spacecraft (Zond 2). Since then, numerous satellites equipped with PPTs have been flown, including the LES-6 (Lincoln Experimental Satellite)(see references below), the Synchronous Meterological Satellite[3,4] (SMS), the TIP/NOVA[5,6] (TRANSIT Improvement Program consisting of three spacecrafts with PPTs onboard), and most recently the Earth Observer-1 Satellite[7].

The frequent utilization of PPTs was mainly driven by their simplicity, robustness, and simply the fact that this system was space qualified. However, in comparison with other electric propulsion systems, PPTs suffer from a very low thruster efficiency of around 5-12 %. Parallel to the extensive flight experience gained with PPTs, they were the objects of intensive research, both theoretical and experimental. The main objectives of this research were to gain a better understanding of PPTs in general and to investigate the sources of the poor thruster efficiency.

CHAPTER 2

APPROACH

Simple analytic models predict the potential for performance improvements in PPTs by utilizing propellants with lower average molecular/atomic weight than the traditionally used Teflon. At The Ohio State University numerical and experimental efforts were initiated to investigate the validity of these predictions.

The numerical calculations were performed by invoking the $2^1/_2$ dimensional magnetohydrodynamic code, MACH2 (Chapter 4). These calculations included several propellant candidates covering a wide range of average molecular/atomic weight: Cesium, Teflon, water, and Lithium. MACH2 confirmed the general trends given by the analytic models, namely higher specific impulses and therefore higher efficiencies for decreasing molecular/atomic weight and higher thrust-to-power ratios (lower efficiencies) for increasing molecular/atomic weight and vice versa.

Encouraged by these results, experimental efforts were initiated to investigate the possibility of using water as propellant for a PPT. The decision to use water was initially predominately driven by practicability issues such as availability and the non-toxic property of water.

The main objectives of the experiment were to investigate changes in physical phenomena and thruster performance induced by the nature of the propellant. An entirely new vacuum and diagnostic facility was assembled for these experiments (Chapter 5).

Additionally, a laboratory PPT was designed, able to use Teflon or alternatively water without requiring major modification of the thruster geometry or circuitry (Chapter 5). This hybrid nature facilitates an unambiguous comparison of the physical phenomena and thruster performance changes induced by the different nature of the propellants.

Diagnostic methods included basic current and voltage measurements, Langmuir probe measurements, impact pressure measurements and magnetic field measurements (Chapter 6 and 8). The successful introduction of pressure probe measurements for PPT research permits not only new insight into the thrust mechanism of a PPT, but also constitutes a convenient method to evaluate performance parameters like the specific impulse.

Analytic models were implemented for a better understanding of the experimental observation. Thruster performance was evaluated by using experimental data and subsequently correlated to thrust stand measurements (Chapter 9)

CHAPTER 3

BACKGROUND

A concise summary of the research conducted over the last four decades will be presented in this chapter. Due to the scope of PPT research it is not intended to present every single direction of existing research, but rather to focus on systems somewhat related to the one utilized in the present work (parallel-plate PPT). This chapter is divided into three subchapters, the first describing the general research on parallel-plate PPTs. The successive chapters will then summarize the investigation of the utilization of solid propellants other than the standard Teflon and PPTs utilizing gaseous propellants, the so-called Gas-Fed PPTs, and fluid propellant PPTs. Finally, a short summary of the potential benefits of water as propellant is given.

3.1 General PPT Research

Guman and Peko[8] reported on efforts with both parallel-rail and coaxial electrodes for a range of discharge energies between 1 and 40 J. For both configurations a linear dependency of the specific impulse to the discharge energy has been verified, indicating a predominately electromagnetic acceleration of the propellant (in contrast to a change of specific impulse with the square-root of the discharge energy, indicating a predominately thermodynamic acceleration). Efforts to increase the specific impulse of the coaxial thruster with an expansion nozzle failed. It was shown that the shorter the nozzle, the higher the specific impulse of this device.

Several studies were conducted with the LES-6 PPT and derivatives of it. Vondra, Thomassen, and Solbes[9] used the LES-6 thruster operating at 1.85 J and measured an ion velocity in the exhaust gas of 40 km/s. Based on the measured ablation rate and the impulse bit, they concluded that less than 10% of the ablated mass was electromagnetically accelerated while the major part was gas dynamically accelerated. An analysis of the circuit elements revealed that only 3% of the total discharge energy went into kinetic energy while the rest was dissipated in the capacitor or lost in other various sinks.

Modifying the LES-6 PPT such that the propellant can be fed from both sides instead of the conventional way of feeding it from the back (breech-fed), Vondra and Thomassen[10] investigated the effect of variations in geometry. By adjusting the distance between the two fuel faces they were able to control the ablated mass. Performance measurements and calculations showed the existence of a well-distinguished optimum of specific impulse and thrust with regard to the mass consumption. In comparison with the breech-fed configuration, they slightly improved the performance with regard to the efficiency, impulse bit, and specific impulse. However, strong and inhomogeneous ablation of the fuel faces was observed after a relatively short time. The effects of this carbonization on their measurements of impulse bit and specific impulse have not been discussed.

Solbes and Vondra[11] investigated the influence of the electric circuit elements (capacitance, voltage, inductance, and resistance) on the thruster performance by developing semiempirical relationships. They confirmed the general notion that the impulse bit and mass bit are proportional to the discharge energy, therefore the specific impulse and efficiency is independent of the capacitor voltage. Mass bit and thrust are decreasing with increasing circuit resistance, inductance, and capacitance (with the circuit resistance as the dominant factor). However, increasing the inductance and capacitance increases the specific impulse (for the same discharge energy), with the circuit resistance having only minor effects.

A further study of the influence of electrode geometry on thruster performance was conducted by Palumbo and Guman[12]. Their PPT system was unique with regard to the discharge energies up to 450 J. Increasing the spacing between the electrodes, they observed a monotonic decrease of the thrust to power ratio, but an increase in specific impulse. Measuring the effects of an included angle between the electrodes on efficiency, specific impulse, and thrust to power ratio, they found the existence of an optimum angle. They reported efficiencies of up to 53% and a specific impulse of more than 5000 s. Those results were never verified by other groups.

In an effort to investigate the poor propellant utilization efficiency, Spanjers et al.[13] conducted interferometric and broadband emission measurements of the plume. They found neutral gas evaporating for at least 300 μs after the main discharge. A first estimation of the neutral density suggests that these neutrals are the source of the propellant inefficiency. A parametric study showed that increasing the discharge energy does not increase the propellant utilization efficiency, however, due to increased velocities of the fast ions, the total efficiency of the thruster improves with increased discharge energy. Furthermore, observations of increased electron density while decreasing the capacitance (for the same energy, requiring higher voltages) implied that a decrease in capacitance can improve the propellant efficiency.

A further contribution to the propellant inefficiencies due to particulate emissions was investigated by Spanjers et al.[14]. Collecting the plume contents on witness plates and subsequently analyzing them with the combination of a scanning electron microscope with energy dispersive x-ray analysis and microscopic imaging, they found Teflon particulates ranging in size from 1 μm to 100 μm. Estimations suggest that the particulate emission can be up to 40 % of the total propellant consumption while they contribute less than 1% to the total thrust.

Arrington[15] investigated the possibility of improving performance by varying the electrode geometries. The parametric study was done by keeping the electrode gap at a constant value of 3.81 cm and varying only the length of the electrodes and their flare angle. Measurements were done at various energy levels ranging from 5 to 54 J.

Summarizing the results: At a discharge energy of 43 J, they found that increasing the length of the electrodes from 2.54 cm to 3.81 cm increased the efficiency (9.5% instead 9.0%) but not the thrust to power ratio (16.1μN-s/J instead of 16.9μN-s/J). An additional electrode flare angle of 20° resulted in an improvement of the thrust to power ratio (17.1μN-s/J) and further increase of efficiency (10.3%).

In order to better understand the mechanism of late time propellant evaporation, Spanjers et al.[16] investigated how they relate to parameters like the discharge duration and power level (Spanjers et al., 1998). Since it was hypothesized that the level of late time evaporation is linked to the temperature of the Teflon bar, its temperature at several locations inside the bar was measured. The result showed that the temperature rose when the thruster was operated at increased power levels or the total length of the propellant bar was reduced. In both cases the propellant consumption rate increased without increasing the thrust, therefore lowering the (calculated) quantities like specific impulse and efficiency. Calculations of the potential propellant savings for lower temperatures of the Teflon bar showed propellant savings of 25% by reducing the temperature from 130°C to 40°C.

In an effort to utilize the late time evaporation, Okada et al.[17] investigated a "double discharge method". It was hypothesized that a second discharge utilizes the otherwise lost amount of propellant evaporating after the main discharge. The thruster was equipped with two capacitors, one for each discharge. The performance of the thruster was measured as a function of the ratio of capacitance of those two capacitors

(4/0, 3/1, 2/2, and 1/3) and the delay time (5, 100, and 1000 μs) between the two discharges. A capacitor ratio of 2/2 with a delay time of 5 μs resulted in the best performance. However, it was not clear if this performance improvement was due to a efficient use of late time evaporation or, since the two discharges with such a short delay time are basically the same as one discharge, simply due to the increased total discharge energy.

A Herriott Cell Interferometer diagnostic was developed by Antonsen et al.[18] with the objective to measure the plume electrode and neutral density, in particular the neutral density after termination of the discharge. Utilizing a Herriottt Cell they were able to focus a large number of laser beams in a relative small volume of the plume, therefore achieving a resolution a factor of about 10 higher than compared to a single-pass interferometer. Measurement of the neutral particle density 20 μs after discharge termination measurements showed a neutral particle density of 3 x 10^{21} m^3, increasing linearly with time to almost 7 x 10^{21} m^3 at 200 μs after discharge termination. The estimated total mass of neutral particles was about 1/8 of the average mass loss per discharge of the utilized thruster. However, this was based on a low estimated average thermal velocity of 300 m/s.

Antonsen et al.[19] developed a microsecond timescale surface temperature method to measure accurately the Teflon ablation surface shortly after the termination of the discharge. Utilizing a micro-pulsed plasma thruster (8 J discharge energy) they measured Teflon surface temperature of nearly 600°C about 20 μs after the discharge. The temperature decreased with time and at 90 μs after the discharge was reduced to only 100°C.

3.2 Alternative Propellants for PPTs

The above section dealt nearly exclusively with the effort to improve PPT performance by changes in thruster geometry, electric circuits, variation of discharge operation, etc. It is clear from the summary above that, although major improvements in understanding of PPTs in general and the poor thruster efficiency in particular have been achieved, it did not translate into a significant improvement of thruster performance. One additional possibility for performance improvements has been excluded so far: the utilization of propellants other than the standard Teflon.

One of the first publication to mention the notion of alternative propellants was Palumbo and Guman[12]. They investigated two general possibilities: (i) replacement of the Teflon with other thermoplastics like Celon, Halar, Tefzel and unsintered Halon, and (ii) Teflon sintered with 10% and 30% of LiOH and InBr. All of the alternative thermoplastics produced a lower thrust to power ratio than Teflon and specific impulses close to the ones obtained with Teflon. The LiOH tests showed a strong decrease in impulse bit during the test. Several tests lead to the conclusion that a high resistance compound is precipitating out on the electrodes from the propellant, thereby decreasing the amount of energy coupled into the plasma with time. Furthermore, the performance measurements with the InBr sintered Teflon showed no significant increase in performance.

Leiweke et al.[20] explored the possibility of multi-material propellants for Pulsed Plasma Thrusters. The basic idea was to utilize materials with lower average molecular weight to increase the specific impulse. However, since the investigated high density polyethylene (HDPE) does not have the necessary voltage hold-off strength, an arrangement of alternating layers of plastics and Teflon instead of a uniform Teflon bar was developed. During the conducted experiments carbonization of the HDPE was observed while the Teflon ablated in regular fashion. This resulted in a lower ablation rate and consequently in lower impulse bits and efficiencies. The difference in thermal conductivity of the Teflon and the HDPE was suggested to be the reason for these observations.

Pencil et al.[21] compared the performance of nominal Teflon with a high-density, a porous, and a carbon-impregnated Teflon propellant. The impulse bit for all of these propellants agreed within ±10%. The efficiency for the nominal and the high density Teflon were about the same (6-13%), however the 2% carbon-impregnated propellant provided efficiencies up to 18%. Examination of the experimental results showed that while the ablation rate changed with the propellant porosity, the thrust did not. It was suggested that the degree of porosity influences propellant losses like macroparticle ejection and late time evaporation. In general, the lower the density of the Teflon, the higher the ablation rate, and Teflon with higher carbon contribution tends to have premature discharges and high shot-to-shot variation.

3.3 Gas-Fed and Liquid Propellant PPTs

Gas-fed thrusters, other than the PPTs operating with a solid propellant like Teflon, require an active propellant feed and injection system. This significantly increases the complexity of the thruster; however it also promises higher thrust efficiencies and a broader range of propellant candidates. The potential efficiency increase is due to a better control of the mass bit (no late time evaporation or macro particle ejection) and the possibility to use propellants with lower average atomic or molecular weight.

Ziemer, Choueiri, and Birx[22] experimentally investigated the influence of the capacitance on the performance of a coaxial gas-fed Pulsed Plasma Thruster (GFPPT). GFPPTs have significant differences from a standard, solid propellant coaxial PPT: The argon propellant is fed into the thruster via a mechanical valve. Since those valves have opening times of several milliseconds, a train of six pulses, with a total discharge time between 3-5 μs, is fired per trial instead of only one like in a standard PPT. The train of discharges is synchronized with the mass pulse (valve open) such that the majority of the propellant is utilized, assuring high propellant utilization efficiencies. The thruster is controlled by an all-solid-state modulator in order to achieve this discharge behavior. Two capacitances were investigated, 94 μF and 180 μF with charging voltages of 330 V and 240 V respectively. Total discharge energy was 5 J. While experimental investigations show an increase in thrust efficiency (up to 69%) and specific impulse (up to 19,000 s) for increasing capacitance, it is lower than predicted by simple analytic models. Comparisons of the experimental trends with a more sophisticated one-dimensional model suggest that the reason for their observation is that due to the increased capacitance, the discharge reaches the edges of the electrodes before the capacitor is fully discharged.

A comparison between a coaxial and parallel-plate GGPPT was conducted by Ziemer et al.[23]. Furthermore, since simple analytic models predict a strong influence of the inductance-per-length, L', experiments were conducted to investigate the impact of this parameter. Inductance-per-length values between 280 nH and 565 nH were achieved by changing the electrode geometry ($L' \approx \mu_o H/W$, with H and W the electrode gap and width respectively). The electrode length for the parallel-rail GFPPT was about 10 cm and the thruster discharge energy was 2 and 4 J. The different configurations were tested with argon and water propellant. The electromagnetic model of acceleration predicts increased performance with increasing L' values; however the experimental data contradicts those predictions. As a result the coaxial configuration performed in general slightly better than the parallel-rail configuration, although the latter exhibits the higher inductance-per-length. It was shown that for the parallel-rail configuration a 1:1 ratio of electrode gap and width performed best. It is suggested that both of these results are due to increased wall losses when confining the discharge area above a certain level. The water propellant has proven to result in higher thruster efficiencies (up to nearly 20% for 2 J discharge energy) and for low mass bits also in higher thrust-to-power ratios (4 μN/W at a mass bit of about 0.5 μg).

A comparison between a gas-fed PPT using water and argon was conducted by Ziemer and Petr[24]. Utilizing a rectangular parallel-plate gas-fed PPT , they investigated the thruster performance with both propellants as a function of the capacitance (63 - 130 μF), discharge energy (2-4 J), and mass bits (0.1 – 4.0 63 μg). They found that the efficiency scales linearly with the exhaust velocity, indicting that the gas-fed is an electromagnetic accelerator. The water propellant provided about 15 – 25% better efficiencies than the argon propellant. At the lowest mass bit, efficiencies close to 20% and specific impulse near 7000s were obtained. The improvement was suggested to be due to lower plasma resistance in the case of water. Furthermore a model of current sheet canting predicts improvement for lower average molecular weight propellants.

Koizumi et al.[25] investigated a liquid propellant PPT. The water propellant was in injected in liquid form by means of ink-jet type mechanism. Experimental evaluation of the thruster performance included variation of the mass bit (4 – 26 μg) and discharge energy (3 – 13.5 J). At discharge energies at the low end of the investigated range they observed a low discharge initiation probability of $<50\%$. Evaluation of the impulse bit by varying the mass bit showed that the first is nearly independent of the second. The specific impulse decreases approximately liner with increasing mass bit. For a mass bit of 4 μg and discharge energy of 13.5 J they measured a impulse bit of about 60 μNs and a specific impulse of roughly 1500 s.

Kakami et al.[26] extended the range of possible liquid propellants by including ethanol, methanol and buthanol. The utilized liquid propellant PPT was similar to the one investigated by Koizumi (Koizumi, 2003). Performance measurements showed only slight differences when compared to water propellant. High speed photography evaluated the injection time of the propellant to be between 1 ms for 3 μg to 4 ms for 40 μg. Analytic modeling showed that more than 80% of the retaining liquid propellant is in liquid form even 10 ms after injection.

3.4 The case for water

As discussed above, gas-fed PPTs allow control of the mass bit and thereby avoid the significant late time mass losses. Furthermore, by choosing the propellant and its average molecular/atomic weight, respectively, one can broaden and potentially improve the performance of PPTs. While many elements/materials offer lower molecular/atomic weight than Teflon, water has many other reasons justifying its use as propellant.

One attractive advantage of water is its multifaceted use. In manned systems, water is present in the environmental system, for direct use of the crew, and as a product of fuel cells. Sharing this water with the propulsion system would lead to a reduced system complexity and simplify logistics. The International Space Station produces waste water in an amount of 3 to 7 liters a day (depending on the size of the crew)[27]. This waste water could constitute a precious source of propellant (depending on its degree of pollution). Furthermore, the water could be shared with other propulsion systems relying on water as propellant[28,29].

In recent years water has been found to be far more abundant in our space system then initially believed. Water is a major component of comets, it is abundant in the Jovian system, and it was even found stored in permanent frost on Mars. A propulsion system using water as propellant would therefore amend many In-Situ-Resource-Utilization (ISRU) missions[30].

In the context of PPTs, water would allow utilizing the gas-dynamic component of the thrust efficiently by using suitable geometries of the acceleration channel. This is not possible with Teflon since it contains carbon, which, deposited on the side-walls, will lead to uncontrolled discharges or even short-circuit the thruster.

The above are only some rather general advantages of usage of water as propellant. The advantages of a usage of water always have to be considered with regard to the specific propulsion system and the mission. A detailed discussion of all the advantages with regard to various propulsion systems and possible missions would be beyond the scope of this work. However, further general advantages of water propellant are as follows:

- Water is nontoxic, nonflammable, nonvolatile, noncorrosive, nonpolluting (compatible with Space Shuttle Bay requirements)
- Available in virtually limitless quantity
- Very low cost
- Easy and cheap to handle
- Water propellant has a higher density than gaseous propellant and does not need high pressure vessels like a gaseous propellant; subsequently reducing the tank and structure mass (important for micro satellites)

- A exhaust plume containing no carbon reduces the danger of accumulation of a conducting layer on sensitive electric or optical equipment
- Long time storability

CHAPTER 4

NUMERICAL AND ANALYTIC EVALUATION OF PPT PERFORMANCE

4.1 Introduction

The most straightforward justification for the utilization of propellants other than Teflon for PPTs is expressed by the following equation for the thrust-to-power ratio:

$$\frac{T}{P} = \frac{2 \cdot \eta}{u_{exit}} \tag{4.1}$$

with the thrust T, the power P, the thruster efficiency η, and the exhaust velocity u_{exit}. Assuming that a system has the ability to transfer a certain amount of stored energy into kinetic energy, if follows that the exhaust velocities and the thrust-to-power ratio can be controlled by choosing the propellant with the appropriate molecular/atomic weight. This again, could increase the rather limited range of performance of PPTs significantly.

The average molecular weight of particles in the exhaust plume of a Teflon PPT was evaluated to be 31 g/mol[31]. Following the above reasoning, propellants with a lower average molecular weight than 31 g/mol should provide higher exhaust velocities and a better thruster performance. An effort was undertaken to investigate this correlation in more detail by developing an idealized analytical model for ablation and acceleration process[32,33,34]. Furthermore, the numerical magnetohydrodynamic code, MACH2, was invoked to evaluate how accurate the analytic model captures the subtleties of the complicated discharge and acceleration processes. Both methods were employed to calculate the performance of a PPT assuming for different kinds of propellant covering a wide range of molecular/atomic masses (see Table 4.1): water, Lithium, Cesium, and, for comparison purposes, Teflon. Both methods are presented in the following.

	Mass [amu]	1st ionization energy [eV]	2nd ionization energy [eV]	Thermal diffusivity [m^2/s]	Heat capacity [J/kgK]	Heat of Vaporization [J/kg]	Density [kg/ m^3]
Teflon®	100	92.2	280.9	$1.28*10^{-7}$	1250	$2.1*10^{6}$	2150
Water	18.02	40.8	75.9	$1.47*10^{-7}$	4179	$2.4*10^{6}$	997
Lithium	6.94	5.39	81.0	$4.44*10^{-5}$	3600	$2.1*10^{7}$	530
Cesium	132.9	3.89	27.1	$8.0*10^{-5}$	240	$5.1*10^{5}$	1870

Table 4.1: Material properties for the investigated propellants

4.2 Idealized Analytic Model

An idealized model was developed with the objective to model the complicated ablation and acceleration processes in PPTs. The core of this model is the assumption of the existence of two distinguished points in the flow of a PPT: A sonic point, adjacent to the propellant surface, and a magnetosonic point further downstream. By assuming a one-dimensional quasi-steady plasma flow with low ratios of thermal to magnetic pressure, (low β), it can be shown that a point in the flow, called the magnetosonic point, exists where the flow velocity equals Alfven's wave speed given by

$$u^* = v_A = \frac{B^*}{\sqrt{\mu \cdot \rho^*}} \tag{4.2}$$

with the density ρ, and the magnetic field B. Starred quantities refer to the magnetosonic point. Under the assumptions stated above, the conservation of mass, momentum and energy can be written like

$$\dot{m} = \rho^* \cdot u^* \cdot A \tag{4.3}$$

$$\dot{m} \cdot \frac{du}{dx} = j_y \cdot B_z \cdot A \tag{4.4}$$

$$\dot{m}\left(h + u\frac{du}{dx}\right) = -\frac{E \cdot A}{\mu} \cdot \frac{dB_z}{dx} \tag{4.5}$$

with the flow velocity u, the specific enthalpy h, the current density j, the constant channel area A, the constant electric field E, and x as the direction of the flow. Substituting B_z - given by Ampere's law - into the equation for conservation of momentum and integrating from stagnation point to the magnetosonic point results in an expression for the mass flow

$$2 \cdot \mu \cdot \dot{m} \cdot u^* = A\left(B_o^2 - B^{*2}\right) \tag{4.6}$$

Further substitution of the mass flow rate, given by the conservation of mass, into Eq. 4.6 shows the following proportionality between the magnetic fields at the magnetosonic point and at the stagnation point:

$$\frac{B^*}{B_o} = \frac{1}{\sqrt{3}} \tag{4.7}$$

where the index (o) refers to quantities at the stagnation point. Combining Eqs. 4.3 – 4.5 with this proportionality and substituting the flow velocity u* with Eq 4.2 allows expressing express the mass flow rate due to the magnetosonic condition as

$$\dot{m} = \frac{A \cdot B_o^2}{3 \cdot \mu \cdot u^*} = \frac{A \cdot \mu \cdot j^2}{3 \cdot d^2 \cdot u^*} \tag{4.8}$$

with the discharge current density j and d the gap between the electrodes. Integrating the conservation equation of energy from the stagnation point to the magnetosonic point results in

$$\dot{m} \cdot h_o + \frac{A(E \cdot B)_0}{\mu} = \dot{m}\left(h^* + \frac{u^{*2}}{2}\right) + \frac{A(E \cdot B)^*}{\mu} \tag{4.9}$$

In the additional limit of high magnetic Reynolds numbers at the magnetosonic point, we can write for the magnetosonic velocity

$$u^* = \sqrt{\frac{h^* - h_o}{\sqrt{3} - 1.5}} = 1.468\sqrt{2\Delta h} \tag{4.10}$$

Since

$$h^* - h_o = \Delta h \cong c_p \cdot T^* + (\varepsilon_i)^* \tag{4.11}$$

and if we assume that energy deposition to ionize dominates the contribution to thermal internal energy and p(dv)- work, i.e.

$$c_p \cdot T^* << \varepsilon_i \tag{4.12}$$

then u^*, the speed at the magnetosonic point, tends to remain fixed and proportional to Alfven critical speed

$$u_{crit} = \sqrt{2 \cdot \varepsilon_i} \tag{4.13}$$

and

$$u^* = 1.468 \cdot u_{crit} \tag{4.14}$$

We can therefore rewrite the mass flow rate

$$\dot{m} = \frac{\mu \cdot j^2}{4.404 \cdot d^2 \cdot u_{crit}} \tag{4.15}$$

Equation 4.15 implies that the mass flow rate, based on the magnetosonic condition, is a function of the material properties, the thruster geometry, and the operating current level. Similarly, we can express the mass flow rate in terms of conditions at the thermal sonic point adjacent to the propellant surface. Assuming steady state flow of an ideal gas, the mass flow rate based on sonic conditions can be written as a function of the pressure p_a and temperature T_a at the sonic point

$$\dot{m} = A \cdot p_a \cdot \sqrt{\frac{\gamma}{R \cdot T_a}} \tag{4.16}$$

where R is the specific gas constant. The conservation of momentum and energy relates the surface pressure p_s and surface temperature T_s to the condition at the sonic point with

$$p_a = \frac{p_s}{1+\gamma} \tag{4.17}$$

$$T_a = \frac{2 \cdot T_s}{1+\gamma} \tag{4.18}$$

substituting Eqs. 4.17 and 4.18 into Eq. 4.16, and setting the surface pressure equal to the equilibrium vapor pressure results in an expression for the mass flow rate based on the sonic point assumption

$$\dot{m} = A \cdot p_{eq} \sqrt{\frac{\gamma}{2(1+\gamma)R \cdot T_s}} \tag{4.19}$$

with

$$p_{vap} = C_1 \cdot e^{-\frac{C_2}{T_S}} \tag{4.20}$$

where C_1 and C_2 are material dependent constants that can be found empirically. By setting Eq. 4.15 and 4.19 equal, the propellant surface temperature can be calculated iteratively based on the magnetosonic and sonic conditions. The surface temperature can then be used as boundary condition to solve the heat equation and find the temperature distribution in the propellant slab.

Assuming an ideal square wave discharge current, then, according to the idealized model (Eq. 4.15), the required mass to sustain the discharge varies linearly with time. The depth of the heat flux from the plasma into the propellant scales as the square root of time (see Fig. 4.1). These two statements are equivalent to the two curves depicted in Fig. 4.2. Hereby is $d_{EV/DC}$ the thickness of the layer, which is elevated above decomposition-/evaporization- temperature and d_{EM} the equivalent to the amount of mass required by the discharge. At a certain time, in the following called the optimum pulse time t_{opt}, these two curves intersect with each other. If the current pulse ends before reaching this optimum pulse time, the temperature of a certain amount of propellant is elevated above evaporation/decomposition temperature. This part of gaseous propellant will thus exhaust at low thermal velocities and therefore minimally contribute to the impulse bit, thus degrading thruster efficiency. To utilize the propellant more efficiently the current pulse has to be adapted in magnitude and in duration to the material properties of the propellant.

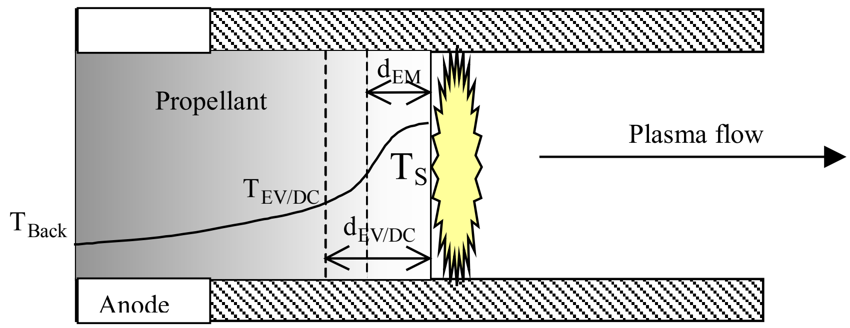

Fig. 4.1: Schematic of a PPT with the two depths $d_{EV/DC}$ and d_{EM}, the surface temperature T_S and evaporation/decomposition temperature $T_{EV/DC}$

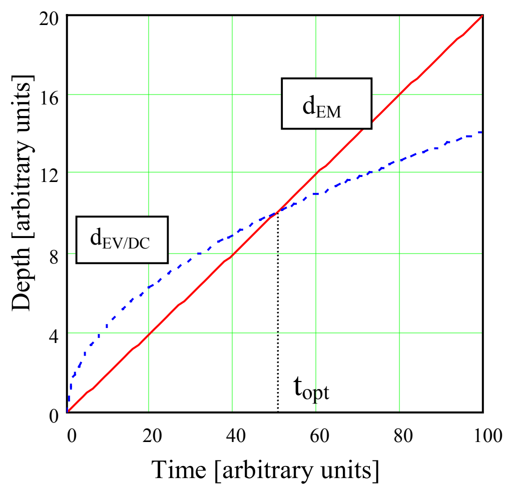

Fig. 4.2: Required depths to sustain the discharge and mass elevated above vaporization temperature

Based on the idealized model described above, a simple numerical code was developed to solve Eq. (4.19) for the surface temperature[33]. Based on this temperature, the temperature distribution in the propellant slab was evaluated and the optimum pulse times were calculated.

Using the optimum pulse times calculated thereby as input values, the full blown magnetohydrodynamic code MACH2 was employed in order to verify the idealized model and eventually refine the results. Along with a short introduction to MACH2, the results of these calculations are given in the next sections.

4.3 Introduction to the MACH2 Code

The processes during dissociation, ionization, and subsequent acceleration of the propellant are complicated and are closely related to the properties of the propellant. To investigate how well the idealized analytic model captures these processes and to evaluate the validity of the above discussed relation between molecular/atomic weight of various propellants, the numerical "Multiblock Arbitrary Coordinate Hydromagnetic" code (MACH2) was invoked. Consistent with the analytic model, these calculations included the four different propellants: water, Lithium, Cesium, and Teflon.

MACH2 was developed by the Center for Plasma Theory and Computation (Air Force Research Laboratories) and adapted by research groups at The Ohio State University for solving problems related to various propulsion systems. MACH2 is a 2 $^1/_2$ dimensional, time dependent, MHD code. Due to its Arbitrary-Lagrangian-Eulerian adaptive mesh and multi-grid diffusion systems, it is able to solve problems of complex geometries in plane-parallel of cylindrical symmetry. It is a single fluid, multi-temperature code employing real equation of state (EOS) and real viscosity effects. The code has been used successfully in the past to simulate various magnetohydrodynamic problems including compact toroids[35] and MPD thrusters[36]. Most recently new subroutines were added, allowing one to model the complex ablation processes occurring in ablation fed PPTs[37].

MACH2 permits inclusion of several features that cannot be captured by an analytic model. The results of the analytic model presented in Chapter 4.2 are based on a defined degree of ionization. Although MACH2 offers the possibility to define and fix the degree of ionization, it also provides the possibility to calculate the real degree of ionization through its extensive SESAME library of thermodynamic properties[35]. Both options, ideal gas assumption with fixed degree of ionization and real equation of state (EOS) models, were used since only the results of MACH2 gained with fixed ionization degrees allow a direct comparison with the results of the analytic models. The rigorous calculations, however, invoked the complete MACH2 capabilities with real EOS models.

4.4 Comparison of Numeric and Analytic Results

MACH2 calculations included several parameters such as exit velocity, mass flow rates, magnetic fields, electron temperature, etc. Of particular interest, with regard to a comparison between the numerical and analytic method, were the mass flow rates for the different propellants. Figs. 4.3 and 4.4 illustrate the mass flow rates of Teflon and water for a 30 kA discharge current.

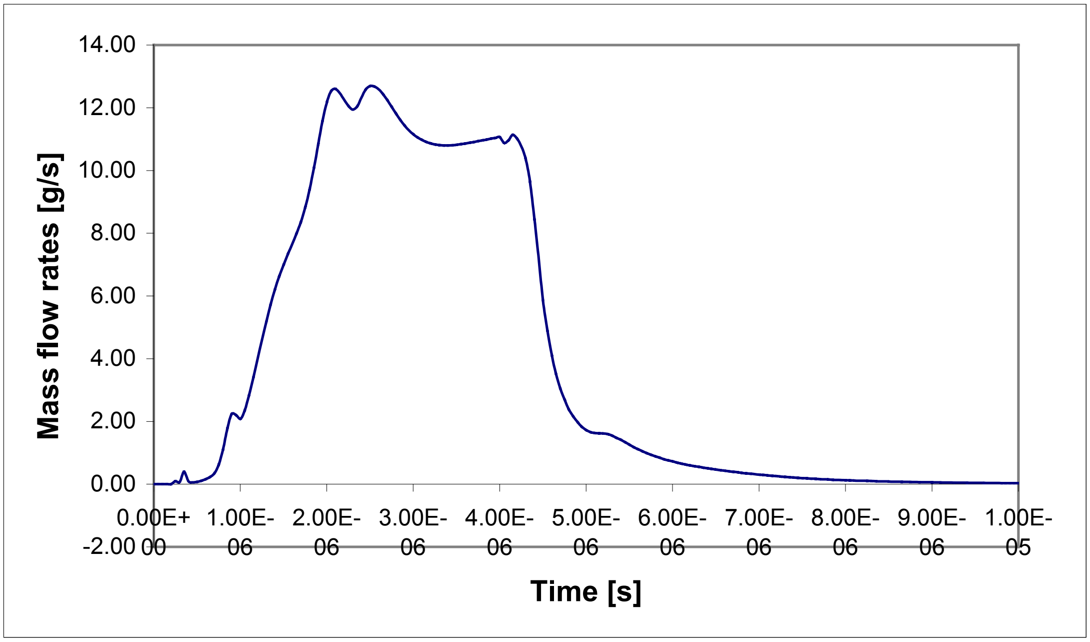

Fig. 4.3: Mass flow rate across the boundaries of the computational domain (MACH2) for Teflon, 30 kA square discharge current, with a 4 μs pulse width

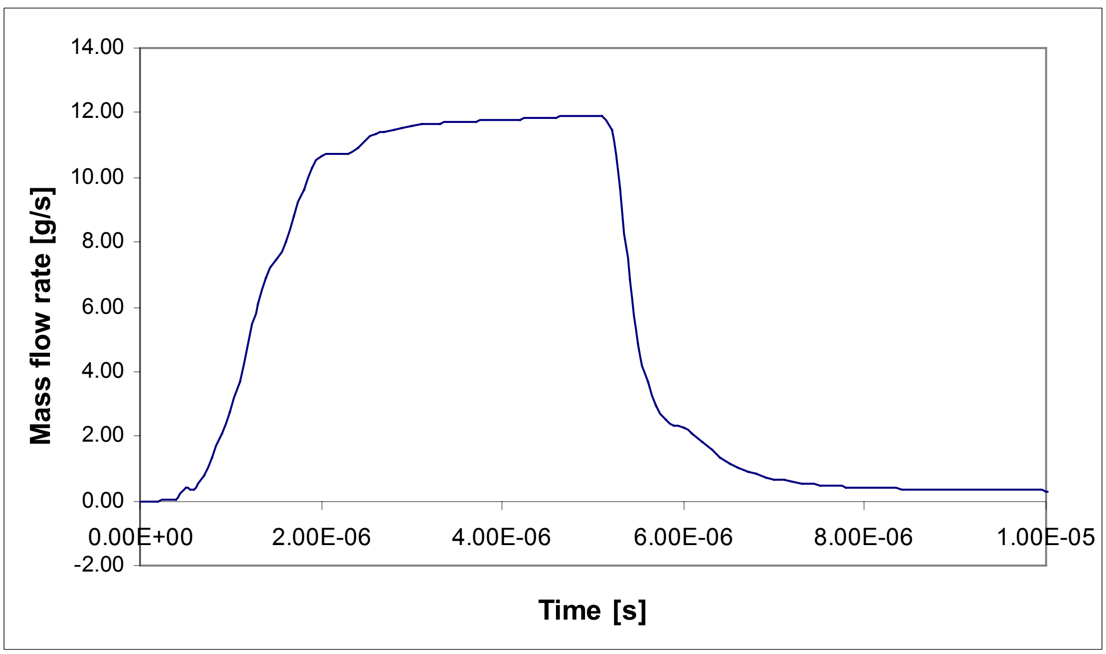

Fig. 4.4: Mass flow rate across the boundaries of the computational domain (MACH2) for water, 30 kA square discharge current, with a 5 μs pulse width

Table 4.2 compares the results for exhaust velocities and mass flow rates as obtained with the analytic model and MACH2. The values given in Table 4.2 were obtained for a square current waveform of 30 kA magnitude. Integer values for the degree of ionization, Z, as given in the first column, indicate a fixed degree of ionization, while non-integer values indicate MACH2 calculations employing the EOS model.

Comparing the results in Table 4.2, it is evident that although some results of the idealized analytic model agree well with MACH2 results, others are several factors off. Analysis of the results uncovered the following relation between cases for which the results of the two methods agreed, and those where they did not agree: In all the cases where the results did not agree it was found that the energy deposition into thermal modes was larger than the specific ionization energy, contradicting one of the central assumptions in the analytic model (Eq. 4.12). In general it was found that the overall idealized model scaling with Alfven critical velocity is valid as long as the specific ionization energy $\varepsilon_i \sim c_p T$ or better, $\varepsilon_i > c_p T$ (see Tables 4.2 and 4.3).

Calculation of the thrust-to-power ratios and specific impulses based on the results of the idealized analytic model and the MACH2 results illustrates the impact of the failure of the assumptions that the change in enthalpy between the sonic and the magnetosonic point is dominated by the ionization energy. Figs. 4.5 and 4.6 show the thrust-to-power ratio as a function of the specific impulse, based on the results of the idealized analytic model, and based on the MACH2 calculations, respectively. In general, for cases where the assumption of $\varepsilon_i / (c_p T) > 1$ failed, MACH2 results (see Fig. 4.6) indicate higher velocities at the magnetosonic point and thus higher specific impulse values and lower thrust-to-power ratios than predicted by the idealized model (see Fig. 4.5).

	$\dot{m}$ [kg/s]		u^* [km/s]	
	MACH2	IM	MACH2	IM
Teflon (Z=1)	--	0.019	--	19.6
Teflon (Z=2)	--	0.011	--	34.1
Teflon (Z=2.1)	0.0115	--	31.5	--
H_2O (Z=1)	0.0118	0.012	29.3	30.6
H_2O (Z=2)	0.0094	0.009	40.2	41.8
H_2O (Z=1.6)	0.0174	--	22.3	--
Li (Z=1)	0.0067	0.021	52.8	18.0
Li (Z=2)	0.0052	0.0052	70.0	69.6
Li (Z=2.15)	0.0031	--	120.8	--
Cs (Z=1)	0.128	0.43	12.0	3.5
Cs (Z=2)	0.127	0.589	13.0	9.2

Table 4.2: Comparison between the idealized model (IM) and MACH2 results

Material	$\varepsilon_i/(c_p T)$
Teflon , $Z \approx 2.1$	> 1.69
H_2O , $Z = 1$	1.05
H_2O , $Z = 2$	1.26
H_2O , $Z \approx 1.6$	< 0.66
Li, $Z = 1$	0.17
Li , $Z = 2$	1.52
Li , $Z \approx 2.15$	> 1.42
Cs, $Z = 1$	0.09
Cs , $Z = 2$	0.51

Table 4.3: Ratios of specific ionization energy to the thermal static specific enthalpy, c_pT, at the magnetosonic point

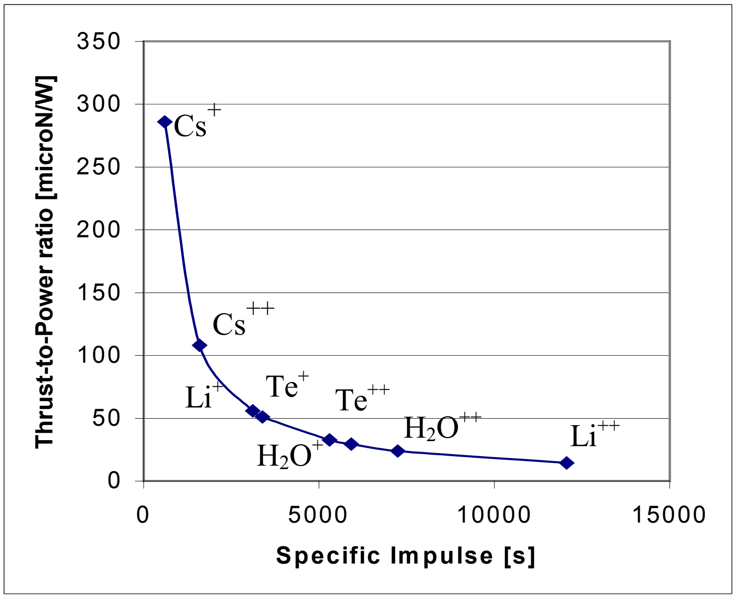

Fig. 4.5: Thrust-to-power ratio for different propellants and ionization degrees predicted by the idealized analytic model

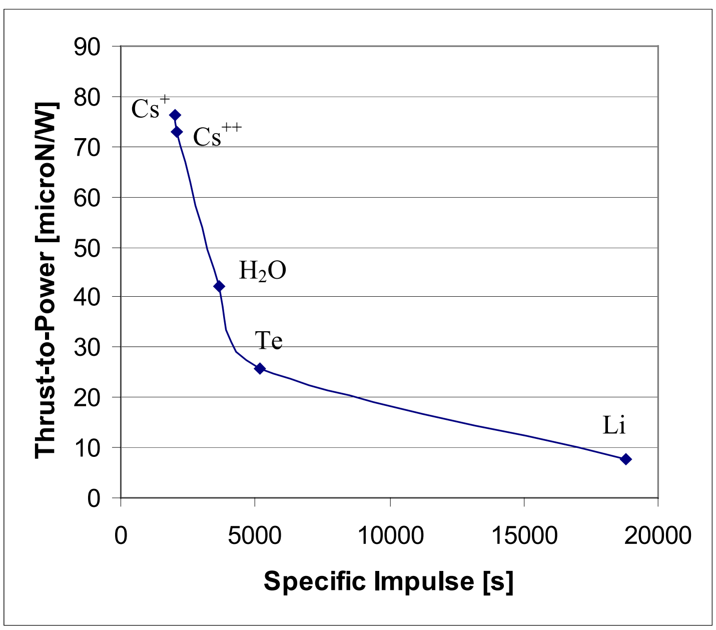

Fig. 4.6: Thrust-to-power ratio for different propellants and ionization degrees calculated by MACH2

4.4 Summary

The results of the analytic and the numerical treatment show both a significant broadening of the performance range of PPTs when considering propellants other than the standard Teflon. The simple analytic model predicts a larger range of possible thrust-to-power ratios than the MACH2 calculations can confirm. The reason for the discrepancy for some of the investigated propellants was found to be a failure of one basic assumption made in the development of the idealized analytic model. The potential of using alternative propellants, however, is confirmed by both methods despite of the discrepancy between them.

CHAPTER 5

EXPERIMENTAL APPARATUS

In the following, a general overview of the experimental setup is presented. The details of the main components like the utilized thruster and the vacuum system etc. are given in the following chapters. More information about the various diagnostic instruments and the experimental setup can be found in their respective chapters.

5.1 General Overview

For the present work a complete new vacuum and diagnostic facility was developed. Fig. 5.1 shows schematically an overview of the system.

The vacuum chamber (pyrex bell jar) is located on a table and surrounded by a cage to protect personnel and equipment. It is equipped with two separate feed-throughs, one for the high voltage connections with the thruster and one for the connections with the diagnostic instruments such as Langmuir and pressure probe. The thruster is mounted on a table inside the vacuum chamber. For diagnostic purposes this table can be moved ±7 cm in the vertical direction. Diagnostic instruments like the oscilloscope and the Langmuir probe electronics are situated in a Faraday cage, while the pump controls, pressure gauge controllers, and main power supplies are mounted in a separate rack. Both the Faraday cage and the rack are electrically grounded to a special Earth ground. A mechanical roughing pump, in connection with a turbomolecular pump, provides the means to reach background pressures in the low 10^{-5} Torr range.

5.2 Pulsed Plasma Thruster

Use of a solid propellant like Teflon significantly simplifies the construction of a thruster. No pressurized tank or feed lines are necessary. No means of propellant control mechanism such as flow valves etc. are needed. The propellant is mounted between the electrodes and only a spring is employed to keep the Teflon bar in a fixed location relative to the electrodes during the entire life time of the thruster. It can be expected that the electrode geometry (length, width, gap, etc.) and the circuitry elements (e.g. capacitance) for an efficient operating Teflon thruster will be significantly different than those of a thruster operating with water. However, it is evident from past research (Chapter 3) that already subtle changes in the above mentioned thruster elements have a major impact on discharge behavior and subsequently on thruster performance. The primary objective of the present work is the identification of thruster performance due to the use of liquid water instead of Teflon. Therefore, a hybrid thruster design was envisioned, a thruster able to use both water and Teflon without requiring major modifications in thruster geometry or circuit elements when changing the propellants. Only with such a hybrid design will an unambiguous identification of the impact of a change of propellants be possible.

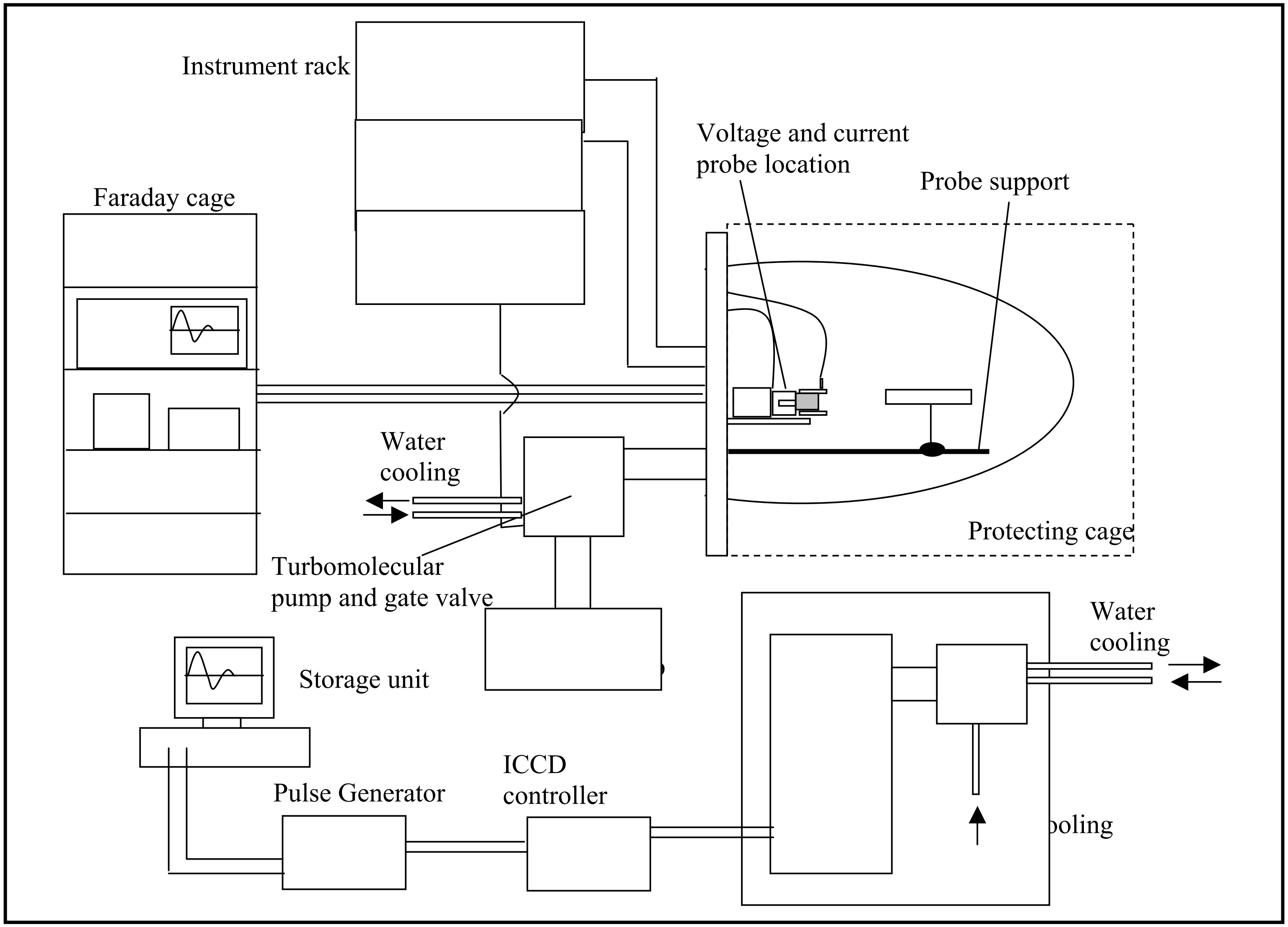

Fig. 5.1: Schematic overview of the vacuum and diagnostic facility

In the following chapter, the design is presented and discussed. The development of this hybrid thruster went through several modifications. Only the final design, which was used for the diagnostics, will be discussed in detail in Chapter 5.2.

5.2.1 Teflon Thruster

PPTs using Teflon as propellant exist in a large variety, having been developed over the last 40 years. In general one distinguishes between breech-fed, side-fed, rectangular, and coaxial PPTs. All of them have certain advantages and disadvantages. The most investigated PPT type is surely the rectangular, breech-fed PPT. Since a large data basis for this thruster type exists, it was decided to use this type as the basis for further developments.

The chosen thruster geometry is very similar to the bench mark thruster tested earlier at OSU by Kamhawi et al.[38], and also to geometries of thrusters of various other groups (e.g. LES 8/9). The effective length (measured from the Teflon ablation surface to the thruster's exit plane) and width of the electrodes is 2.54 cm, both electrodes are 0.75 cm thick and they are separated by a 2.54 cm gap. A hole in the cathode, centered at 0.8 cm from the Teflon ablation surface, allows the spark plug to be mounted such that it is flush with the electrode surface. A 0.15 cm high shoulder in the anode retains the Teflon bar, ensuring that the relative position between the Teflon bar and the spark plug is fixed.

The thruster was designed such that different capacitors can be used. Tests with a 10 μF (±10%) and a 30 μF (±15%) capacitor were conducted. However, only the results obtained with the 30 μF capacitor will be presented. The 30 μF (Maxwell Laboratories Inc.) oil-filled capacitor has a maximum voltage rating of 5kV and peak current rating of 25 kA. It is encased in a cylindrical metal case (8.5 cm in diameter and 9 cm long) to prevent leakage (the capacitor and the thruster are exposed to the vacuum). The thruster is equipped with side-walls, which are located about 0.5 cm left and right of the electrodes.

The main differences between this and other thruster designs are the transmission lines between the capacitor and the electrodes. Palumbo and Guman[12] and Kamhawi and Turchi[38] pointed out that a reduction of the circuit inductance can significantly increase the discharge peak currents, impulse bit, and efficiencies.

In an effort to reduce the circuit inductance and resistance, the commonly used parallel plate transmission lines were modified. In the new design, the transmission lines between capacitor and electrodes consists of two coaxial tubes, arranged such that the connection from the capacitor to the anode is inside the connection to the cathode (see Fig. 5.2). The two tubes are separated by a 1.3 mm thick insulation composed of mylar foil and high voltage tape to guarantee electric insulation. The Teflon bar and the spring are mounted inside the anode tube.

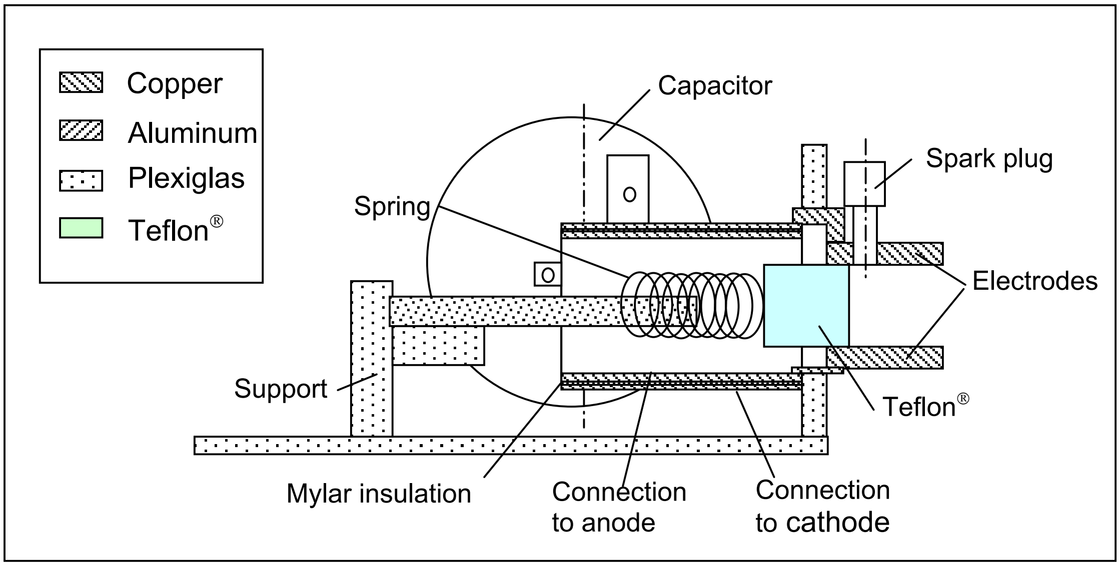

Fig. 5.2: Schematic of the Teflon PPT

5.2.2 Water Thruster

5.2.2.1 Problem Definition

The utilization of a solid propellant like Teflon has various advantages. From an engineering perspective, the two main advantages are:

1. The solid propellant requires neither propellant storage, nor a sophisticated propellant feed system (except for a simple spring).
2. The thrust producing discharge is providing itself with the amount of propellant required to sustain itself at exactly the time the discharge occurs.

Replacing the Teflon with water negates these two advantages. The notion of using water in its solid form as ice is not practical for two reasons: (i) as experimentally evaluated, the sublimation rate of water ice in vacuum amounts to several hundred $\mu g/s\text{-}cm^2$ under laboratory conditions, a value too high to be of practical use, and (ii) the elevated temperature of the various components of the thruster during operation would further increase the sublimation rate or even melt the water ice.

Resolving the difficulties involved with storage of a fluid propellant (point 1 from above) is relatively simple since numerous applications of chemical propulsion and electric propulsion systems have successfully dealt with the same problems. The main challenge in feeding water into a PPT can be summarized as follows:

To supply the water propellant in very small quantities (0.1 – 10 μg) instantaneously into the discharge area shortly before discharge initiation

While the above given quantity of water (0.1 – 10 μg) is rather an arbitrary range, only derived from the experience with Teflon thrusters, the issue of supplying the propellant instantaneously at the exact time, namely when the discharge is initiated, into the thruster has particular importance. Mismatch between the propellant feed and the discharge initiation results in propellant inefficiencies.

As mentioned in Chapter 3, Ziemer et al.[22] and Koizumi et al.[25] developed two very different systems in an effort to solve exactly this problem. Ziemer et al. utilized a mechanical valve to feed water vapor into the discharge area. Since the valves utilized have opening times in the range of several milliseconds, they employed a sophisticated discharge system which initiates a train of discharges during the time the valve is open. While they achieved high propellant utilization efficiencies with such a system, at the same time they significantly increased the complexity of the system by including moving parts (valve) and a complicated discharge scenario.

Koizumi et al. provided the water as liquid in the form of small droplets through a mechanical, ink-jet type valve. The exact timing between opening of the valve and discharge initiation was experimentally evaluated. However, high speed photography showed the presence of water droplets several milliseconds after discharge termination, suggesting poor propellant efficiency. Additionally the use of a mechanical valve increases the complexity of the thruster.

The major objective of this work was to investigate methods to supply the water propellant in a fashion which retains the simplicity of the PPT system and at the same time allows high propellant efficiencies. Consequently, rather than utilizing an active control of the mass flow rate, including valves, a passive flow control and delivery system was developed. The following chapters will present an overview and initial analysis of such a system.

5.2.2.2 Design Philosophy of the Passive Flow Control Element (PFC)

Active control of the water feed would involve valves of some kind. Antropov et al.[39] mention the possibility of fast acting ($<0.1 \times 10^{-3}$s) electromagnetic pulsed gas valves. However, these valves are still under development. Commercially available mechanical valves have, compared to the total duration of a PPT discharge, in general large opening times (several milliseconds). As mentioned above, utilizing these valves requires additional features, which in general tend to significantly increase the complexity of the PPT system.

Ruling out the utilization of mechanical valves in general allows a different perspective of the problem. Rather than focusing on the problems related to the synchronized supply of the propellant and the discharge initiation, it reduces the task only to the supply of the water in a controlled fashion and in particular to retain it in the vicinity of the discharge area for the duration between two successive discharges. Both requirements can be satisfied by what will be called in the following, a Passive Flow Control element (PFC). A PFC element consists basically of a material of certain porosity, located between the water and the low pressure (vacuum) side. The water starts to diffuse through the porous material due to the pressure gradient, dp/dl over the length l of the material. The mass flow rate, $\dot{m}_{H2O}$, is a function of the porosity of the material, the pressure gradient, dp/dl, and the size of the contact surface, A_c, between water and the porous material (see Fig. 5.3).

The diffusion process is governed by Darcy's law and the mass flow rate in the simplest 1 dimensional form can be expressed as:

$$\dot{m}_{H2O} = \rho_{H2O} \cdot k \cdot A_c \cdot \frac{dp}{dl} \tag{5.1}$$

with the density ρ (kg/m^3) of water, the coefficient of permeability k (m^3s/kg), the cross sectional contact area A_c (m^2), and the total pressure gradient over the length of the porous material dp/dl (N/m^3).

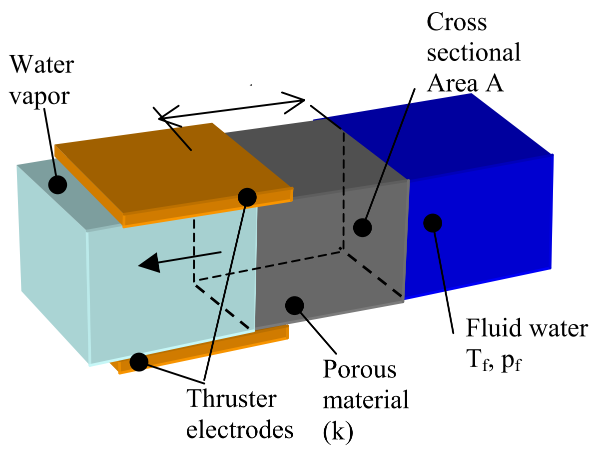

Fig. 5.3: Schematic of the water feed mechanism

A very convenient trait in dealing with this system is the number of variables one can easily adjust: the geometry and size of the contact surface, A_c, between the PFC element and the fluid water, the length of the PFC element or alternatively the pressure in the propellant plenum, both influencing the pressure gradient. The permeability coefficient, k, can be influenced by the choice of material. For example, Teflon with different densities can be utilized or, alternatively, layers of different material can be combined in order to increase or decrease the permeability.

Fig 5.4 shows schematically how a PFC element works. The water is stored in the reservoir under a certain pressure. The other side of the PFC element sees the low vacuum chamber pressure. Due to this pressure gradient, water starts to diffuse through the PFC element. In the time between two discharges, the porous material is saturated with water (saturation percentage is schematically shown in Fig. 5.4). A certain percentage of water will also escape from the porous material into the volume between the electrodes and further away. When the discharge is initiated, it will, analagous to the ablation process in the case of Teflon, utilize the water stored in a thin layer, δl, of the PFC element (Fig. 5.4, (b)). Subsequently the water will be dissociated, ionized, and accelerated. If the parameters (dp/dl etc.) of this system are chosen correctly, the time between two discharges will suffice to saturate the layer δl again with water before the next discharge is initiated.

5.2.2.3 Water Mass Flow Rate Evaluation

Candidate materials for a PFC element have to satisfy several conditions:

1. The permeability coefficient, k, must be such that water mass flow rates between 0.1 –10 μg can be achieved without excessive material lengths
2. Materials should retain their structural stability when in contact with water
3. Electrically non-conductive
4. High voltage stand off capabilities
5. Heat resistant

Two candidates satisfying all the above listed criteria are Teflon and, in general, ceramic materials. In the form of very thin layers (μm range), both materials are used as molecular filters in medical applications. Investigations of the water mass flow rate through Teflon, published by DuPont (DuPont web page), have shown that the relation mass flow rate to film thickness is non-linear, making a simple scaling process difficult. Furthermore, although the porosity is in general a known value for a specific type of Teflon or ceramic, it can vary widely depending on the production method (personal conversation with representatives of DuPont (Teflon) and Cotronics Corp. (Ceramics)).

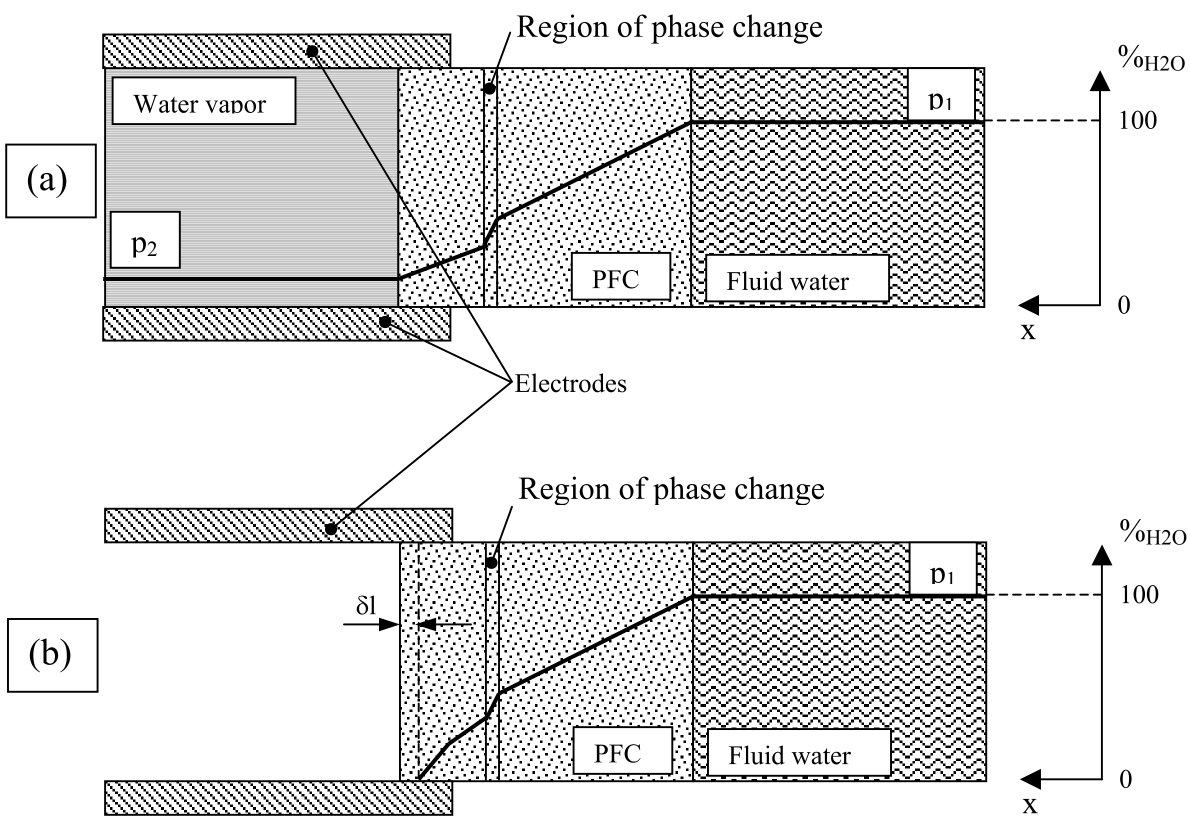

Fig. 5.4: Idealized working principle of the Passive Flow Control element shortly before (a) and after (b) initiation of a discharge

In order to investigate experimentally the mass flow rates of various materials, an experimental set up was designed. The objective of this experiment was not to carry out a detailed investigation of the mass flow processes, but rather to obtain bulk values in order to be able to select potential candidates for designing a Passive Flow Control element.

The experimental set up is shown in Fig. 5.5. It is designed such that all the vital parameters mentioned above (A_c, l, and k) can easily be changed. Figure 5.5 (b) (Photo) shows how the mass flow experiment is assembled in a feed-through of the vacuum chamber facing the vacuum side.

In order to measure the water mass flow rate through the test material, the vacuum chamber was pumped down to about 2-5 mTorr. Subsequently the vacuum chamber was separated from the pumps by closing the main gate valve. The water (pyrex re-distilled water with a low percentage of impurities (total organic carbon: 1.8 mg/L, total silica: 1.1mg/L, chlorides: 1 mg/L)) was stored under atmospheric pressure in a small plenum. Opening the electromagnetic valve (see Fig. 5.5), the water was allowed to diffuse through the test material. The mass flow rate through the porous media was then evaluated by measuring the pressure rise in the vacuum chamber over time, dp/dt, and utilizing eq. 5.2

$$\dot{m}_{H2O} = \frac{dp}{dt} \cdot \frac{V_{chamber}}{R_{H2O} \cdot T} \tag{5.2}$$

with the vacuum chamber volume $V_{chamber}$ [m^3] , the temperature T (300°K) and the specific gas constant for water (461J/kg°K).

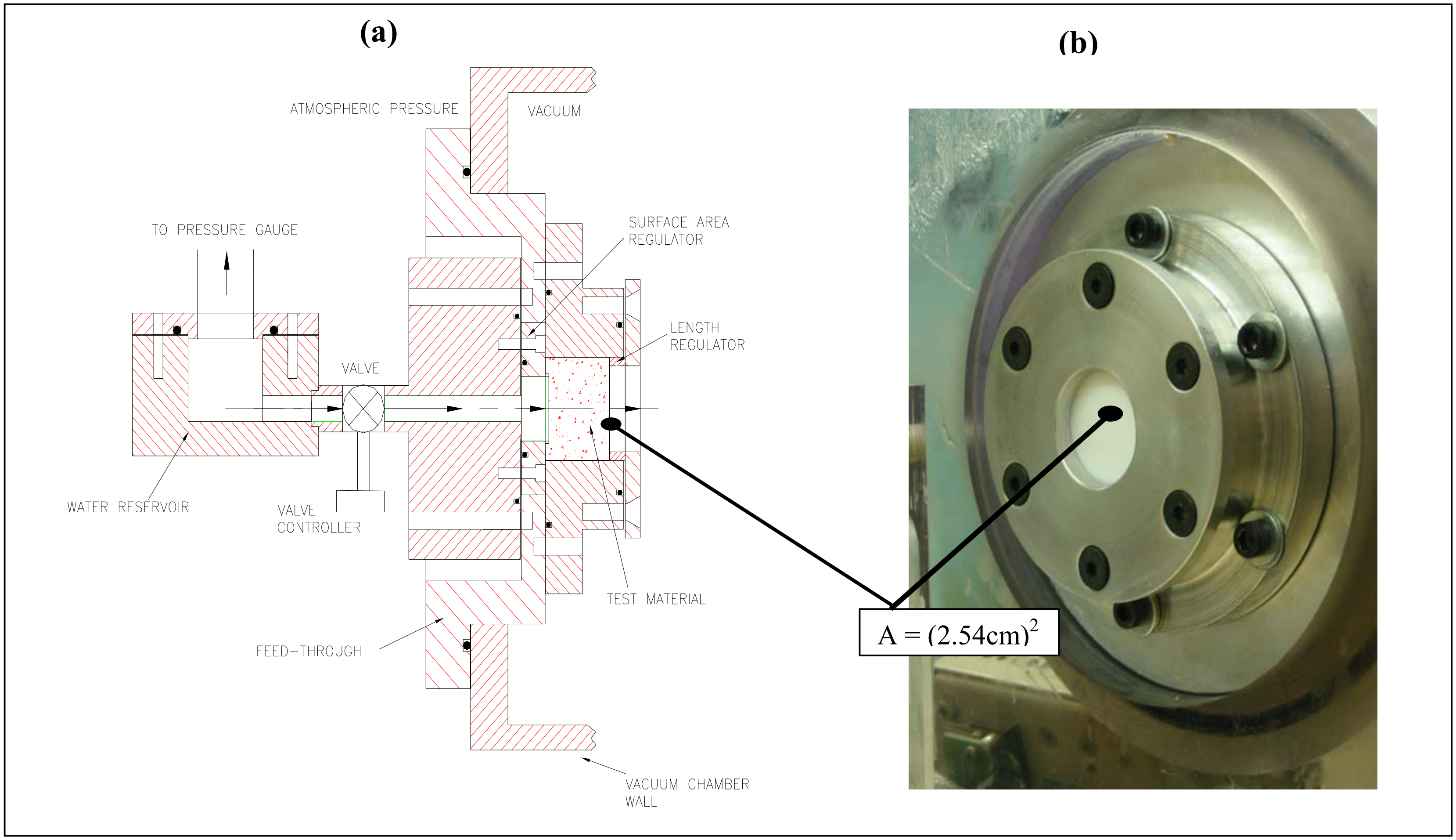

Fig.5.5: Schematic presentation and front view of the mass flow experiment

Fig. 5.6 depicts some representative results of the above described evaluation of the pressure rise after opening the electromagnetic valve. Table 5.1 summarizes the evaluated test materials and their respective mass flow rates.

As noted in Table 5.1, the porosity of some of the tested materials was too high to retain the water sufficiently. In cases of some of the materials, water droplets started to develop on the surface of the porous material as soon as the pumps started to pump down the vacuum chamber, eventually developing to a steady flow. For these cases no mass flow rate was evaluated. In the case of the 5 micron Teflon with a porosity of 25%, water droplets started to develop and freeze on the Teflon surface.

From the evaluated materials basically only two fulfilled the requirement of mass flows in the vicinity of 10 μg/s: standard Teflon and the Rescor-902 ceramic. The variation of the length of the Teflon (see Table 5.1) also showed that the mass flow rate can be controlled in a fashion predicted by the one dimensional form of Darcy's law (the moderate deviation is assumed to be due to the 1-D approximation)

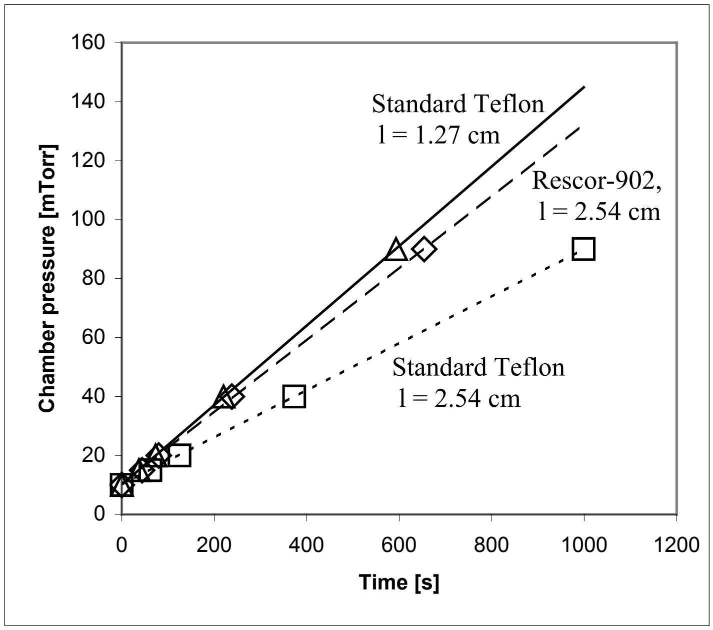

Fig. 5.6: Pressure history of the vacuum chamber due to the water mass flow rates into the vacuum chamber

Test material	Porosity	Length l [cm]	Mass flow rate [μg/s]	Comments
Standard Teflon(1)	N/A	2.54	8.3	
Standard Teflon(1)	N/A	1.27	14.0	
Teflon(2) (5 micron pores)	25 %	2.54	>1000	Initially small water droplets were visible on the surface of the material. After about 30 sec they froze on the Teflon surface.
Teflon(2) (50 micron pores)	40%	2.54	N/A	Water started to spill through the test material as soon as pump down was initiated.
Teflon(2) (100 micron pores)	40%	2.54	N/A	Water started to spill through the test material as soon as pump down was initiated
Rescor-902(3) (Alumina Silicate)	2.9%	2.54	12.7	
Rescor-960(3) (Alumina)	10%	2.54	640	
Rescor-311(3) (Alumina Silicate)	63%	2.54	>1000	Initially small water droplets were visible on the surface of the material. After a short time they froze on the ceramic surface

Table 5.1: Investigated materials and their respective water mass flow rates (A_c =0.8 cm^2)

Sources: (1): American Plastics, Columbus, Ohio, (2): FluoroLogic, LLC, Los Alamitos, California, (3): Cotronics Corp., Brooklyn, New York

5.2.2.4 Water Thruster Configuration

Guided by the above discussed mass flow experiments and by the general requirement that the thruster configuration for water should be as close to the Teflon thruster configuration as possible (see introduction to this chapter), several different versions of a water thruster configuration were designed, built, and tested. They were named in sequence starting with WPPT-1 to WPPT-4. WPPT-1 to WPPT-3 will briefly be discussed in this chapter. Only the final design, WPPT-4, will be presented in the detail.

The initial design, named WPPT-1, followed closely the schematics in Figs. 5.3 and 5.4. The Teflon bar and the spring were replaced by the PFC element, which was attached to a small water reservoir. The sides of the PFC element were covered with epoxy to force the water to exit the PFC element only on the side facing the discharge area between the electrodes. Tests included Teflon, Rescor-902, Rescor-960, and a combination of Teflon and Rescor-960[40].

Starting at small mass flow rates, it was found that the discharge currents were much lower than in the case of Teflon. Additionally, in the case of 10 J and 20 J discharge energy, the thruster frequently did not discharge at all. Arguing that this might be due to an insufficient amount of water propellant participating in the discharge, the mass flow rates were increased from about 10 μg/s up to 600 μg/s by changing the geometry of the PFC element (length of the PFC element and size of the contact surface A_c). Indeed, increasing the flow rate lead to slightly higher discharge current.

However, since increasing the mass flow rate decreases the efficiency of the thruster at the same time, it was felt that further possibilities have to be explored.

It was evident that in order to obtain a reliable discharge behavior and possibly higher discharge currents, the method to supply the water into the discharge area had to be modified. The design described above allows the water to enter the discharge area over a total area of 6.45 cm^2 (2.54 x 2.54 cm). It was reasoned that due to this relative large area, the available water in the volume where the discharge is initiated is too small, especially for low mass flow rates. The objective of the new design was therefore to change the method to supply the water into the discharge area such that at the moment of discharge initiation the water density in the discharge area is higher.

Figs. 5.7 and 5.8 show schematically the result of the design overhaul, named WPPT-4. The major part of the thruster is identical to the Teflon thruster (see Fig. 5.2). The water is now fed through the PFC element (Rescor-902) into a volume in front of the spark plug. Both the spark plug and the PFC element are mounted inside the cathode (see Fig. 5.7). The volume in front of the spark plug is connected through a thin channel (7 mm x 0.8 mm) with the volume defined by the side-walls and the electrodes. Like before, it is assumed that a certain percentage of the water will be stored in the structure of the ceramic (while the rest will either linger in the small volume in front of the spark plug or escape into the vacuum chamber). When the spark plug triggers, it will free some of the water in the ceramic and force it into the discharge channel. The water, together with the spark plug material, will then initiate the main discharge.

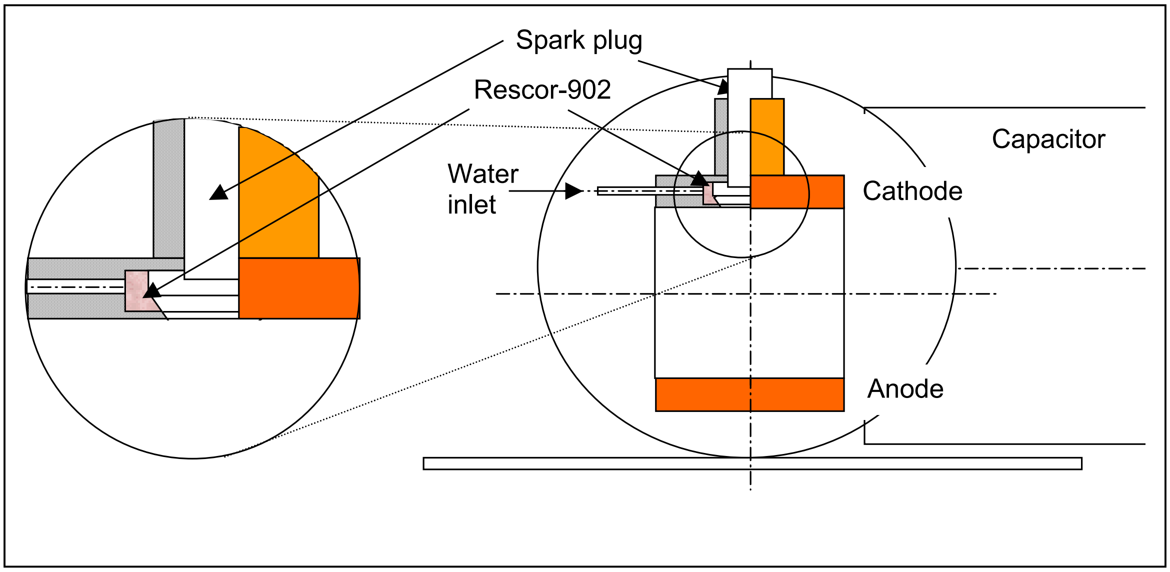

Fig. 5.7: Front view of WPPT-4 with details of the propellant feed mechanism

The configuration WPPT-4 has the advantage that the surface area of the ceramic through which the water enters is about a factor of 7 smaller then in the former designs, thereby focusing the water into a smaller volume. Furthermore, the method of injecting the water together with the spark plug discharge avoids any concerns about synchronization of discharge initiation and propellant injection. Fig. 5.8 shows a side view and top view of the water PPT.

Though initial testing of this configuration showed discharge currents in the same low range as before (10 –12 kA at 20 J), it also showed a reliable discharge behavior even for water flow rates as low as 1.1 µg/s[41].

It was therefore decided to utilize WPPT-4 as the final configuration for further investigations and plasma diagnostics.

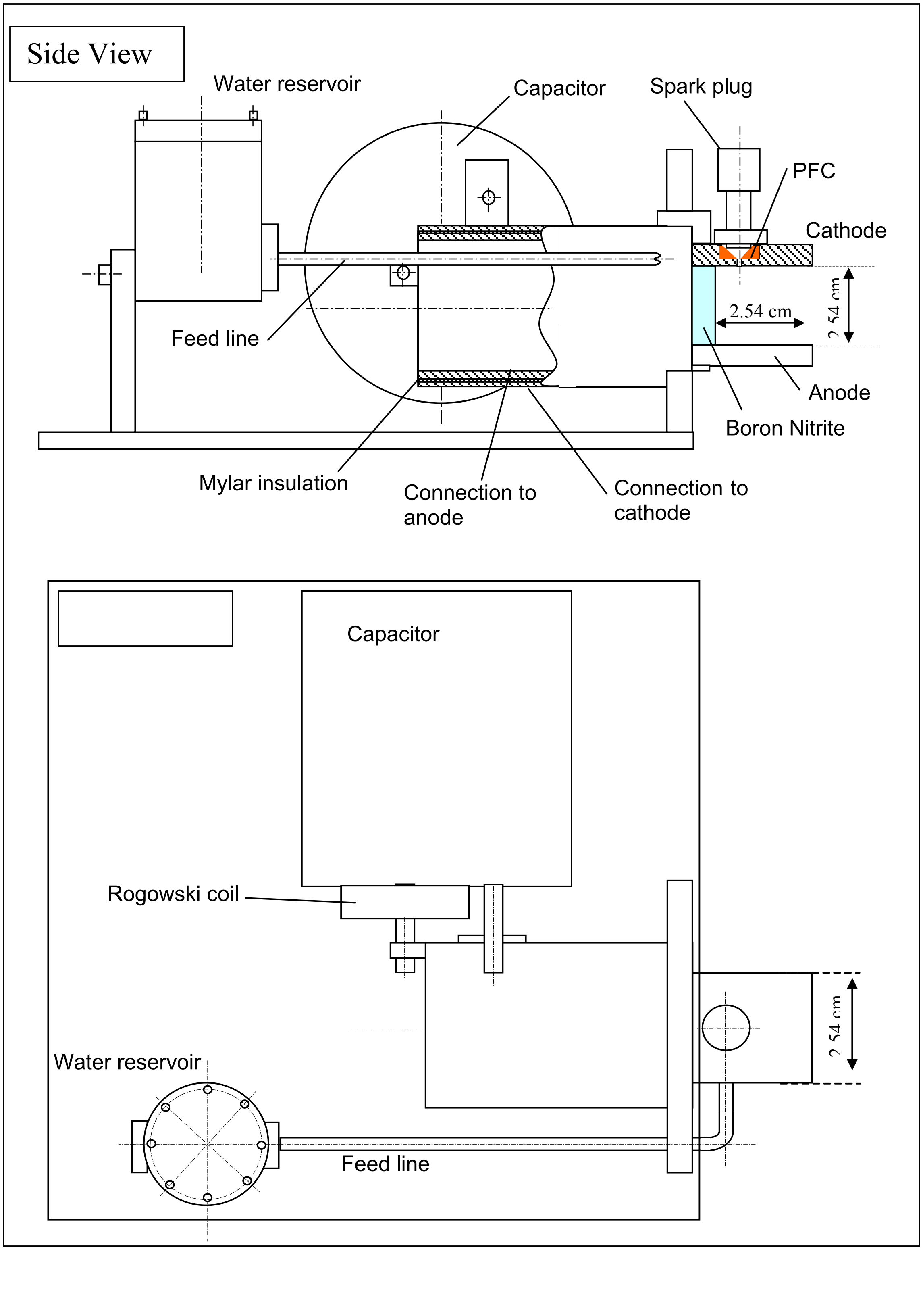

Fig. 5.8: WPPT-4 configuration with water reservoir and feed line

5.3 Electrical Discharge Circuits

The electric circuitry of a PPT consists of three separate units: (i) the charging circuit, (ii) the trigger circuit, and (iii) the discharge circuit. The discharge circuit is mainly governed by the generated plasma and will be discussed in detail in Chapter 6.1. The charging circuit supplies the thruster with the necessary energy. It consists of a high voltage power supply (Glassman, series EW, 500 W) and a capacitor (Maxwell Laboratories Inc., 30 μF). The discharge energy is controlled through the charging voltage. To protect the power supply from the high frequency oscillation occurring during operating of a PPT, a high frequency filter is added into the circuit. The trigger circuit initiates the main discharge with the help of a spark plug (Unison Industries Inc., Jacksonville, FL). The spark plug discharge is controlled by an ignition exciter unit (Unison Industries Inc., Jacksonville, FL) and powered by a Lambda power supply (model LQ-410, 1-10V, 2A). The discharge frequency of the spark plug is controlled through the voltage applied to the ignition exciter unit.

The capacitor voltage and the discharge currents are monitored with the help of a standard Tektronix voltage probe (TEK5100, attenuation factor x100) and a laboratory made Rogowski coil, respectively. The Rogowski coil and its calibration are discussed in Chapter 6.

5.4 Vacuum Facility

Operation and performance of PPTs is known to be sensitive to the background pressure in the vacuum chamber. The vacuum system used in earlier experiments at The Ohio State University was only capable of reaching background pressures around 2-5 mTorr. Since the background pressure can have deleterious effects on the results of the diagnostic, and most of the research done by other groups is performed at background pressures at least two orders of magnitude lower, it would make a comparison of results difficult. Furthermore, due to the low pumping speed of the utilized mechanical pumps and the relative large volume of the vacuum tank, it required a rather long time to reach the minimum pressure. A new vacuum system was therefore designed and built.

The new vacuum system and its main components are illustrated in Fig. 5.1 The compact design of the system and the utilization of a TURBOVAC turbomoleculare pump (NT 220, Leybold-Heraeus) in conjunction with a conventional roughing pump allow to reach background pressures in the high 10^{-6} Torr range. The convenient small vacuum chamber (Pyrex bell jar, V_c~$0.1m^3$) and the compact vacuum lines made it possible to reach the necessary background pressure in a relatively short time.

The vacuum chamber is located in a plexiglass cage to protect personnel and equipment in case of an imploding chamber. Ventilation ducts at the rear end of the cage are provided to reduce the load on the cage in such a case. The horizontal positioning of the bell jar (conventionally used in an upright position) made special care necessary to avoid misalignment with the base plate of the vacuum chamber, potentially resulting in a torque on it, which could lead to its destruction. To prevent this, a supporting structure was designed, allowing transverse movement of the bell jar perpendicular to the base plate and additional rotation around two axes. A precise alignment has been achieved with this configuration.

The base plate, which closes the vacuum chamber at its open end, provides the connection to the vacuum line and feedthroughs for two high voltage and up to twelve low voltage connections. The base plate is rigidly attached to the cage structure to prevent bending and successive leakage in the process of pumping the system down.

The vacuum chamber can be separated from the vacuum feed lines with an electropneumatic main gate valve (HANNIFIN, Model GG-200-25). Pressure in the vacuum chamber is measured with a thermocouple (TC Vacuum Gauge, type 0531) in conjunction with a gauge controller (MKS, type 286) for pressures above 1 mTorr and an ion gauge (Veeco, type RG-75-K) in conjunction with a separate controller (Granville-Phillips, type 280) for pressures in the $10^{-6} - 10^{-4}$ Torr range. An additional thermocouple of the same type as the one above was located downstream of the main gate valve. Two separate bleeding valves, upstream and downstream of the main gate valve, allow keeping the chamber under vacuum while the downstream side is under atmospheric pressure (necessary to avoid roughing pump oil in the molecular pump).

5.5 Probe Support

A probe support for the measurements with the Langmuir, the magnetic field, and the pressure probe was built (see Fig. 5.9). The probe support allows the variation of the measurement location in all three directions (x, y, z). To change the measurement location the chamber had to be opened and the position of the probe had to be changed by hand. The limits of the location variations in all three directions are shown in Fig. 5.9.

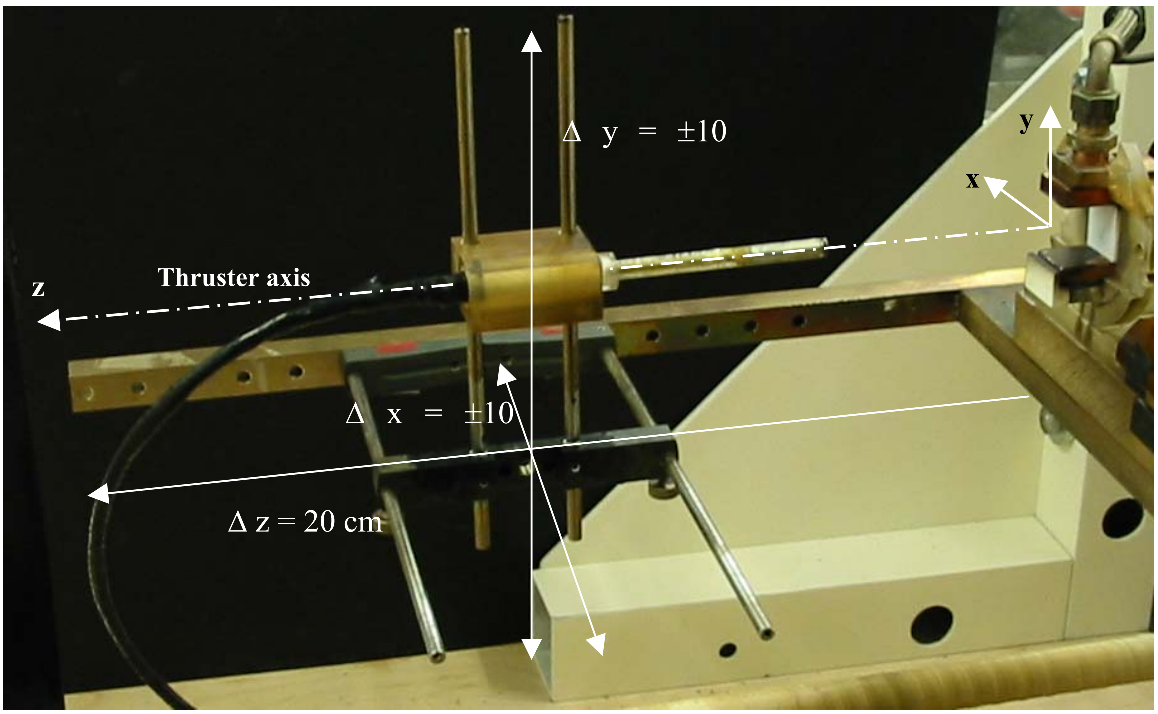

Fig. 5.9: Probe support and the range of possible locations

CHAPTER 6

CIRCUIT DIAGNOSTICS

Although the measurements of the discharge currents and voltages constitute one of the most straightforward methods of thruster diagnostics, they provide important insight into the governing processes and even allows first estimations of thruster performance. The following chapter outlines a simple method to model the thruster in terms of its electric circuit elements. Results for the current and voltage measurements are presented. Based on these results, circuit parameters of the thruster were determined, allowing the identification of important differences between operation of the thruster with Teflon vs. water.

6.1 Introduction and Theory

An idealized model pictures the discharge in a PPT as a discrete sheet of current, moving towards the thruster exit. Even though this is clearly a very simplified model of the arc, as shown by Eckbreth[42] and more recently by Berkery and Choueiri[43], it allows the modeling of the electric system, including the thruster, as a simple inductance-resistance-capacitance (LRC) circuit as pointed out by Jahn[1]. Fig. 6.1 illustrates the different elements of such a circuit model. One distinguishes in general between external and internal circuit elements. External circuit parameters consist of the inductance L_L and resistance R_L of the current leads and the capacitance C of the capacitor and its own parasitic inductance L_C and resistance R_C. Internal circuit elements model the resistance R_P and inductance L_P of the discharge arc in the thruster.

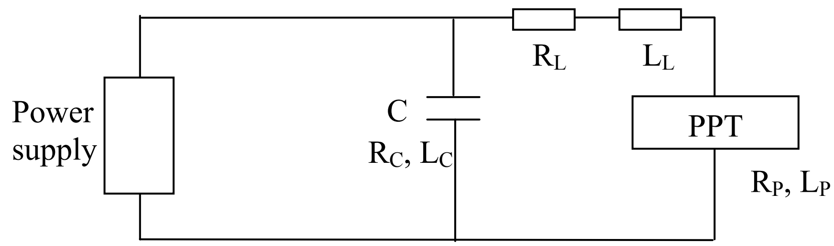

Fig. 6.1: Elements of the circuit model

At initiation of the discharge, the breakdown of the gas completes the circuit, having a total initial inductance of $L_t(t=0) = L_L+L_C$ and total initial resistance of $R_t(t=0) = R_L+R_C+R_P(t=0)$. With time, the discharge intensifies and starts to move towards the exit of the thruster, thus changing the plasma resistance and inductance. A simple application of Maxwell's third equation ($\nabla x\vec{E} = -d\vec{B}/dt$) around the changing circuit allows expressing the voltage V(t) across the electrodes in the following way:

$$V(t) = I(t) \cdot R_t(t) + \frac{d}{dt}\left(L_t(t) \cdot I(t)\right) \tag{6.1}$$

Furthermore, with

$$I(t) = -\frac{dQ(t)}{dt} \quad and \quad V(t) = \frac{Q(t)}{C} \tag{6.2}$$

and assuming L_t and R_t are constant in time, Eq. 6.1 can be written as a differential equation for the charge Q:

$$L_t \cdot \frac{d^2Q}{dt^2} + R_t \cdot \frac{dQ}{dt} + \frac{Q}{C} = 0 \tag{6.3}$$

Equation 6.3 has two solutions depending on the initial conditions. Assuming Q = Q(t=0), I (t=0) = dQ(t=0)/dt, the charge or current waveform is either under-damped or over-damped, depending on the following ratios:

$$\text{Under-damped:} \frac{C \cdot R_t^{\,2}(t=0)}{4 \cdot L_t(t=0)} < 1 \tag{6.4}$$

$$\text{Over-damped:} \frac{C \cdot R_t^{\,2}(t=0)}{4 \cdot L_t(t=0)} > 1 \tag{6.5}$$

In the case where the above ratio is unity, one refers to the waveform as a critically damped waveform.

The choice of the circuit elements has significant impact not only on the discharge behavior but also ultimately on the thruster performance. Solbes and Vondra[11] conducted a thorough investigation of the influence of circuit parameters on thruster parameters like thrust and specific fuel consumption, etc. A summary of their results is given in Table 6.1. Arrows pointing up or down indicating an increase or decrease of the respective parameter. All the tests were performed for the same energy.

	Specific Impulse I_{sp}	Specific fuel consumption m/E	Thrust F
Inductance ↑	↑	↓	↓
Resistance ↑	N/A	↓	↓
Capacitance ↑	↑	↓	↓

Table 6.1: Influence of circuit parameters on thruster performance

6.2 Experimental Setup for Current and Voltage Measurements

The experimental setup for the current and voltage measurements consists of a Rogowski coil connected to a passive integrator (RC =100μs) and the oscilloscope (Tektronix, TDS 420A) to measure the discharge current. The voltage across the capacitor was measured with a standard voltage probe (Tektronix P5100, x100, 2.5kV peak). To assure consistency in the voltage measurements, the probe was in frequent intervals calibrated and compensated over the duration of this work.

Current and voltage measurements were conducted during the entire duration of this work since they allow a convenient method to monitor the performance of the thruster. The current signal was additionally employed for trigger purposes, therefore providing a uniform time reference for comparison of different measurements. The experimental setup is schematically shown in Fig. 6.2.

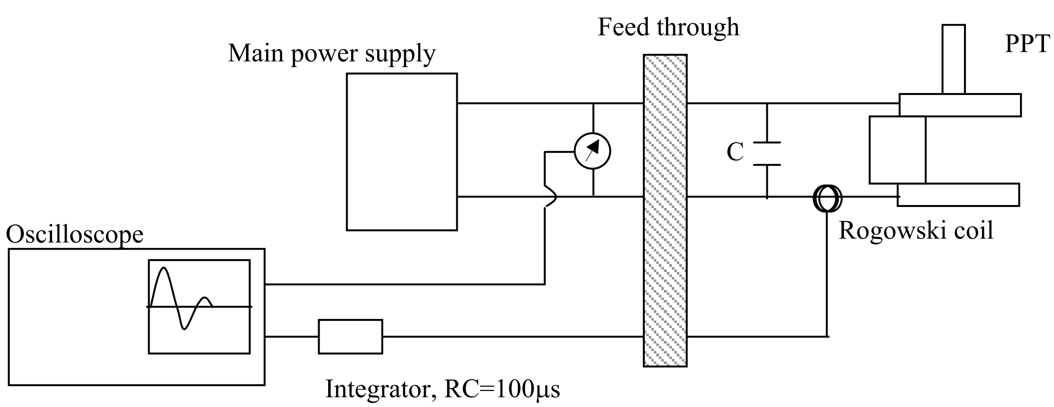

Fig. 6.2: Schematic presentation of the experimental setup for the current and voltage measurements

In order to keep the current leads between capacitor and anode as short as possible and the circuit inductance low, a new Rogowski coil was constructed for the current measurements. The geometry of the coil is such that it fits precisely around the hot stud of the capacitor. The Rogowski coil consists of a 12-turn solenoid wrapped around an insulated copper ring. The endings of the solenoid are twisted and connected to a coaxial cable leading to the feed through of the vacuum chamber.

The calibration of the Rogowski coil was conducted utilizing the Teflon PPT. Both the Rogowski coil and a Pearson current monitor (Palo Alto, CA, model 5046, accuracy ±1%) were positioned around the lead connecting the hot stud of the capacitor with the anode. In order to fit both of them, the lead had to be modified. This resulted in an increase of the circuit inductance but kept the thruster system otherwise unchanged. Fig. 6.3 shows the calibration setup. The calibration was performed in the vacuum chamber at a background pressure of 5×10^{-5} Torr. The 10 μF capacitor was charged up to about 2 kV, resulting in a discharge energy of 20 J. The signal of the Rogowski coil was integrated with a passive integrator having a time constant of 100 μs. The calibration constant was determined by simultaneously recording the output of the Pearson current monitor and the integrated signal of the Rogowski coil and evaluating the ratio of these outputs. By averaging 10 data sets, a calibration constant for the Rogowski coil of 9988 A/V was evaluated. Uncertainty of this calibration is 4%, which is mainly due to the averaging process and the accuracy of the Pearson current monitor.

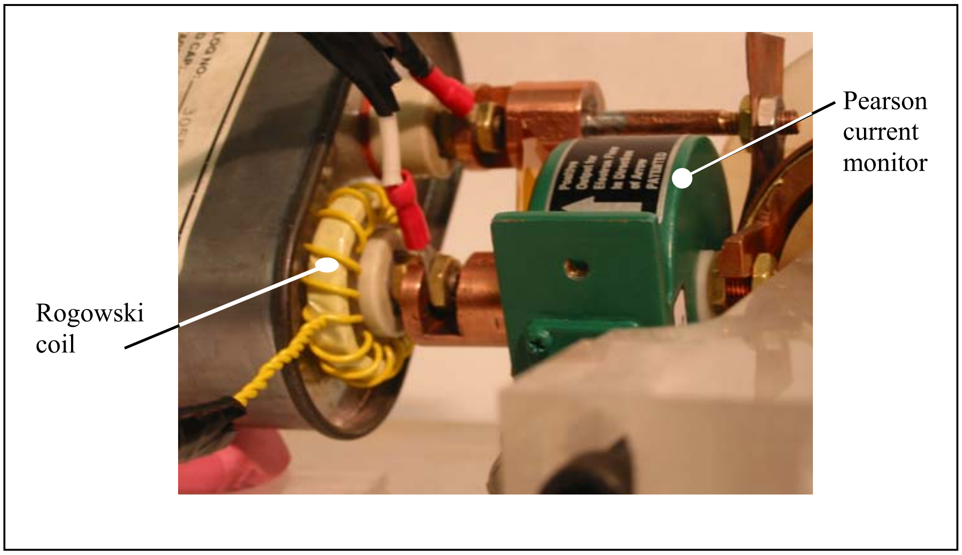

Fig. 6.3: Calibration of the Rogowski coil with the Pearson current monitor

6.3 Data Acquisition and Procedure

Prior to any measurements the thruster was allowed to operate for several minutes. This assures that transition effects, as described by Spanjers et al.[16], do not impact the measurements.

PPTs are known for their shot-to-shot variations with regard to the discharge current and voltage. These variations are assumed to be due to various reasons, including slight differences in initial particle density the discharge encounters and the rather erratic discharge initiation of the spark plug. Since it is reasonable to assume that these shot-to-shot variations will have an impact on the results of the plasma diagnostic, they needed to be quantified.

Figs. 6.4 and 6.5 depict the initial part of the discharge current for Teflon and water respectively. Both data sets were obtained for 30 J discharge energy. Each figure shows the discharge current history of five successive measurements (dotted lines) and their averaged current history (solid line). The reproducibility in terms of the discharge current in both cases is relative good. However, the water thruster shows, especially in the initial phase, a more erratic behavior. The current rise in the water case has a shot-to-shot variation of up to ±0.5 μs compared to ±0.2 μs for the Teflon thruster. The magnitude of the peak currents in the water case have a variation of about ±2.5 % (±0.35 kA) compared to only ±1% (0.3 kA) in the case of the Teflon thruster. The same trend is observed for the 20 J discharge case. Only at a discharge energy of 10 J, the water thruster shows a significant higher shot-to-shot variation in terms of the magnitude of the peak (±10%) while those for Teflon are roughly the same as in the higher energy cases.

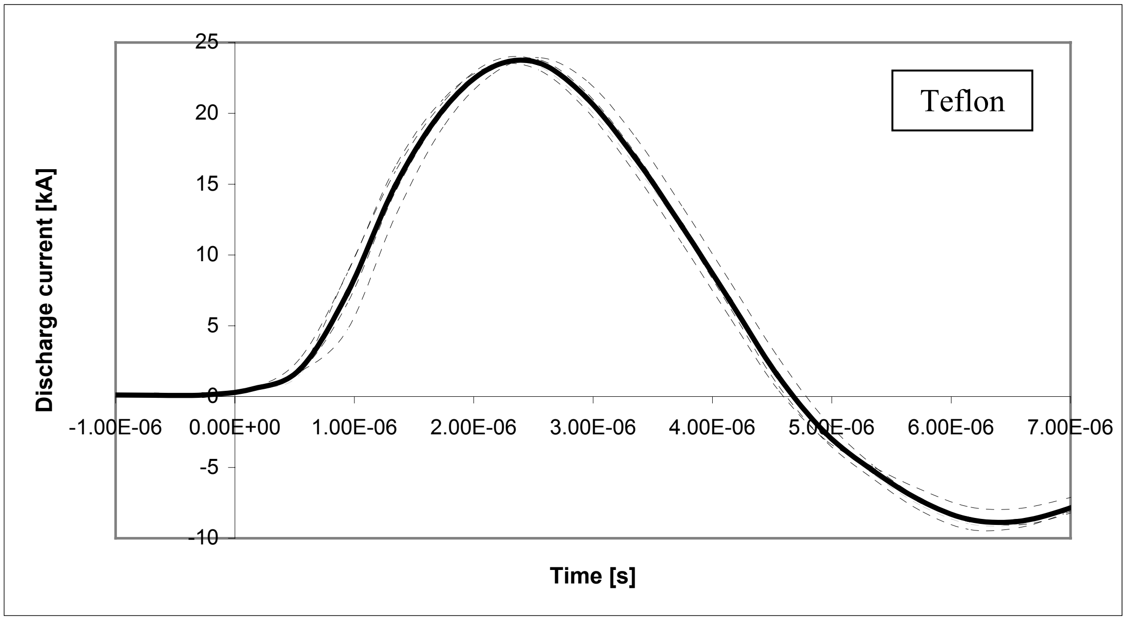

Fig. 6.4: Discharge current shot-to-shot variations (dotted) for the Teflon thruster at a discharge energy of 30 J and their average (solid)

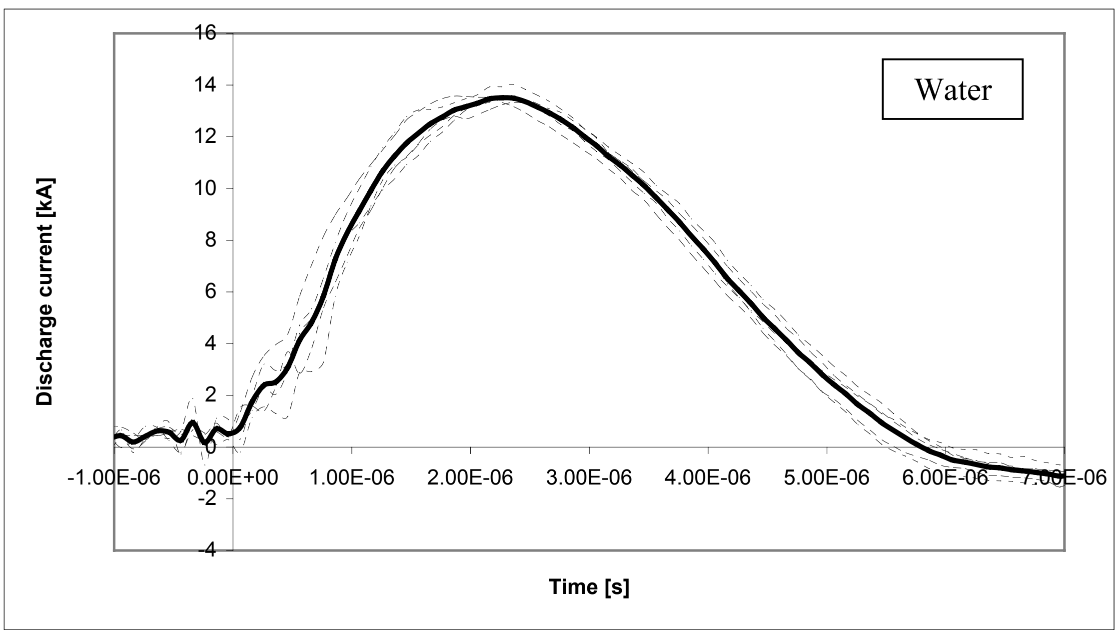

Fig. 6.5: Discharge current shot-to-shot variations (dotted) for the water thruster at a discharge energy of 30 J and their average (solid)

6.4 Experimental Results and Reduction of Data

6.4.1 Discharge Current and Voltage Measurements

The discharge current in a given PPT system is a function of the capacitance and the internal and external plasma resistance and inductance (R_P, R_C, R_L, L_P, L_C, L_L). By employing the hybrid thruster design as described in Chapter 5.2, the capacitance and external circuit parameters for the Teflon thruster and the WPPT-4 are identical. Any difference between the current and voltage history of the Teflon and the water thruster is subsequently due to the different propellants.

Figs. 6.6 and 6.7 show the current and voltage history (30 J discharge energy) for the Teflon thruster and the WPPT-4, respectively. As expected, changing the propellant type has a significant impact on the discharge behavior of the thruster. While the discharge current for the Teflon thruster shows the typical under-damped form, the water discharge current resembles a critically damped waveform. The peak currents for the water case are lower in all the investigated energies, as shown in Figs. 6.8 and 6.9, suggesting higher plasma resistance and inductance. The possibility of a starvation of the discharge due to insufficient amounts of propellants was experimentally investigated by increasing the water mass flow rate in several steps from about 10 μg/s up to 600 μg/s. Since this did not result in an increase of the discharge current, it is assumed that effects other than the magnitude of the mass flow rate are responsible for the low discharge currents.

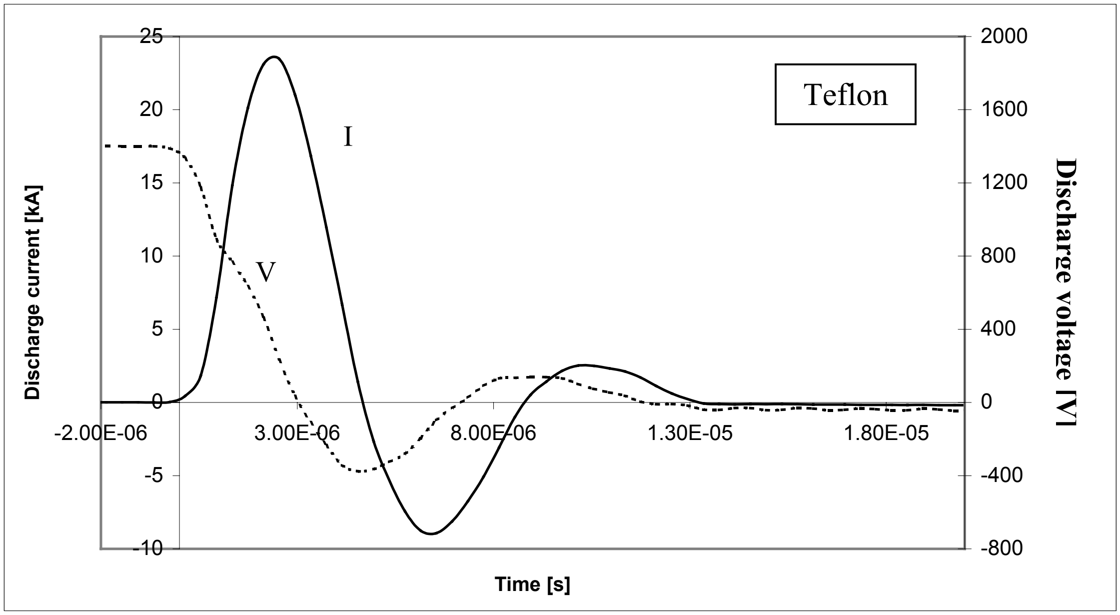

Fig. 6.6: Current and voltage history for Teflon 30 J discharge energy

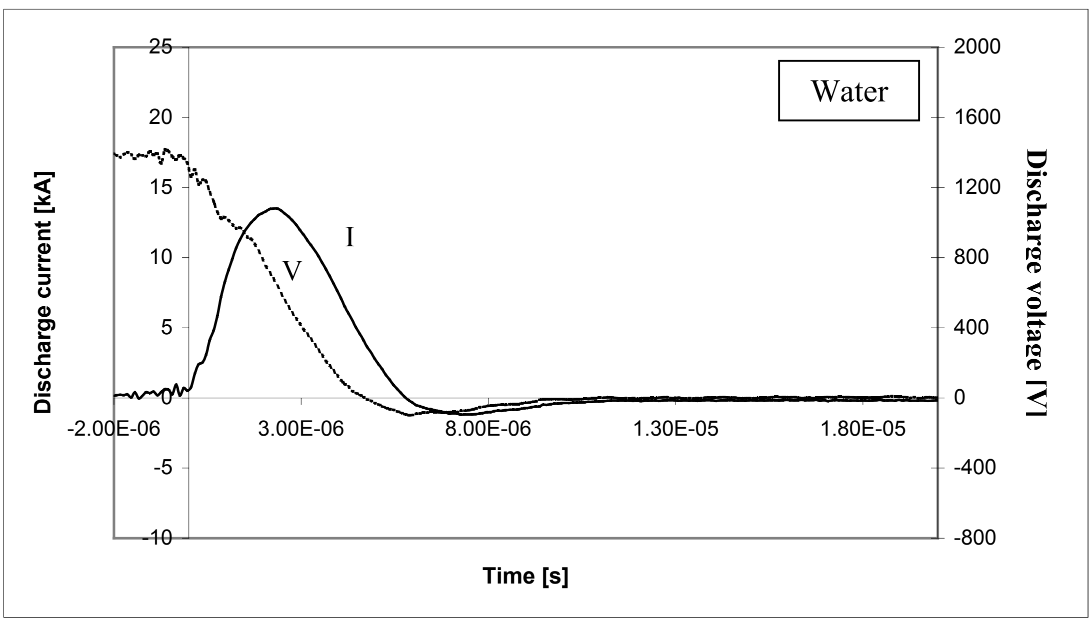

Fig. 6.7: Current and voltage history for water 30 J discharge energy

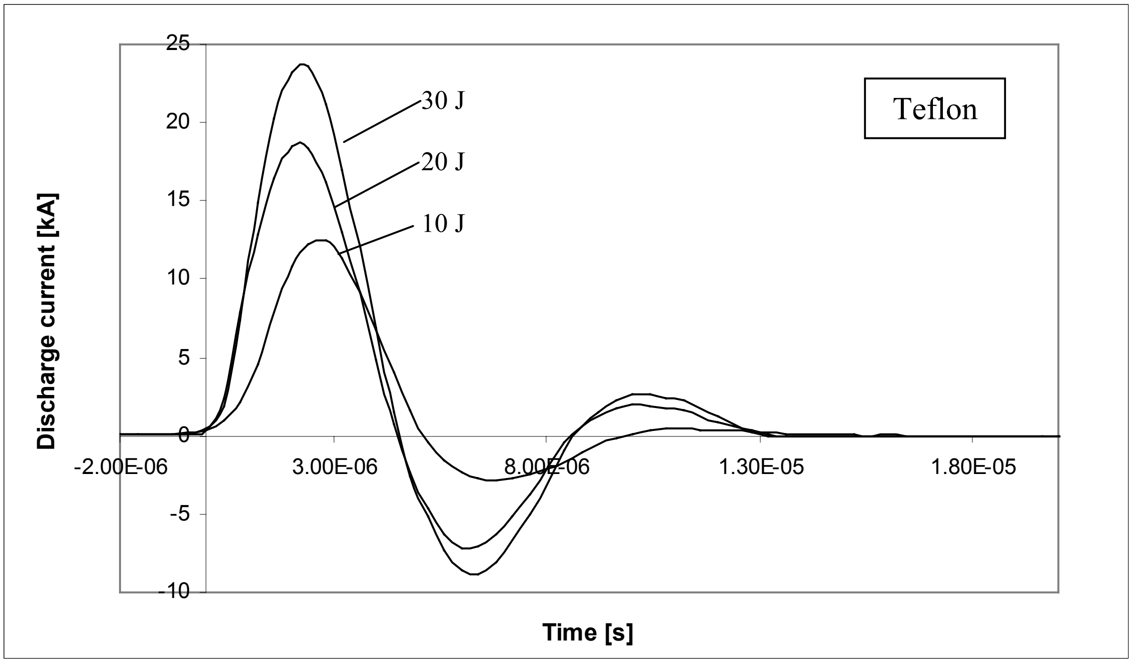

Fig. 6.8: Current history for Teflon at different discharge energies

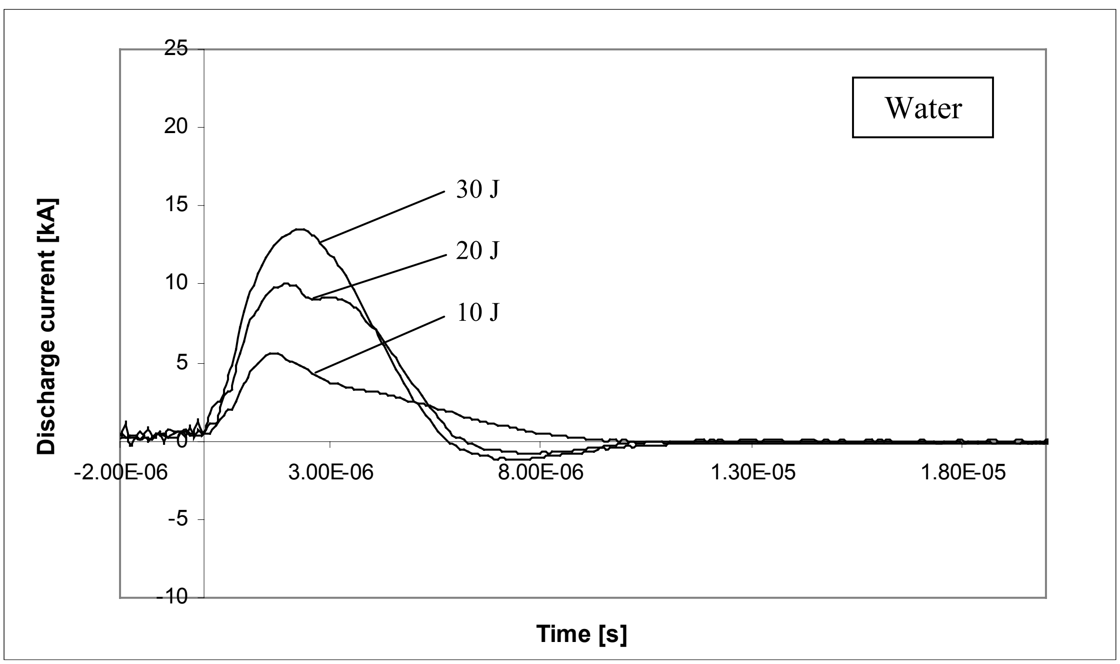

Fig. 6.9: Current history for water at different discharge energies

6.4.2 Evaluation of Circuit Elements

The knowledge of the discharge current history allows the determination of circuit parameters like the total inductance and resistance. The inductance of a LRC circuit can be calculated by recognizing that the period of the sinusoidal current waveform is given by:

$$T = 2\pi\sqrt{L \cdot C} \tag{6.6}$$

with the period T = 2Δt as indicated in fig. 6.10. Subsequently,

$$L = \frac{T^2}{4\pi^2} \cdot \frac{1}{C} \tag{6.7}$$

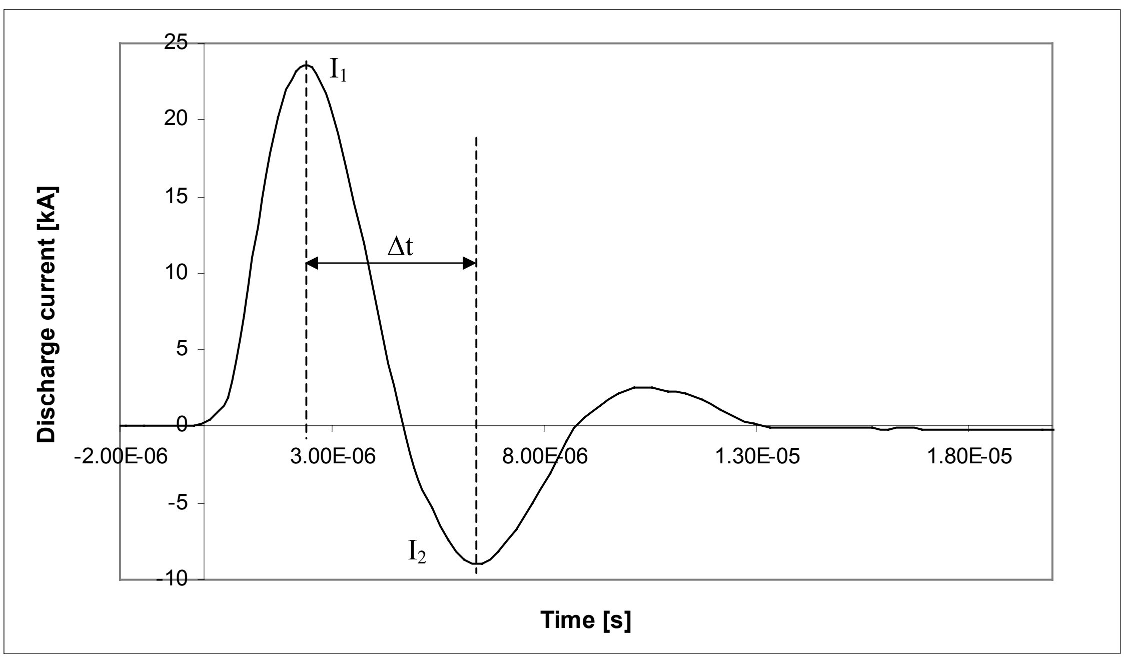

Fig. 6.10: Evaluation of T and the ratio of I_1/I_2

The ratios of two subsequent current peaks (see Fig. 6.10) are related to the circuit resistance and inductance in the following fashion

$$\frac{I_1}{I_2} = e^{\frac{R \cdot T}{2 \cdot L}} \tag{6.8}$$

Knowing the circuit inductance from Eq. 6.7, the circuit resistance R can be evaluated with

$$R = \frac{2 \cdot L}{T} \cdot \ln\left(\frac{I_1}{I_2}\right) \tag{6.9}$$

It has to be emphasized that this is only an approximation of the circuit resistance and inductance since both are not constant in time as it is assumed in the above analysis.

Utilizing Eqs. 6.8 and 6.9 and the discharge currents as shown in Figs. 6.8 and 6.9, the circuit parameters were calculated and are summarized in Table 6.2. No evaluation of the circuit parameters was performed for the 10 J water case due to its critically damped waveform shape. From Table 6.2 it is evident that the resistance and the inductance in the water case are significantly higher than it is the case for Teflon. Additionally, other than in the case for Teflon, for water one can observe an increase in inductance with decreasing discharge. The latter is attributed to the fact that the mass bit in the case of water is fixed, while in the case of Teflon the magnitude of the discharge current determines the mass bit.

Discharge energy		Period T [μs]	I_1/I_2	Inductance L [nH]	Resistance R [mΩ]
30 J	Teflon	8	2.8	52	13.6
	Water	**10**	**11.3**	**81**	**39.4**
20 J	Teflon	8	2.6	52	12.4
	Water	**11.2**	**12.2**	**102**	**45.6**
10 J	Teflon	8	4.5	52	19.4
	Water	**N/A**	**N/A**	**N/A**	**N/A**

Table 6.2: Circuit parameters for operation with Teflon and water and a capacitance of $C = 31.1\mu F$

CHAPTER 7

PROPELLANT CONSUMPTION

7.1 Introduction

Thruster performance is closely related to the propellant consumption. The pulsed nature of PPTs and the relative high shot-to-shot variations require an averaging method over at least several thousand discharges to evaluate the propellant usage per discharge, also called mass bit. It is obvious that due to the different nature of the state of the propellant (solid vs. liquid/gaseous) and the different fashion of feeding the propellants, two fundamentally different methods are required to evaluate the mass bits for the water and the Teflon thruster.

In the following chapters the procedures to evaluate the different mass bits are outlined and the results are presented. The results of the mass bit evaluation in conjunction with the Impulse bit measurements allows subsequntly the calculation of performance parameters like specific impulse, efficiencies, etc.

7.2 Teflon Thruster

To evaluate the Teflon consumption rate, a simple weight measurement (Mettler AE100) of the Teflon bar before and after a run is sufficient. The mass bits were evaluated for 10, 20, and 30 J discharge energy. For all discharge energies, the thruster was operating for >5000 discharges. Since the total mass of the Teflon bar influences its heat capacity and can result in measurable differences in ablation rates[16], the three different Teflon bars, one for each energy level, had the same dimensions (2.54 x 2.54 x 2.54 cm). Being exposed to normal room air, Teflon can absorb water vapor up to 1% of its own weight. After being exposed to a vacuum for several hours and the additional heat influx due to thruster operation, is has to be assumed that the Teflon does not contain any water. In order to avoid errors in the weight measurements due to differences in the amount of water vapor in the Teflon bar before and after the experiment, the Teflon bar was allowed to adjust to room humidity after the run for a period of at least 24 hours before weighting.

The temperature of the thruster was not monitored for these runs and in order to avoid excessive heating of the thruster, all the runs were split into two parts with a 1 hour break in between (2 hours in case of the 30 J test). Table 7.1 and Fig. 7.1 summarizes the ablation results.

Discharge energy [J]	# of discharges	Ablation/discharge [μg]	Ablation/unit of energy [μg/J]
10	5400	11.9	1.19
20	5400	27.5	1.375
30	5500	35.3	1.18

Table 7.1: Teflon ablation rates for various discharge energies

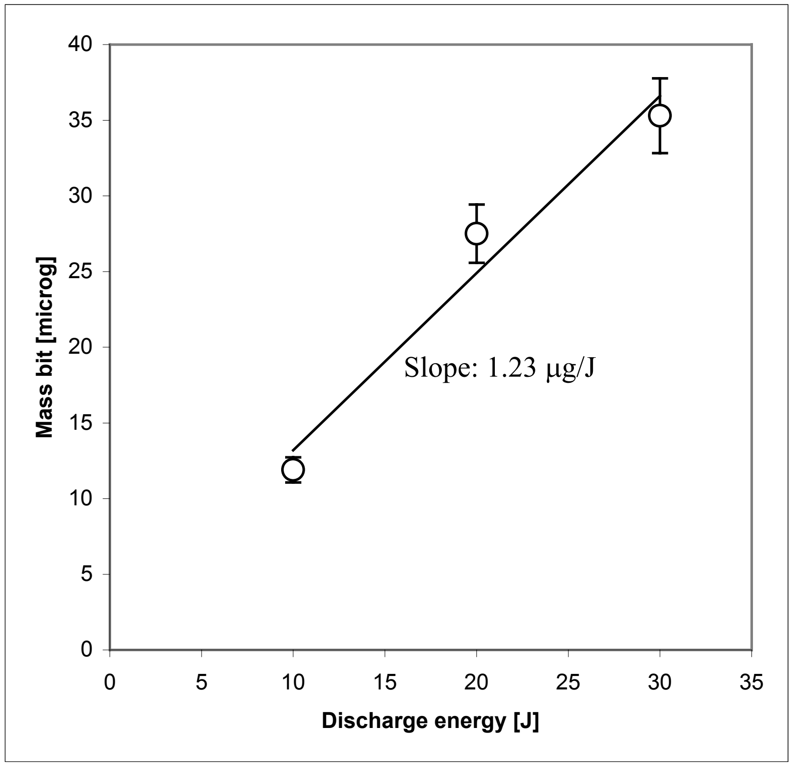

Fig. 7.1: Mass bit as a function of discharge energy

With an average ablation rate of 1.23 μg/J, the results are on the lower end of typical values for comparable PPT systems (LES 8/9: 1.5 μg/J, Tip-II (NOVA): 2.3 1.5 μg/J). The measurement for the 10 J case is considered to be too low since a slight carbonization of the Teflon ablation surface was observed (this would reduce the ablation rate). It has to be noted, however, that these results were obtained at a vacuum background pressure of around 8 x 10^{-5} Torr, nearly one order of magnitude higher than PPT experiments are usually conducted. Since the background pressure influences the amount of ablated mass, these values have to be reexamined at lower background pressures.

7.3 Water Thruster

The water is stored in a relative large and therefore heavy reservoir. Measurements of the weight loss of the water reservoir before and after the experiments would introduce an error of unacceptable magnitude or require experiments of excessive duration (several days). In order to measure accurately mass flow rates in the order of several μg/s, a different method was utilized in the following.

The mass flow rate through the PFC element was evaluated in a fashion similar to the one described in Chapter 5.2.2.3. Again, the flow rate through the diffusion element was evaluated based on the pressure rise over time (dp/dt) in the closed vacuum chamber. With an ideal gas assumption, the total mass flow rate into the vacuum chamber can be evaluated by:

$$\dot{m} = \left(\frac{dp}{dt}\right) \cdot \left(\frac{V_c}{R \cdot T}\right) \tag{7.1}$$

with the volume V_c of the vacuum chamber, the specific gas constant R of the medium inside the chamber, and the temperature T (assumed to be room temperature, ~300 K).

Due to the importance of the mass bit evaluation, the task of measuring these very small mass flow rates requires special care. In order to obtain an accurate measurement of the mass flow rate through the PFC element, one has to be able to distinguish it from the vacuum chamber's leakage rate and outgassing occurring in the chamber. Both of them constitute a virtual mass flow rate since they all contribute to the pressure rise dp/dt in the vacuum chamber. In order to correct the water mass flow rate for these effects, the following experimental setup and procedure was adapted.

The experimental setup differs slightly from the one used in the thruster experiments. Instead of having the water stored in a reservoir inside the vacuum chamber, it is now located outside the vacuum chamber and connected through a pipe to the PFC element inside the chamber. An electromagnetic valve separates the water reservoir from the vacuum chamber. The pressure driving the mass flow is the same as in the thruster experiments, namely one atmosphere.

In general, to measure the water flow rate through the ceramic diffusion element, the vacuum chamber was pumped down for a certain time (between 12 to 15 hrs). Then the main gate valve was closed and the electromagnetic valve was opened, allowing the water to reach the ceramic diffusion element and diffuse through it into the vacuum chamber. The measured pressure rise in the vacuum chamber over time allows then the calculation of the water flow rate.

The following procedure was adapted in order to cope with the above mentioned sources of error in the water flow rate evaluation:

1. The vacuum chamber was pumped down for about 12 to 15 hours (from experience this is about the time it needs to minimizes outgassing). Then the main gate valve was closed and the pressure rise $(dp/dt)_{Air}$ in the chamber was

monitored. At this point the electromagnetic valve separating the water reservoir from the PFC element was still closed such that no water is in contact with the ceramic diffusion element. The monitored pressure rise is mainly due to the leakage rate of air into the vacuum chamber and can be evaluated by:

$$\dot{m}_{Air} = \left(\frac{dp}{dt}\right) \cdot \frac{V_c}{R_{Air} \cdot T} \tag{7.2}$$

2. Generally the pressure was allowed to rise up to 20 mT in step 1. At this point, the electromagnetic valve was opened and subsequently water was diffusing through the PFC element into the vacuum chamber. The monitored pressure rise (dp/dt)' is now due to a combination of air leakage and water diffusing into the vacuum chamber. With $\dot{m}_{Air}$ known, the water mass flow rate can be easily evaluated in the following way:

$$\dot{m}_{H2O} = \left(\left(\frac{dp}{dt}\right)' \frac{V_c}{R_{H2O} \cdot T}\right) - \dot{m}_{Air} \cdot \frac{R_{Air}}{R_{H2O}} \tag{7.3}$$

with R_{H2O}=461 J/kgK.

Figs. 7.2 – 7.4 illustrate the results of steps 1 and 2 for three different measurements conducted in the fashion described above. The difference in these three measurements was the size of the contact surface A_c. For Figs. 7.2 – 7.4 the respective size of the contact surface is A_c= 0.008 cm^2, A_c= 0.018 cm^2, and A_c= 0.086 cm^2.

In each of the figures one can clearly distinguish the time when the electromagnetic valve is opened (at 20 mTorr) and the water is allowed to diffuse through the ceramic element. The slope of the graph increases nearly immediately, indicating a water mass flow into the vacuum chamber. There are three different regions one can identify in all of the figures, and each region is distinguished by a different mass flow rate indicated by the slopes of the depicted linear linefits. The first part of the graph (region 1 between 5 and 20 mTorr) shows the constant slope dp/dt, indicating the air leakage rate of the chamber. After opening the electromagnetic valve, an incline of the slope dp/dt indicates a higher mass flow rate into the chamber due to the water diffusing through the ceramic element (region 2). While the mass flow rate increases in the third region in Fig. 7.2, it decreases in both in Figs. 7.3 and 7.4. Both effects can be explained with the experience obtained from the mass flow measurements in Chapter 5.2.2.3. It was observed that when the porosity of the ceramic element is increased to a certain level, fluid water diffuses through the ceramic and freezes on the surface of the ceramic element facing the low pressure side. Reducing the porosity, the freezing on the surface cannot be observed anymore, but it is reasonable to assume that the region of phase change (from fluid to ice) moved inside the porous material since a change in porosity leads to a change of the pressure gradient over the length of the material. Independent of the location of the phase change region, on the surface or inside the volume of the porous material, the rate of sublimation will be lower than the rate of evaporation, since more energy is required. Therefore the decrease in mass flow rate in the third region of Figs. 7.3 and 7.4. However, Fig. 7.2 indicates that this changes at mass flow rate below a certain level. At low mass flow rates the energy loss due to vaporizing water is not enough to lead to a freezing of the water; instead, region 2 shows a slowly increasing mass flow rate until it reaches a constant mass flow rate in region 3.

During operation the increased temperature of the thruster might partially or at all impede the freezing of the water in the ceramic. The water mass flow rate during thruster operation is therefore assumed to be closer to the value of region 2 than the one from region 3 for the two cases shown in Figs. 7.3 and 7.4. However, for the case shown in Fig. 7.2, the mass flow rate indicated in region 3 was assumed to be the one during thruster operation (see Table 7.2).

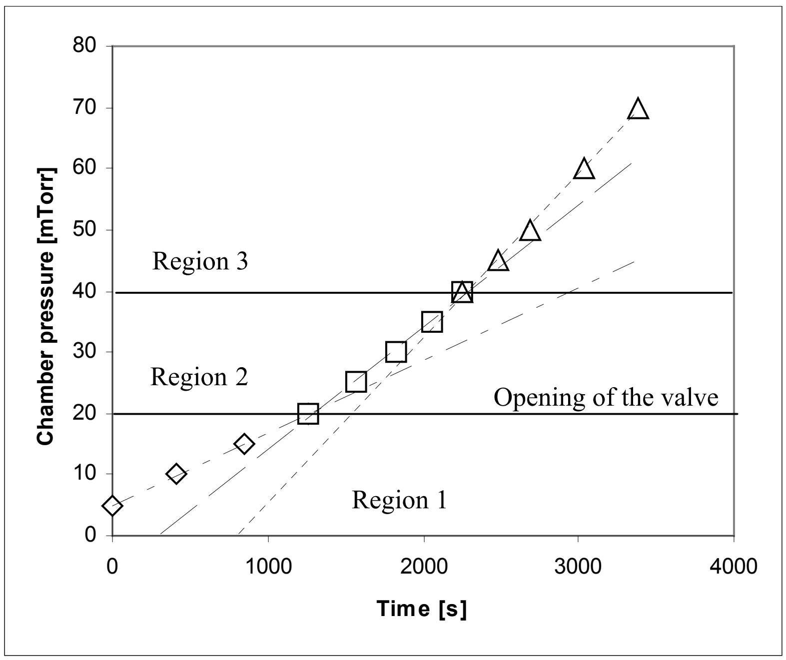

Fig. 7.2: Pressure history of the vacuum chamber for A_c = 0.008 cm^2

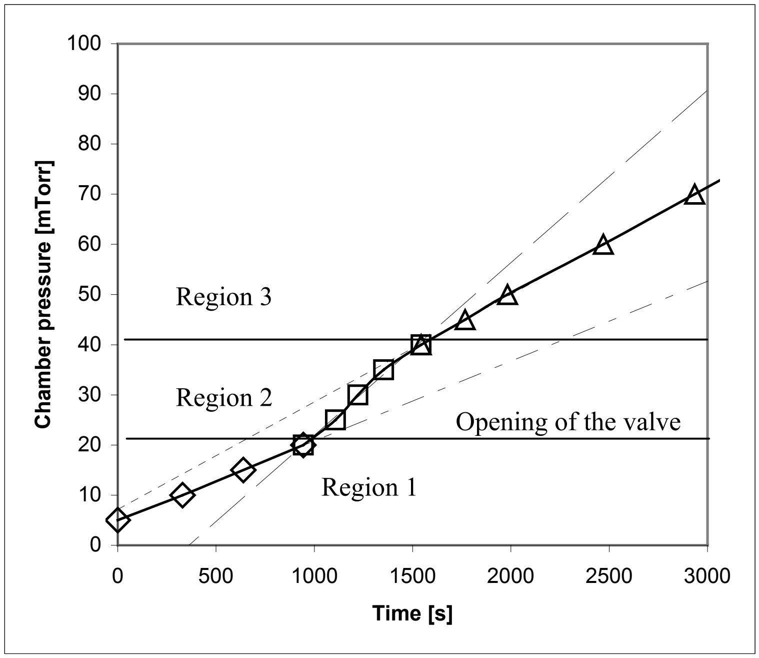

Fig. 7.3: Pressure history of the vacuum chamber for $A_c = 0.018\ cm^2$

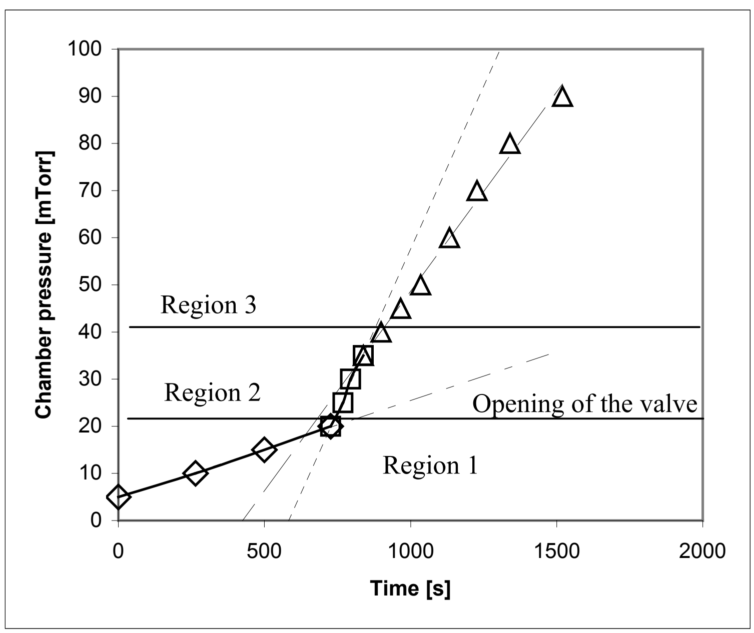

Fig. 7.4: Pressure history of the vacuum chamber for $A_c = 0.086\ cm^2$

	Air leagage $\dot{m}_{Air}$ [μg/s]	$\dot{m}_{H2O}$ (20-35 mTorr) [μg/s]	$\dot{m}_{H2O}$ (35-80 mTorr) [μg/s]
A_c=0.008 cm^2	1.85	0.97	**1.64**
A_c=0.018 cm^2	2.65	**2.16**	0.59
A_c=0.086 cm^2	3.45	**11.87**	7.2

Table 7.2: Mass flow rate evaluation through the PFC element (bold numbers are the mass flow rates for an operating thruster)

CHAPTER 8

PLASMA DIAGNOSTICS

The following chapters summarize the diagnostic methods employed to investigate the water PPT. For means of comparison, the same diagnostics were performed utilizing the Teflon thruster. For each of the diagnostic methods, a concise introduction into the underlying theory and the experimental setup is presented. Subsequently, an initial reduction of the data and interpretation is given.

8.1 Langmuir Probes

Langmuir probe measurements provide information about electron density, n_e, and temperature, T_e, of a plasma. Several different kind of Langmuir probes exist, distinguished by their number of tips, e.g. single, double, triple, etc. Langmuir probes. All of them have been employed for PPT research in the past. For the present work double Langmuir probes were used.

The following chapter recapitulates the past work done with Langmuir probes in the context of PPTs. After an introduction into the underlying theory, the experimental set up and results of the measurements are presented.

8.1.1 Introduction and Theory

Langmuir probes were utilized in various versions by several groups for PPT research in the past. Initially, mainly double Langmuir probes were used to investigate PPTs, but in recent years triple and quadruple[44] Langmuir probes were added as a rather common research tool for PPTs. Although the experimental work was done with different PPT systems and different Langmuir probes, results for the electron density and temperature are in general in good agreement with each other.

Guman and Begun[45] utilized a double Langmuir probe to investigate a PPT (they neither offer a specification of the thruster type nor the discharge energies, but presumably they utilized the LES-6 or a close derivative of it). Measuring the electron temperature and density at a location 0.7 m downstream of the thruster's exit plane, they evaluated a peak electron temperature of 1.2 eV and peak electron density of 3×10^{20} m^3. The peak values were measured on the thruster's axis. For locations off-axis both the electron temperature and density drop significantly. Their results indicate a cone half angle of the plume of 30° - 40°. Comparing the times corresponding to the peak of the probe signals at two downstream locations, they calculated a particle velocity of 25 km/s.

Eckman et al.[46] measured the ion velocity with several single Langmuir probes, arranged such that a velocity measurement was performed during a single shot. They found two ion waves traveling with different velocities: 60 km/s and 30 km/s

Triple Langmuir probes were utilized by Kamhawi et al.[47] to measure electron density and temperature for a rectangular PPT operating at discharge energies between 5 and 10 J. Electron densities were found to be 2.5×10^{21} m^3 at 5 cm distance, 6×10^{20} m^3 at 10 cm, and 1.2×10^{20} m^3 at 15 cm distance from the thruster's exit plane. Electron temperature was found to range between 0.7 and 4 eV. The peak plasma velocity was estimated to be 37 km/s.

Byrne, L.T.[48] compared electron temperature and density measurements of a triple Langmuir probe with those of a double Langmuir probe and found them in good agreement. He evaluated a peak electron temperature and density of 9.2 eV and 7.2 x 10^{20} m^3 respectively at 5 cm distance from the thruster's exit plane (on-axis). The discharge energy was 20 J.

For the present work a double Langmuir probe was utilized as already mentioned above. The theory for the double Langmuir probe was developed by Johnson and Malter[49]. It is based on the same principles as the theory originally developed for a single probe by Langmuir himself. However, double Langmuir probe do not require a reference electrode as in the case of a single Langmuir probe. This is important for transient plasma conditions as encountered in the case of a PPT.

Independent of the kind of Langmuir probe, the essence of this measurement is the following: if a metallic electrode is submerged in a plasma and kept on a certain voltage, a current based on the biasing voltage and the plasma conditions (T_e and n_e) will flow from the plasma to the electrode. Changing the biasing voltage will change the magnitude of the measured current. Varying the voltage over a certain range will result in a current-voltage characteristic from which electron temperature and density can be evaluated.

A double Langmuir probe consists basically of two single Langmuir probes biased with respect to each other and therefore they do not require a reference electrode. Since both electrodes are insulated from ground, they are electrically floating with respect to the plasma, which allows the probe potential to follow closely the rapid changes in the plasma potential. The biasing voltage V_b applied between the two probes can be written in the following way:

$$V_b = V_1 - V_2 > 0 \tag{8.1}$$

with V_1 positive with respect to V_2. The current between those two probes is a function of the applied biasing voltage V_b and is in general defined positive if V_b is positive. Fig. 8.1 shows schematically the arrangement of the two single Langmuir probes and the applied voltage.

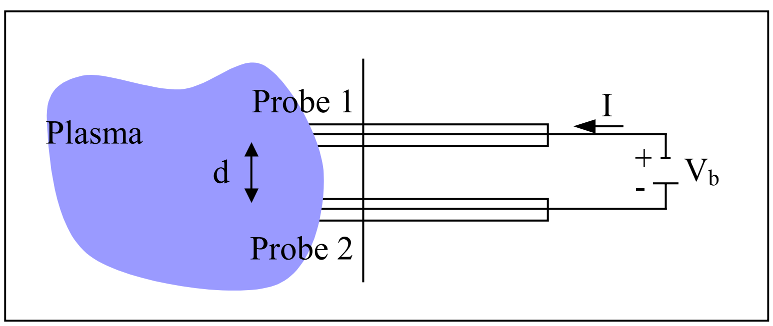

Fig. 8.1: Schematic of the double probe arrangement and the applied voltage source

Figure 8.2 depicts qualitatively the relation between the applied biasing voltage and the resulting probe current. If V_1 and V_2 are chosen such that the biasing voltage V_b equals zero, then no net current can flow to either of the tips and subsequently no current can flow between the probes. V_1 and V_2 are called the floating potentials of the probe tips. With V_1 chosen slightly less negative and V_2 more negative, both with respect to the plasma potential, the biasing voltage becomes positive and more electrons will flow to probe 1 and less to probe 2. Subsequently a positive current will flow between probe 2 and 1. Further increases of V_b will lead to an increase in observed current until around a certain level, denoted B in Fig 8.2. At this point, probe 1 will be just below the plasma potential such that it collects enough electrons to balance the saturation ion current collected by probe 2. Further increase of the biasing voltage only leads to a minor increase in current, which is due to an increasing sheath thickness around the probe tips, allowing a larger number of charged particles to be collected.

A reversal of the biasing voltage would lead to a symmetric shape of the graph (0-B' in Fig. 8.2) as long as the areas of the two probe tips are equal and the plasma condition in the volume defined by the two tips is homogeneous.

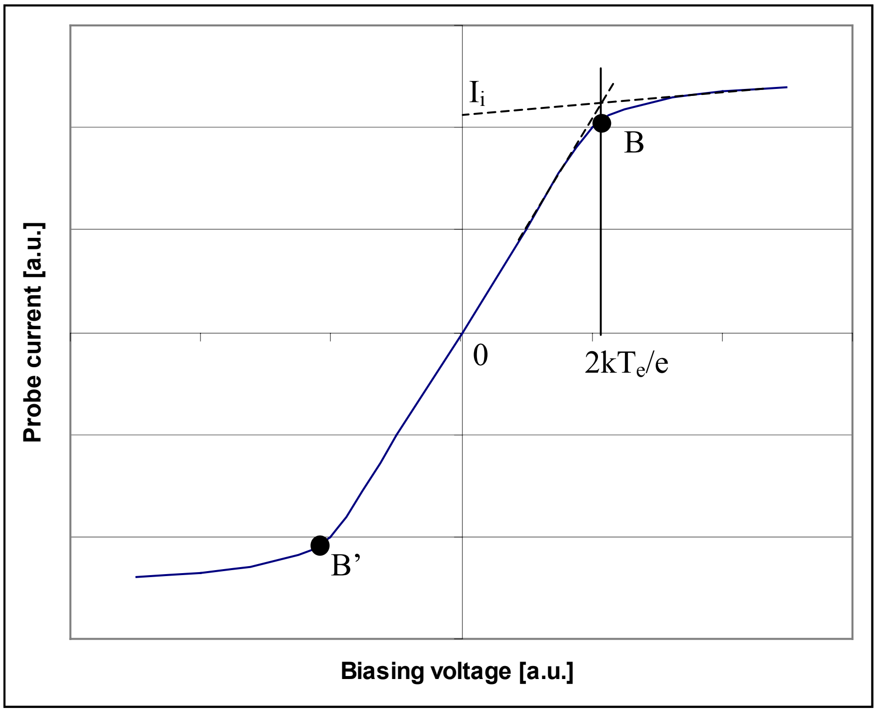

Fig. 8.2: Idealized current-voltage characteristic for a probe with equal tip area in a homogenous plasma

A general advantage of the double Langmuir probe is the fact that the total current in the system can never be greater than the ion saturation current, as suggested by Kirchhoff's law, since the electron current's magnitude is always just large enough to balance the collected ion current. This has the advantage to minimize the disturbance of the plasma due to the measurement itself, but at the same time means that only the higher energy electrons are collected while the bulk part of electrons stays undetected by the probe.

To obtain the electron temperature and density from the current-voltage characteristic, a method described by F. Chen[51] is applied.

In the following, I_{i1}, I_{i2}, I_{e1}, and I_{e2} denote the ion and electron currents to probe 1 and probe 2. Since the probe is electrically floating, Kirchhoff's law requires:

$$I_{i1} + I_{i2} - I_{e1} - I_{e2} = 0 \tag{8.2.}$$

The total current I in the system is given by

$$2I = I_{i2} - I_{e2} - (I_{i1} - I_{e1}) \tag{8.3}$$

Adding and subtracting Eqs. (8.2) and (8.3)

$$I = I_{e1} - I_{i1} = I_{i2} - I_{e2} \tag{8.4}$$

If the potential of the probe is equal or close to the floating potential V_f, most of the electrons are repelled and their distribution remains Maxwellian (assuming that it was Maxwellian to begin with). The electron current to the probe is then only due to their thermal motion and can be expressed in the following way:

$$I_e = \frac{1}{4} \cdot A \cdot e \cdot n_e \cdot \overline{C}_e \cdot e^{\left(\frac{e \cdot V_f}{k \cdot T_e}\right)} = \frac{1}{2} \cdot A \cdot e \cdot n_e \sqrt{\frac{2 \cdot k \cdot T_e}{\pi \cdot m_e}} \cdot e^{\left(\frac{e \cdot V_f}{k \cdot T_e}\right)} \tag{8.5}$$

with the electron charge e ($1.6 \text{x} 10^{-19}$ C), the probe area A, the electron number density n_e and electron temperature T_e, the Boltzman constant k ($1.38 \text{x} 10^{-23}$ J/°K), and the electron mass m_e. $\overline{C}_e$ is called the mean thermal velocity and can be expressed in the following way:

$$\overline{C}_e = \sqrt{\frac{8 \cdot k \cdot T_e}{\pi \cdot m_e}} \tag{8.6}$$

Equation 8.5 remains valid for the entire transition region (0-B and 0-B') and can be rewritten as following:

$$I_{e1} = A_1 \cdot j_r \cdot e^{\left(\frac{e \cdot V_1}{k \cdot T_e}\right)}$$

$$I_{e2} = A_2 \cdot j_r \cdot e^{\left(\frac{e \cdot V_2}{k \cdot T_e}\right)} \tag{8.7}$$

with the random (thermal) electron current j_r

$$j_r = \frac{1}{2} \cdot e \cdot n_e \sqrt{\frac{2 \cdot k \cdot T_e}{\pi \cdot m_e}} \tag{8.8}$$

The general formula for the double Langmuir probe current as a function of the biasing voltage can be obtained by substituting Eq. (8.7) into Eq. (8.4) and using the relationship $V_b = V_1 - V_2$ from above:

$$\frac{I + I_{i1}}{I_{i2} - I} = \frac{A_1}{A_2} \cdot e^{\left(\frac{e \cdot V_b}{k \cdot T_e}\right)} \tag{8.9}$$

The ion currents for both probes are equal if $A_1 = A_2$ and assuming a homogeneous plasma the equation above can be simplified to

$$\frac{I + I_i}{I_i - I} = e^{\left(\frac{e \cdot V_b}{k \cdot T_e}\right)} \tag{8.10}$$

Solving Eq (8.10) for the current I:

$$I = I_i \cdot \tanh\left(\frac{e \cdot V_b}{2 \cdot k \cdot T_e}\right) \tag{8.11}$$

Equation 8.11 has been found to be a good fit to the experimentally obtained I-V characteristic. One method to find the electron temperature T_e is by taking the derivative of Eq. 8.11 with respect to the biasing voltage V_b:

$$\frac{dI}{dV_b} = \frac{I_i \cdot e}{2 \cdot k \cdot T_e} \sec h^2\left(\frac{e \cdot V_b}{2 \cdot k \cdot T_e}\right) = \frac{I_i \cdot e}{2 \cdot k \cdot T_e} \cdot \frac{4}{e^{\left(\frac{e \cdot V_b}{k \cdot T_e}\right)} + 4 + e^{-\left(\frac{e \cdot V_b}{k \cdot T_e}\right)}} \qquad (8.12)$$

At this point one can make use of the fact that, as mentioned above, only a small portion of the electrons are collected. Therefore, sufficient accuracy can be obtained if Eq. 8.12 is simplified by expressing the slope of the curve for V_b=0

$$\left.\frac{dI}{dV_b}\right|_{V_b=0} = \frac{e \cdot I_i}{2 \cdot k \cdot T_e} \qquad (8.13)$$

by further solving for the electron temperature one obtains

$$T_e = \frac{e \cdot I_i}{2 \cdot k} \cdot \left.\frac{dV}{dI}\right|_{V=0} \qquad (8.14)$$

with dV/dI (V=0) and I_i known from the measurements as indicated in Fig. 8.2.

Assuming that the plasma is quasineutral ($n_i = n_e$), the ion current can be expressed in the following way:

$$I_i = \frac{1}{4} \cdot A \cdot n_e \cdot e \cdot \overline{C_i} = A \cdot n_e \cdot e \cdot \sqrt{\frac{k \cdot T_e}{2 \cdot \pi \cdot m_i}} \qquad (8.15)$$

which can be solved for the electron number density

$$n_e = \frac{I_i}{e \cdot A} \cdot \left(\sqrt{\frac{k \cdot T_e}{2 \cdot \pi \cdot m_i}}\right)^{-0.5} \qquad (8.16)$$

The current collection theory outlined above is based on the assumption of collisionless conditions. Before applying this theory it is therefore required to investigate if collisionless condition is satisfied in this particular experiment, or if the theory has to be modified for collisions.

The theory is based on the assumption that on the edge of the collisonless region, the velocity distribution is the same as in the undisturbed region. A condition which can only be satisfied if the plain size of the probe does not establish itself as a obstacle in the flight path of the particles. This condition translates to the simple requirement that the Knudsen number is bigger than unity or, in other words, that the probe radius r_p is considerable smaller than the free mean path λ for the different collision partners, i.e λ_{ii}, λ_{ie}, and λ_{ee}, where the subscript i stands for ions and e for electrons, respectively.

$$r_p << \lambda_{ii}, \lambda_{ie}, \lambda_{ee} \tag{8.17}$$

According to Chen[51], the different free mean path can be approximated by

$$\lambda_{ii} \approx \lambda_{ee} \approx \lambda_{ei} \cong 3.4 \cdot 10^{13} \cdot \frac{T_e^{\,2}}{n_e \cdot \ln \Lambda} \tag{8.18}$$

with the electron temperature T_e [eV], the electron number density n_e [cm^{-3}], and the impact parameter Λ. The latter denotes the fact that the particles are deflected in the presence of charged particles and Coulomb forces, respectively. Due to its combination with the logarithm it is a very insensitive parameter and it will be sufficiently accurate if we set $\ln(\Lambda)$ equal to 10.

To verify the collisionless condition, a second parameter, the Debye length λ_D, has to be checked. The Debye length is given by

$$\lambda_D = \left(\frac{\varepsilon_o \cdot k \cdot T_e}{n_e \cdot e^2} \right)^{0.5} \tag{8.19}$$

with the permittivity of free space ε_o, the Boltzmann constant k, the electron temperature T_e, the electron number density n_e, and the electron charge e. With regards to the collisonsless assumption, the equations of motion of the particles in the sheath around the probe are akin to a free-fall equation. This cannot be assumed anymore for the case in which the above mentioned mean free paths are smaller than the Debye length. Therefore the second requirement for collisionless condition is equivalent to

$$\lambda_{ii}, \lambda_{ee}, \lambda_{ei} > \lambda_D \tag{8.20}$$

From previous investigations of the plasma parameters in a PPT plume, it can be assumed that the range of temperature will be between 1 to 5 eV and the number density between $10^{18} - 10^{21}$ m^{-3} (see introduction)

With these values, a maximum mean free path for collisions for the three above mentioned collision partners of 0.850 m (T_e = 5 eV, n = n_e =1 x 10^{18} m^{-3}) and a minimum value of 1.36 x 10^{-5} m (T_e = 2 eV, n_e =1 x 10^{21} m^{-3}) was calculated. The maximum Debye length is 1.7 x 10^{-5} m and the minimum Debye length is 8.2 x 10^{-7} m. Therefore, both of the above stated requirements are satisfied for a broad range of T_e and n_e. Only for T_e in the range of 2 eV and n_e in the range of 1 x 10^{21} cm^3 the requirement $r_p << \lambda_{ii}, \lambda_{ie}, \lambda_{ee}$ is not fully satisfied (r_p=6.35 x 10^{-5} m).

8.1.2 Experimental Setup for the Langmuir Probe Measurements

The system utilized consists of the double Langmuir probe, a supporting floating probe circuit, and an oscilloscope (Tektronix, TDS 420A), as schematically shown in Figure. 8.3.

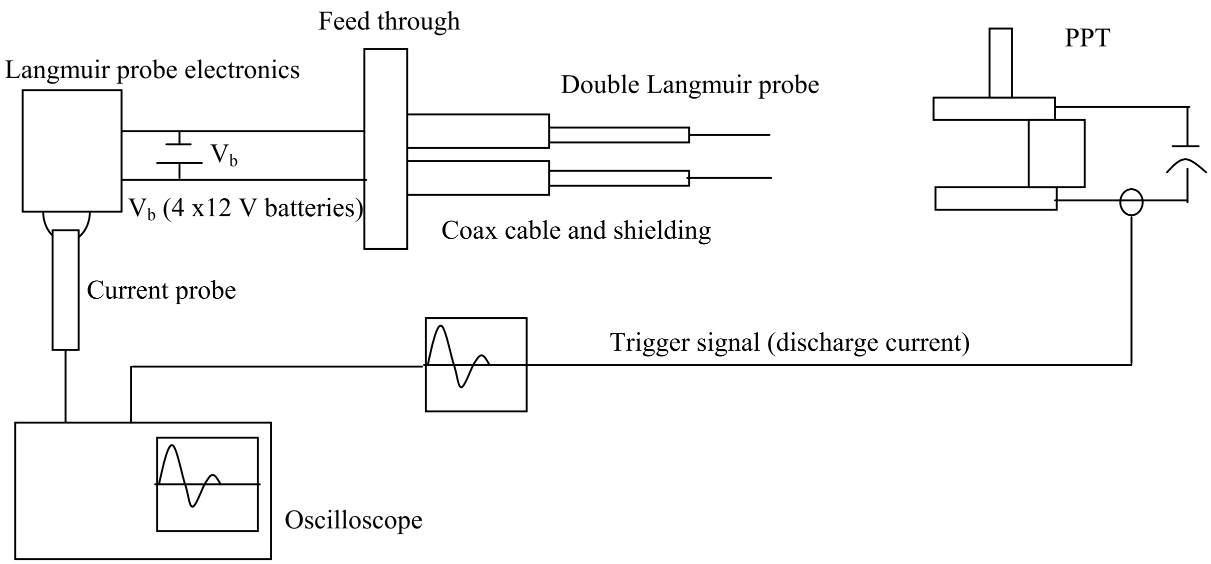

Fig. 8.3: Schematic of the double Langmuir probe measurement assembly

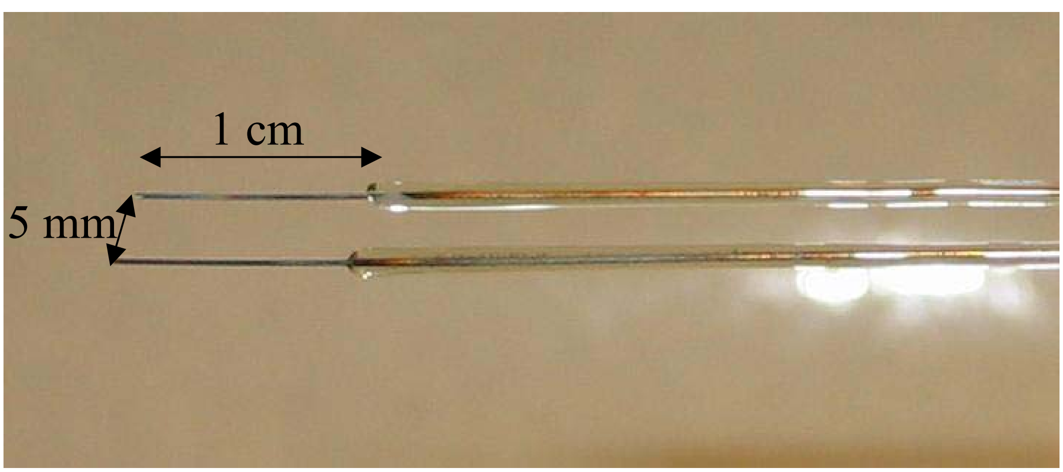

Fig. 8.4: Utilized Langmuir probe

The Langmuir probe has two tips made of 0.127 mm diameter tungsten wire with an exposed surface length of 1 cm. The two tips are separated by a distance of 5 mm (see Fig. 8.4). The remaining length of the tungsten wire is insulated with a 2 mm pyrex tube and vacuum sealed by fusing the tips of the tube to the tungsten wire. Each tungsten wire has copper electroplated to its end so that the center of a coaxial cable could be soldered to it. In order to increase the signal-to-noise ratio, the entire length of the coaxial cable (~1.5 m) between the probe and the feed-through of the vacuum chamber was enclosed in a copper shielding. The shielding consists partially of solid copper tubing and partially of a flexible copper mesh. The latter was necessary to allow enough flexibility of the shielding assembly such that the position of the probe can be easily changed. The shielding is wrapped in insulating tape and connected to Earth ground.

A coaxial cable connected the probe from the feed-through of the vacuum chamber to the floating probe circuit. This circuit keeps the tips of the probe on a constant voltage potential during a measurement. When the tips get in contact with the plasma ejected from the thruster, a current between the two tips will develop. For a given probe geometry, the magnitude of this current is only a function of the state of the plasma and the applied voltage difference. The probe circuit consists of a 550 μF capacitor and a charging circuit. The latter employed four 12 V batteries (Everday®, Cleveland, Ohio) in series, allowing a total biasing voltage of 48 V, and a potentiometer in order to adjust the voltage V_b across the capacitor and the probe tips respectively (see Fig. 8.5). The voltage was monitored with a handhold multimeter (Fluke 75, Series II, Everett, Washington). The currents established between the probe tips were measured with Tektronix probe current (P6021) with a sensitivity of 10mA/mV and a time constant of 1.3 msec. The current probe is connected between the probe circuit and the oscilloscope (see Fig. 8.5).

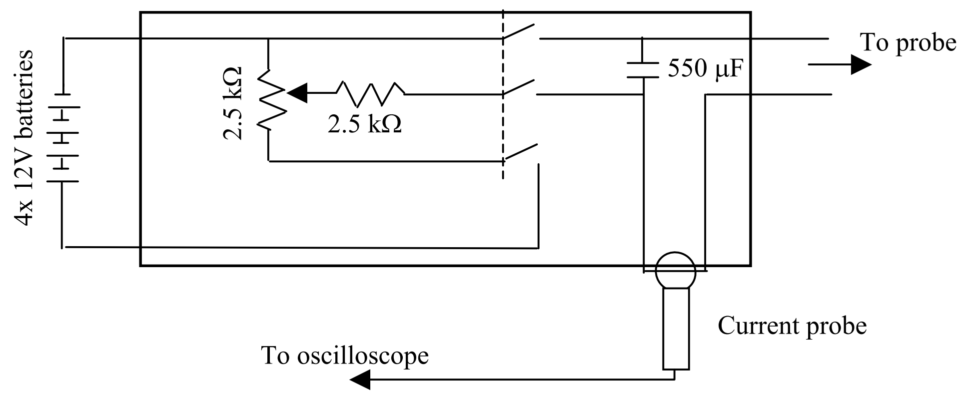

Fig. 8.5: Langmuir probe circuit

8.1.3 Data Acquisition and Procedure

In order to determine the electron temperature and number density a semi-graphical analysis as described in Chapter 8.1.1 was utilized. This required the measurement of the probe currents for several biasing voltages. Since the used probe circuit did not allow a fast voltage sweep during one discharge (duration of one discharge is about 10 μs), each measurement had to be done for one single biasing voltage. After each run the probe had to be glow cleaned to avoid distortion of the signal by deposition of, e.g., carbon on the probe tips. Glow cleaning of the probe was performed in the following fashion: Prior to each run, the chamber was first pumped down to a pressure around 800 mTorr. At this pressure level the probe tips were cleaned through electrical means (glow cleaning). The glow cleaning circuit consists of a high voltage power supply

(Keithley Instruments, #246) connected to the probe via a 100 kΩ resistor to avoid excessive currents in the cleaning circuit (see Fig. 8.6).

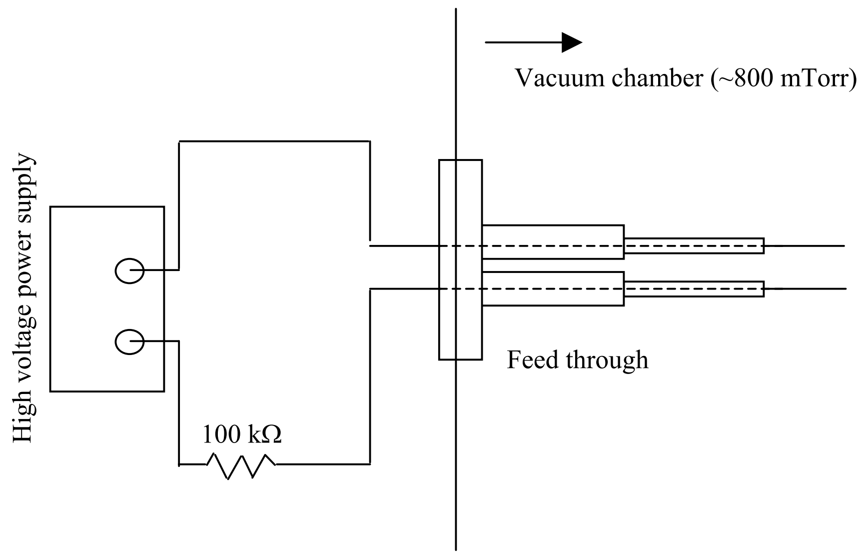

Fig. 8.6: Glow cleaning circuit for the double Langmuir probe

By applying a voltage difference (500 V) to the tips of the probe, a small current between the two tips is generated, which – by means of ion bombardment – then cleans them. During the cleaning process, the polarity of the probe was switched several times to assure that both tips are evenly clean. After the glow cleaning was completed the background pressure was further reduced to the required level.

It is important to note that the shot-to-shot variations with regard to the discharge current history and magnitude (Chapter 6) can also be observed in the Langmuir probe measurements. Additionally, the background pressure has a strong influence on the measured Langmuir probe signal (in general: with higher background pressure, less details in the signal are visible and the magnitude of the signal is reduced).

Due to the different molecular weight of water compared with the average molecular weight of air, the pressure readings will differ when the thruster operates in the water mode. To accommodate this fact, a correction factor $\xi = 0.891$ (1mTorr air pressure corresponds to 0.891 mTorr water pressure) for the ion gauge reading is necessary. With a background pressure for the thruster tests with water of 1.0 - 1.2 x 10^{-4} Torr and for the tests with Teflon of 7.5 – 9.0 x10^{-5} Torr acceptably close conditions were obtained.

To avoid transition effects[16] (in the time before the thruster reaches its thermal equilibrium), measurements should be performed in general after the thruster has already operated for about 1000 discharges. In the case of the Langmuir probe measurements this was not advisable, since 1000 discharges might result in enough deposition on the probe tips to distort the signal. In order to evaluate the distortion of the signal as a function of thruster operation time in the case of the Teflon mode, several measurements were taken between initiation of thruster operation and 10 minutes into thruster operation. This test was done several times at different biasing voltages. Summarizing those tests, it has to be concluded that for low biasing voltages (between 1 and 6 V) and over the duration of 3-4 minutes, a change in signal strength and history can be observed beyond the normal shot-to-shot variation. Additionally, the trend of deteriorating signal increases with increasing distance from the thruster. However, at biasing voltage >12 V, the difference of the probe signal from the first discharge in comparison with one taken several minutes later is well below the normal shot-to-shot variation. Due to this sensitivity to the biasing voltage, it was decided to disregard the transition effects and to perform all the measurements with the Langmuir probe in the first 3 minutes of thruster operation.

During this time, a number between 8 and 10 data sets were recorded. To account for the shot-to-shot variations, the probe current $I(V_b)$ was obtained by taking the average of the measured probe current values. Fig. 8.7 illustrates this procedure. It shows a Langmuir probe data set obtained on the thruster's axis at 5.04 cm downstream of the thruster's exit plane. The dotted lines are the raw data while the solid line is the average of these measurements. Fig. 8.7 shows also the for PPT characteristic double peak structure in the probe signal already shown in the past by Eckman and Gatsonis[46] and others.

However, it has to be mentioned that the second peak did not always occur. Based on the data recorded for this work, for about 30% of the discharges no second peak is detected.

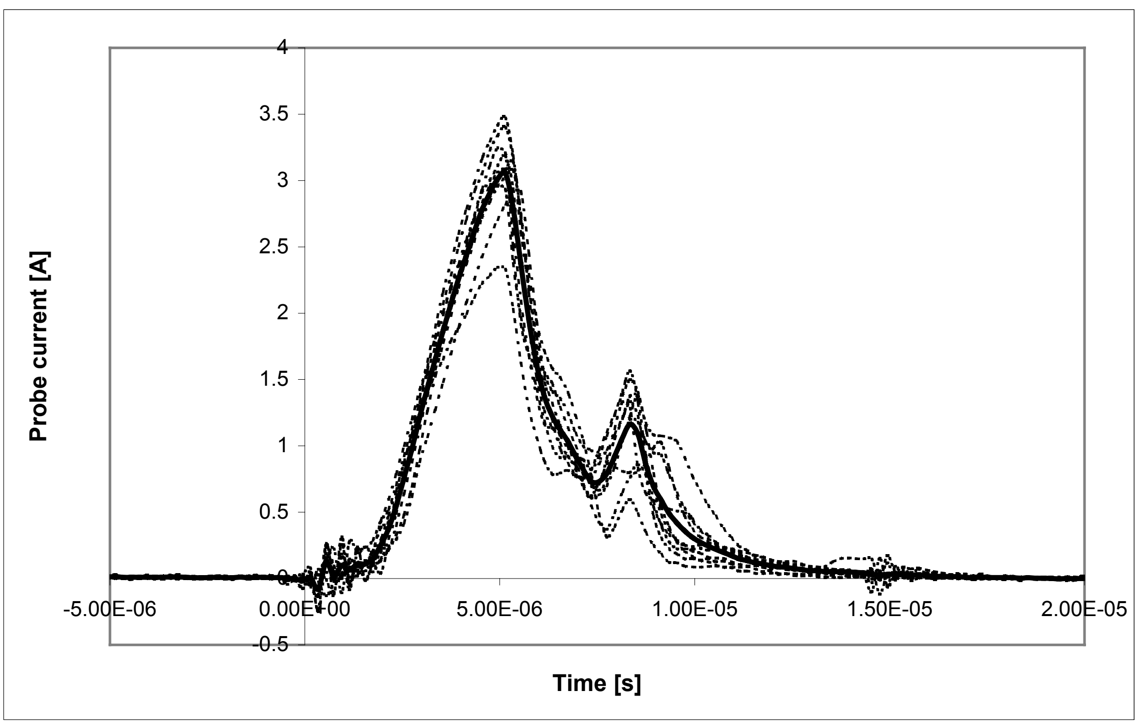

Fig. 8.7: Average procedure for the Langmuir probe current $I(V_b)$ with the raw data (dotted lines) and the average (solid line) (Teflon, 20 J discharge energy)

The probe was mounted on the probe support as described in Chapter 5.5. In general, the probe support allows measurement downstream of the thruster up to a distance of 25 cm. Due to length of the probe itself and the limited size of the vacuum chamber, the maximum distances in case of the Langmuir probe measurements was 15.2 cm.

8.1.4 Experimental Results and Reduction of Data

Various sources in the literature[14,47,48] provide excellent descriptions of variations in electron temperature and density as a function of location (along and perpendicular to the thruster's axis), time, and discharge energy. Since the objective of this work was not an evaluation of the complete plume structure but rather the general identification of differences between a PPT operating with Teflon compared to water, only measurements at 20 J discharge energy and a limited number of locations are conducted and compared with each other in the following. Mass bit at this energy level was 27.5 μg per discharge for Teflon and 11.87 μg per discharge for water.

8.1.4.1 Electron Temperature and Density

Peak electron temperature, T_e, and density, n_e, were evaluated at several different downstream locations on the thruster's axis: 5.08 cm, 10.16 cm, and 15.24 cm. The probe signal for water at 15.24 cm distance was only slightly above the noise level and did not allow an unambiguous evaluation of electron temperature and density.

Utilizing Eqs. 8.14 and 8.16, the electron temperatures and densities can be calculated based on the I-V characteristics from Figs. 8.8 to 8.11. The current values shown in the figures are the averaged peak probe currents of between 5-8 single measurements (see first peak in Fig. 8.7). The evaluated electron temperatures and densities, as presented in Table 8.1, constitute therefore maximum values for T_e and n_e. For calculation of the electron density, n_e, an average molecular mass of 5.14×10^{-26} kg for Teflon[31] and 9.9×10^{-27} kg for water (assuming complete dissociation of the water molecule) was assumed.

For all the measurement locations it was found that the electron temperatures in the Teflon case exceed those for water. It is interesting to note that, while the electron temperature of water declines only marginally, a relative large drop in temperature for Teflon is observed. This might indicate that the assumption of a local thermal equilibrium (LTE) is less accurate for Teflon than for water. The main errors in calculating T_e and n_e are introduced by the graphical evaluation of dV/dI and by the shot-to-shot variation of the peak currents (indicated by the error bars in Figs. 8.8 – 8.11). The shot-to-shot variations are in general more pronounced in the case of water than for Teflon. For the evaluation of the electron temperature, an overall error of ±30% for Teflon and ±45% for water was evaluated. The error in evaluation of the electron density is ±15% for Teflon and ±20% for water.

Distance from thruster's exit plane	T_e [eV]		n_e [m^3]	
	Teflon	**Water**	Teflon	**Water**
5.08 cm	8.74	**3.0**	4.74×10^{21}	**5.64×10^{20}**
10.16 cm	3.52	**2.62**	1.84×10^{21}	**2.11×10^{20}**
15.24 cm	2.67	**N/A**	9.94×10^{20}	**N/A**

Table 8.1: Peak electron temperature and density at different locations on the thruster's axis (20 J discharge energy)

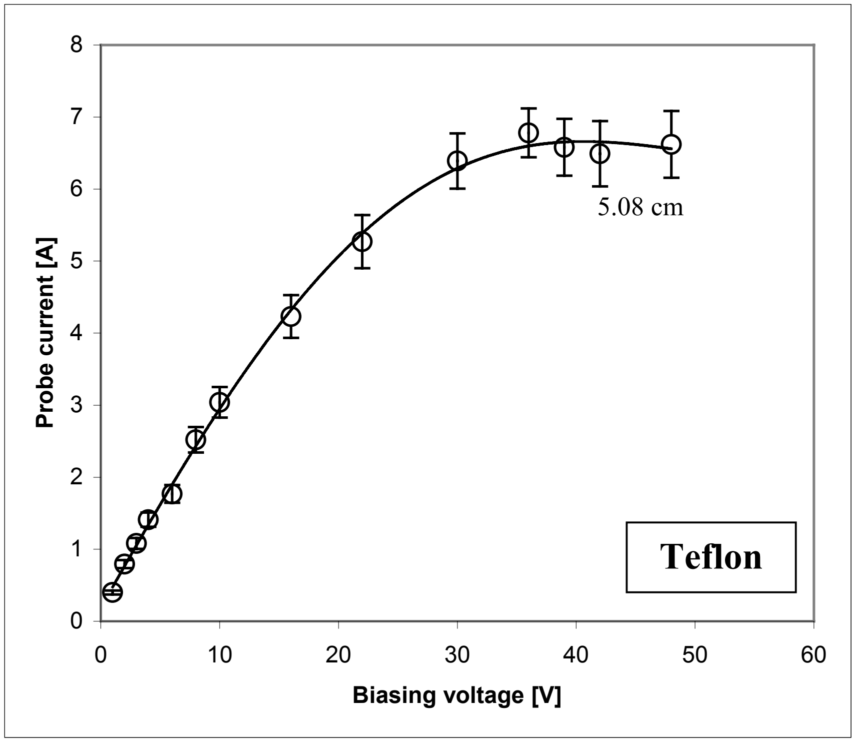

Fig. 8.8: I-V characteristic for Teflon at 5.08 cm distance on the thruster's axis

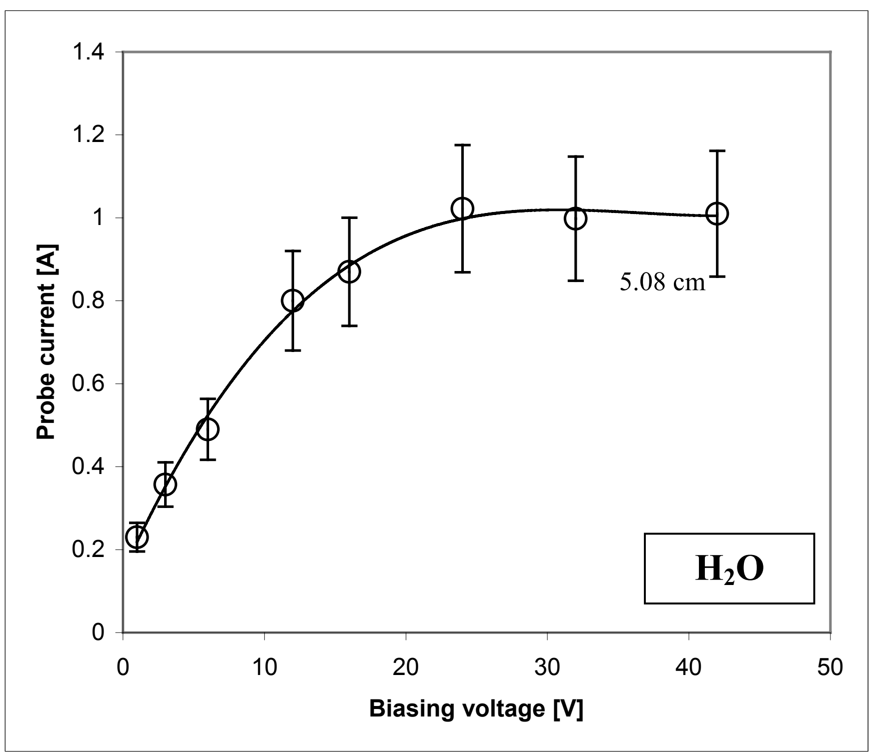

Fig. 8.9: I-V characteristic for Water at 5.08 cm distance on the thruster's axis

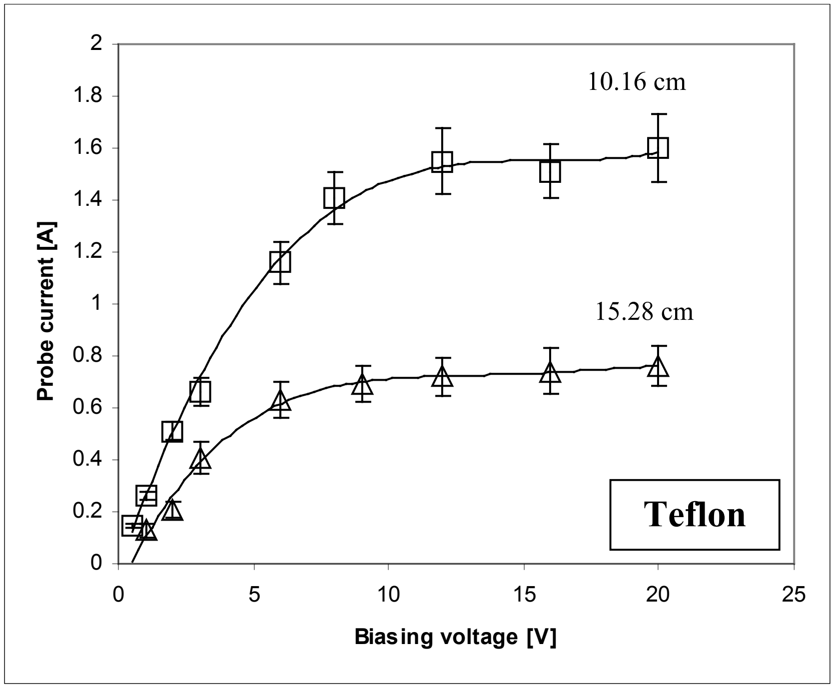

Fig. 8.10: I-V characteristic for Teflon at 10.16 cm and 15.24 cm distance on the thruster's axis

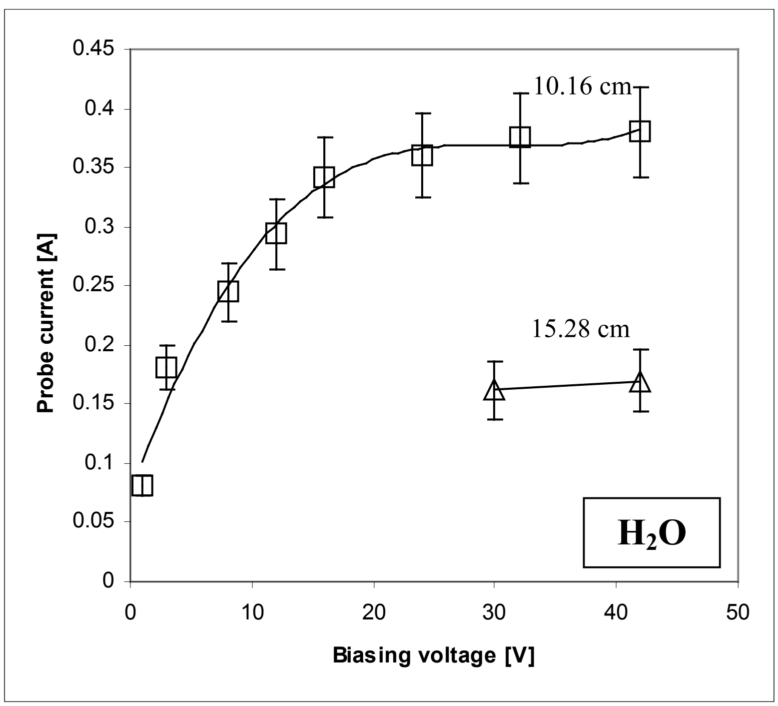

Fig. 8.11: I-V characteristic for water at 10.16 cm and 15.24 cm distance on the thruster's axis

8.1.4.2 Time-of-Flight Measurements

The plasma ejected from the thruster consists of particles with a large range of velocities. However, the Langmuir probe signal can be utilized for time-of-flight (TOF) evaluation by comparing the time of the onset or other characteristics of the signal at different locations downstream of the thruster. It is important to utilize the saturation current for TOF measurements since only they capture the initial, low density, plasma front. This fact is illustrated in Fig. 8.12, showing Langmuir probe measurements at 5.08 cm distance from the thruster for different biasing voltages V_b. It can be clearly seen that the onset of the signal shows an apparent dependency on V_b: For increasing biasing voltages, the time of onset seems to occur earlier. Only when V_b reaches a value where saturation current sets in, the time of onset stays about constant. It was therefore decided to only use the saturation currents for TOF evaluations in the following.

TOF measurements were performed at three different locations on the thruster's axis for Teflon and water: at 5.08 cm, 10.16 cm, and 15.24 cm. Figures 8.13 and 8.14 depict the saturation currents at those three different locations for both propellants. Each curve shown in the two figures is obtained by averaging 8 to 10 single measurements, as discussed earlier in this chapter.

Comparing the two figures, several differences are easily recognizable: (i) the probe signal in the case of water rises earlier and the time difference between the onsets at different locations is smaller, (ii) the water signal does not exhibit the characteristic second peak as in the case of Teflon and is in general more confined, and (iii) while the signal for Teflon is rather smooth, the probe signal for water is more erratic. The latter is attributed partially to a less focused discharge of the water thruster and partially to the higher shot-to-shot variations when using water.

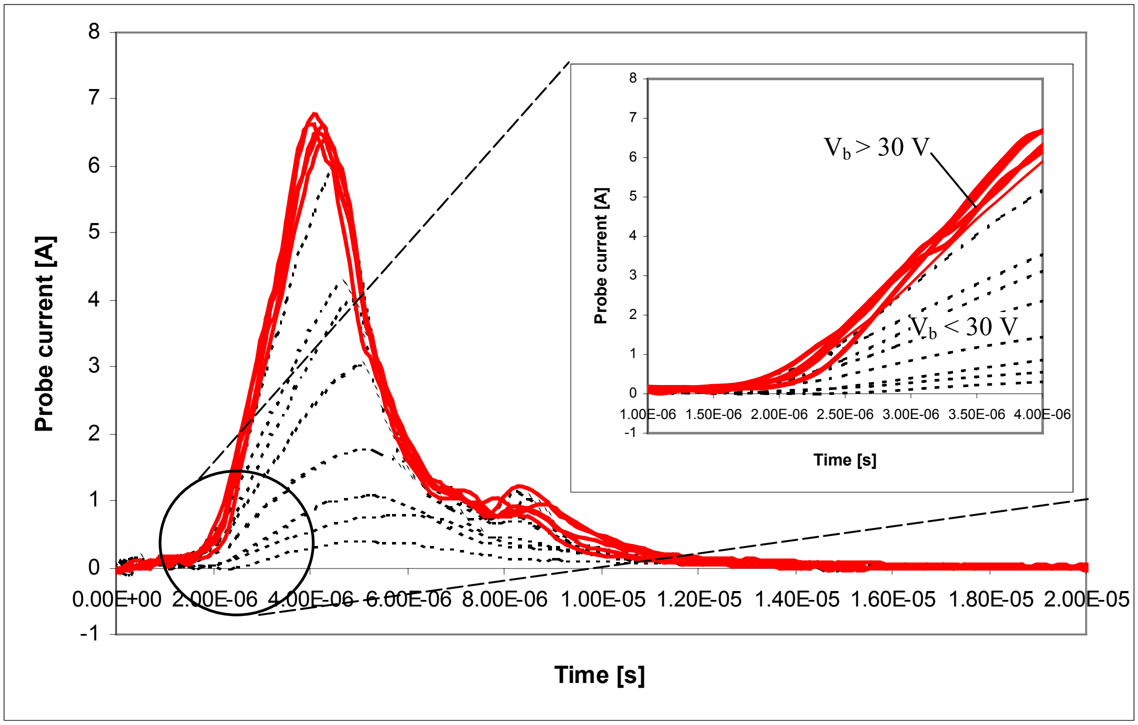

Fig. 8.12: Probe response at saturation (solid line) and below saturation (dotted line) (Teflon, 20 J, 5.08 cm downstream of the thruster's exit plane).

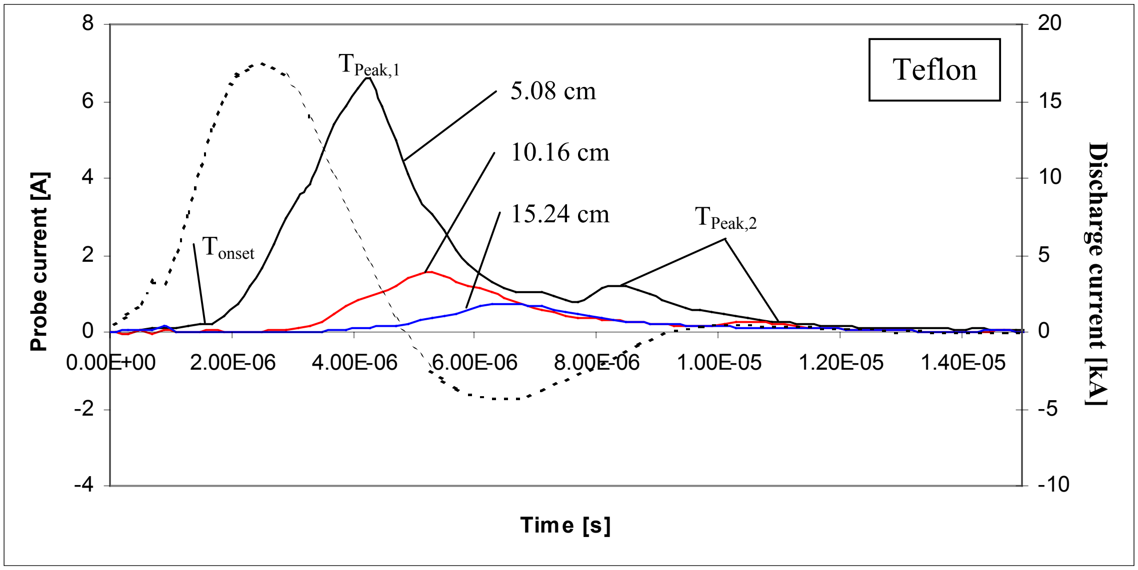

Fig. 8.13: Saturation currents at 5.08 cm, 10.16 cm, and 15.24 cm (Teflon, 20 J) with discharge current for time reference (dotted line)

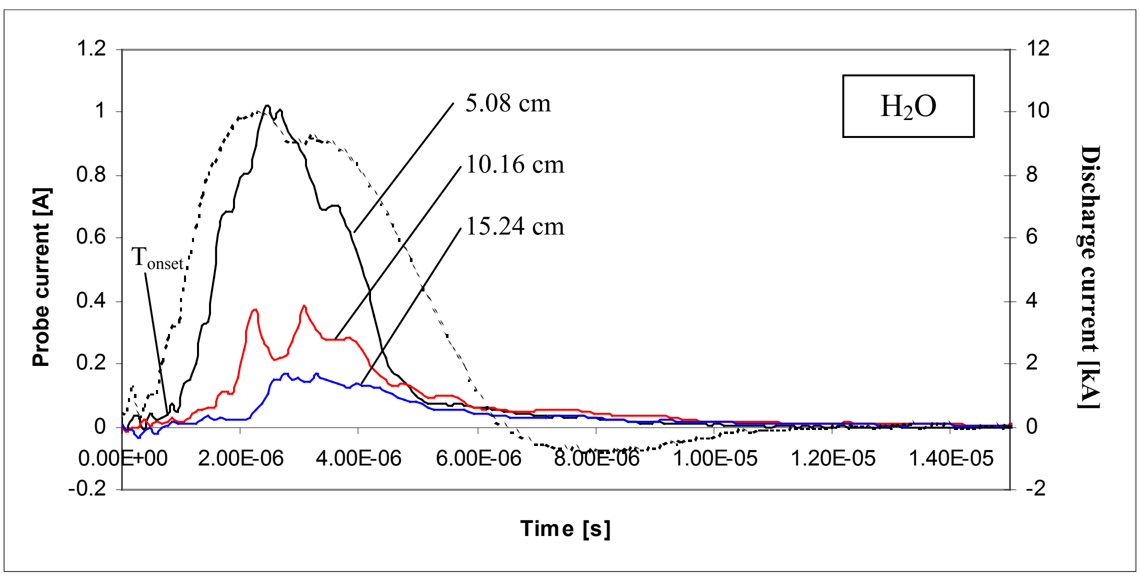

Fig. 8.14: Saturation currents at 5.08 cm, 10.16 cm, and 15.24 cm (water, 20 J) with discharge current for time reference (dotted line)

Due to the differences in magnitude of the signals at the three different locations, certain details of the graphs for 10.16 cm and 15.24 cm are not clearly distinguishable. This was improved by nondimensionalizing the graphs with each of their peak values, $I(t)/I_{max}$, as demonstrated for the case of Teflon in Fig. 8.15. Based on the data for Teflon depicted in fig. 8.15, the velocities of the particles in the plasma front, in the first and second peaks were calculated (see Table 8.2). Due to the more erratic signal for water propellant, there is no clear first or second peak. For the water case it was therefore only possible to obtain the maximum velocities by comparing the onset of the signal at the three different locations (see Table 8.2). The main error in evaluating the velocities results from the time resolution of the oscilloscope and the subsequent error in evaluating the time difference.

These results from Table 8.2 are in good agreement with those from comparable experiments conducted by other groups (see the introduction to this chapter) using double or single Langmuir probes, and also with velocity measurements utilizing alternative techniques like Faraday cups[52], etc.

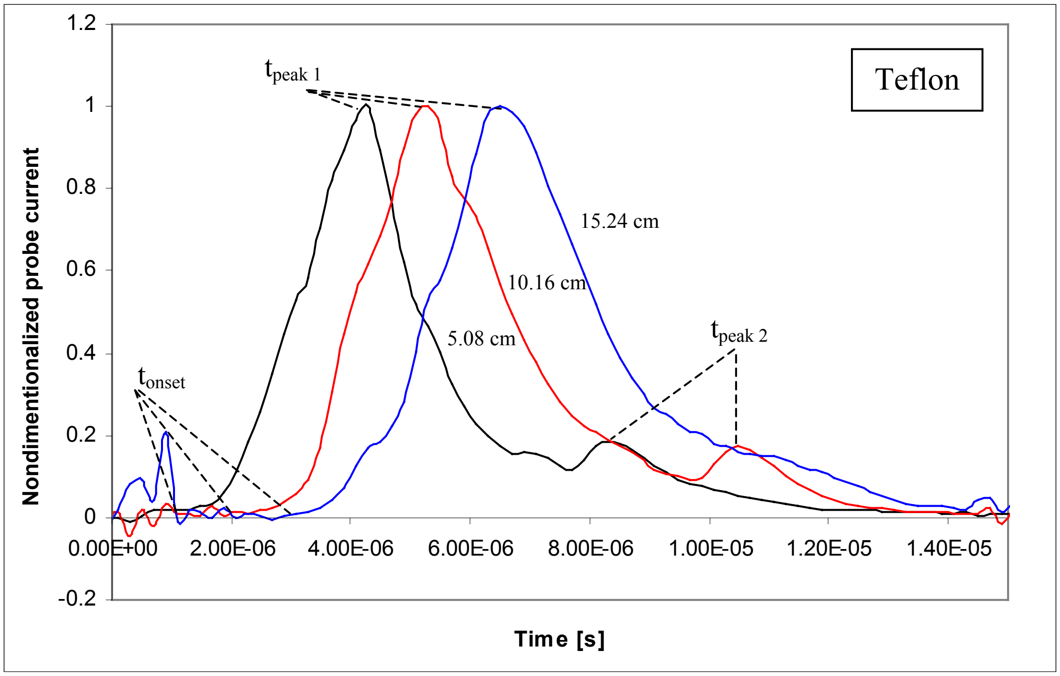

Fig. 8.15: Averaged and nondimensionalized saturation currents at 5.08 cm, 10.16 cm, and 15.24 cm (Teflon, 20 J)

	Δs [m]	Δt [μs]		V [km/s]	
		Teflon	**Water**	Teflon	**Water**
Onset	0.0508 – 0.1524	2	**1.2**	$50.8\ \pm^{25\%}_{20\%}$	**84.7** $\pm^{50\%}_{25\%}$
1st peak	0.0508 – 0.1524	2.4	**N/A**	$42.3\ \pm^{20\%}_{15\%}$	**N/A**
2nd peak	0.0508 – 0.1016	2	**N/A**	$25.4\ \pm^{30\%}_{20\%}$	**N/A**

Table 8.2: Particle velocities in the plasma plume based on the Langmuir probe measurements (20 J)

8.2 Magnetic Field Probes

The knowledge of the magnetic field distribution allows determination of a number of parameters, like the enclosed current distribution, current densities, magnetic Reynolds number, magnetic pressure etc. All these parameters are in general important for a better understanding of the acceleration of the plasma, etc. In the context of the present work, the knowledge of these parameters will allow a further identification of differences due to the utilization of different propellants.

8.2.1 Introduction and Theory

To the best knowledge of the author, magnetic field probes have been utilized only in a few occasions for investigation of parallel rail PPTs. Vondra et al.[9] measured the diffusion of the current (or the magnetic field) into the plasma to determine the magnetic Reynolds number, R_m. It was found that R_m is of order unity indicating that the magnetic field lines are neither frozen in the plasma (as assumed in most of the circuit models), nor do they simply diffuse into it.

Eckbreth[42] employed magnetic field probes to investigate current pattern and gas flow stabilization issues in a device with a total electrode length of 1.2 m. A similar device with an electrode length of roughly 0.6 m was employed by Berkery and Choueiri[43]. Magnetic field measurements were conducted to investigate the current sheet evolution in such a device. They found a current distribution which, except for the initial phase, deviates significantly from the standard current sheet model. Rather than a current sheet perpendicular to the electrode surface, their results indicate a more diffuse structure exhibiting a main trunk and a canted brunch near the anode.

Magnetic field probes derive their utility from the Faraday induction effect given by the following equation

$$\nabla x\vec{E} = -\frac{d\vec{B}}{dt} \tag{8.21}$$

or in integrated form

$$\oint_c \vec{E}\cdot d\vec{l} = -\frac{d}{dt}\int \vec{B}\cdot dA_c \tag{8.22}$$

with the electric field vector $\vec{E}$, the magnetic field vector $\vec{B}$, the circumference l of the coil, and the area of the coil A_c as indicated in Fig. 8.16. The LHS of both equations above constitutes the output of the probe, only depending on the area of the probe coil A_c, the number of turns the coil employs, and the time rate of change of the magnetic field. By integrating the probe output, one obtains the time resolved magnitude of the component of the magnetic field B perpendicular to A_c. With the knowledge of the magnetic field one can either calculate the current density or the total current flow through the particular volume of space by employing one of the following forms of Ampere's law

$$\nabla x\vec{B} = \mu_o \cdot \vec{j} \tag{8.23}$$

$$\oint \vec{B}\cdot d\vec{l} = \mu_o I \tag{8.24}$$

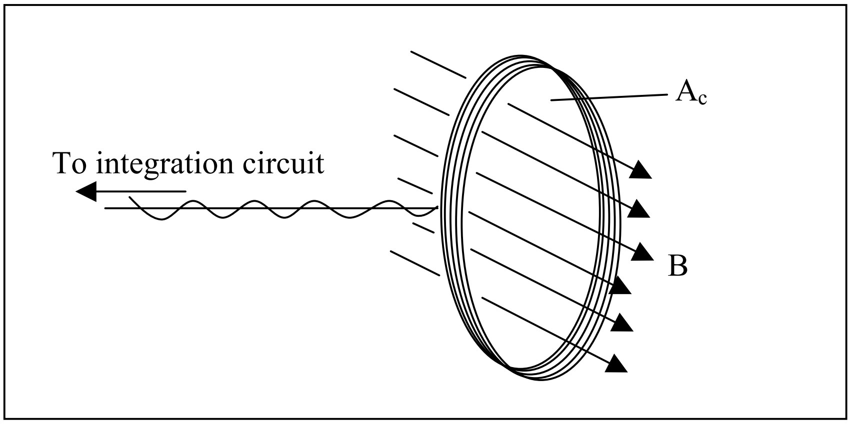

Fig. 8.16: Schematic of a magnetic field probe penetrated by the magnetic field component perpendicular to A_c

8.2.2 Experimental Setup for the Magnetic Field Measurements

The self-induced magnetic field of the Teflon thruster and the WPPT-4 were measured with a magnetic field probe. The probe was made of 5 turns of a 28 gauge copper wire with an inner coil diameter of 4 mm. The probe was placed in a Pyrex tube with a flat fused ending and an outer diameter of 8 mm. The twisted leads were soldered to a coax cable connecting the probe with the feed through. The complete length of the twisted wire and coax cable was enclosed in a shielding made of copper tubes and flexible copper mesh. The shielding was wrapped in insulating tape and connected to Earth ground. The output signal of the probe was integrated with a passive RC integrator having a time constant of 58 μs. A 50 Ω terminator was utilized to prevent signal ringing due to unmatched impedance of the integrator and the oscilloscope. Fig. 8.17 illustrates the set up for the magnetic field measurements.

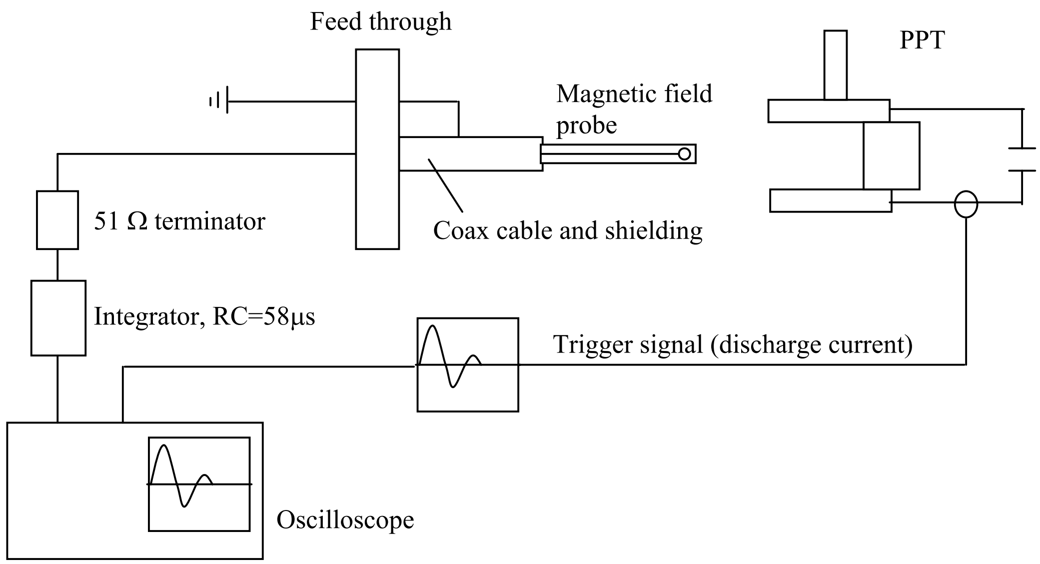

Fig. 8.17: Experimental setup for the magnetic field measurements

The probe was calibrated with a setup consisting of a 10 μF capacitor and a solid copper wire. The length of the wire was chosen such that the circuit inductance allows the production of a current waveform with a period similar to the PPT discharge current. The capacitor was charged with a high voltage power supply and a knife switch was employed to close the circuit. The current in the circuit was measured with a Pearson current monitor (Palo Alto, CA, model 5046, accuracy ±1%). By comparing the output of the probe with the calculated magnetic field based on the measured circuit current, a calibration constant of 1.38 T/V was evaluated. To investigate the error in this measurement due to leaking of magnetic field lines into the probe from directions other than parallel to the probe's axis, the probe was turned 90 degrees and the measurement was repeated. It was found that this effect has an insignificant contribution, with only about 2% of the total magnitude. Mainly based on an uncertainty in probe positioning of about ±2 mm, this calibration has an accuracy of ±5%.

8.2.3 Data Acquisition and Procedure

Prior to a measurement the thruster was operated for several minutes such that it can reach thermal equilibrium. The discharge energy for both cases, water and Teflon, was chosen to be 20 J. Mass bit at this energy level was 27.5 μg per discharge for Teflon and 11.87 μg per discharge for water. The magnetic field probe was mounted on the probe support (see Chapter 5.5). All the measurements were performed on the thruster's axis at downstream locations of 1.5 cm, 2.54 cm, and 5.08 cm (measured from the thruster's exit plane). The data presented in this chapter are averaged values of 5 - 8 successive measurements since the already discussed shot-to-shot variations during PPT operation are also observable in the magnetic field probe measurements. The shot-to-shot variations and the result of the averaging process are illustrated in Fig. 8.18. The discharge current triggers the oscilloscope and provides the time reference for the pressure probe measurements (see Fig. 8.17).

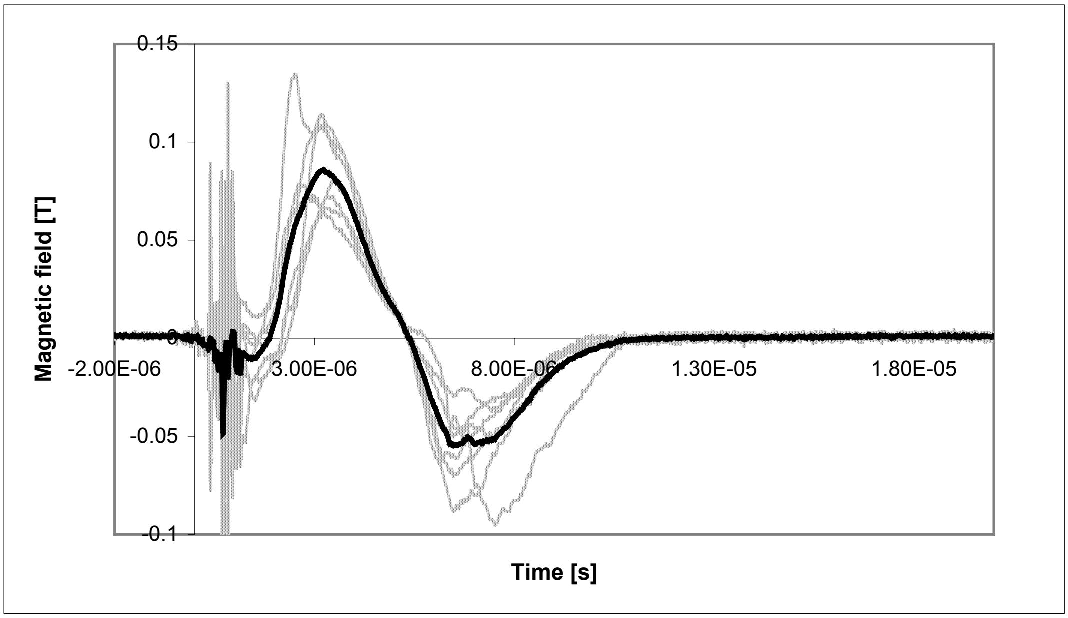

Fig. 8.18: Shot-to-shot variations in magnetic field measurements (gray lines) and the resulting average (black line) for Teflon at 1.5 cm distance and 20 J discharge energy

8.2.4 Experimental Results and Reduction of Data

8.2.4.1 Magnetic Field measurements

The magnetic field was measured on the axis of the thruster at three different locations: 1.5 cm, 2.5 cm, and 5.08 cm. It was not possible to conduct measurements at locations further downstream since the noise started to become dominant. Figs. 8.19 and 8.20 depict the magnetic field at the different downstream locations for Teflon and water respectively. Comparing the results for Teflon and water, it is evident that the signal in the water case has a higher magnitude for all the investigated locations on the axis than the one for Teflon. Furthermore, the onset of the signal occurs earlier than in the case of Teflon.

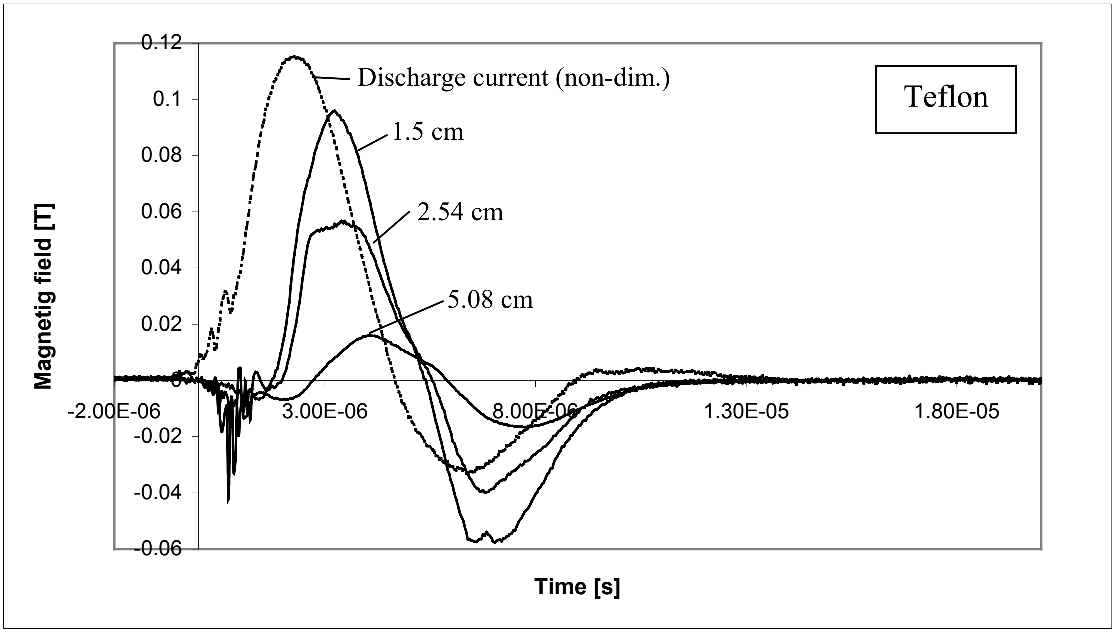

Fig. 8.19: The magnetic field at different distances (20 J, Teflon) (solid lines) with the discharge current (dotted line) for time reference

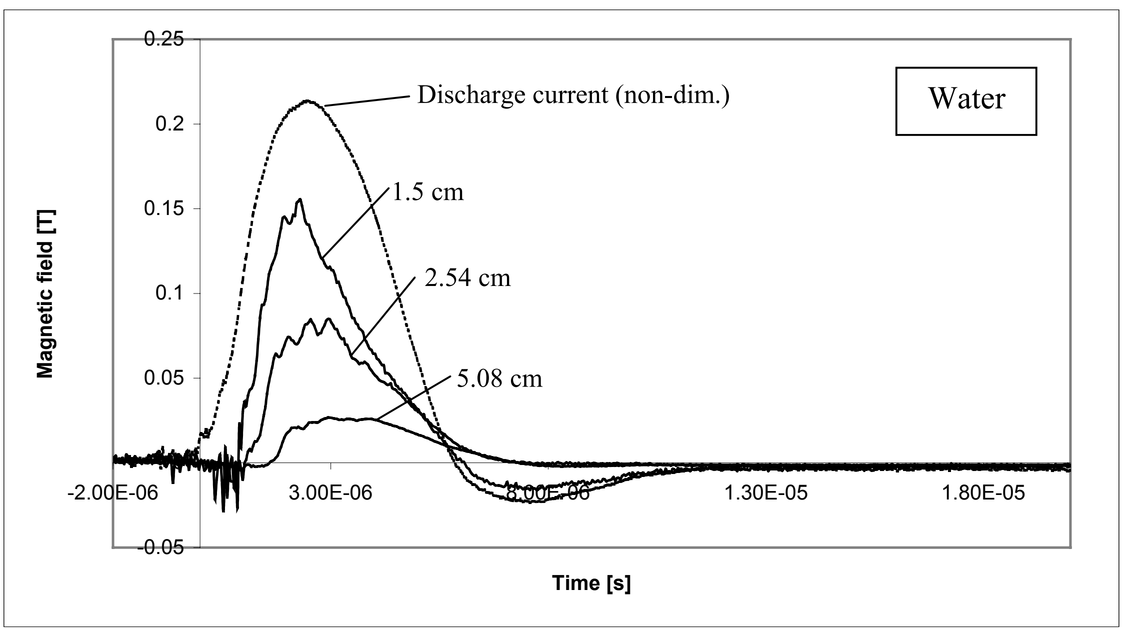

Fig. 8.20: The magnetic field at different distances (20 J, water) (solid lines) with the discharge current (dotted line) for time reference

8.3. Pressure Probes

The fundamental difference between Langmuir probes and pressure probes is the ability of the latter to measure mass flux in general without being limited to only charged particles, as is the case with Langmuir probes. Consequently, pressure probe measurements in the thruster's plume provide additional information about the mass flux in the plume. This again, will lead to a better understanding of the governing acceleration processes in a Pulsed Plasma Thruster.

8.3.1 Introduction and Theory

The short and highly unsteady pulse of a Pulsed Plasma thruster makes pressure measurements in the plume a complicated task. Most diagnostic tools like the Pitot tube[53,54] or a pendulum are simply too inert to be of use under these conditions.

For the present work, a pressure probe based on a piezoceramic technology was used. The pressure probes have been designed by York[55,56] and have been mainly used for investigation of MPDs. The probe is similar to a general piezoelectric probe but designed such that it has a high frequency response and is especially suitable in the extreme thermal and electrical vicinity of plasma discharges.

The probe signal for the high velocity and density of the exhaust flow is equal to the sum of the static and the dynamic pressure and can be expressed in the following way:

$$
\begin{aligned}
p_{impact} &= p_{static} + p_{dynamic} \\
&= (n_h + n_e) \cdot k \cdot T_e + n_h \cdot m_i \cdot u_{exit}^2
\end{aligned}
\tag{8.26}
$$

with the heavy particle density, n_h, and the electron density, n_e, assumed to be equal (quasi neutral plasma), the electron temperature, T_e, the average mass of the ions, m_i, and their exhaust velocity u_{exit}.

8.3.2 Experimental Setup for the Pressure Probe Measurements

Fig. 8.23 shows schematically the set up for the pressure probe measurements. It consists of the pressure probe and an oscilloscope (Tektronix, TDS 420A). Since the employed pressure probe is a charged coupled device with no significant current flowing, it is very sensitive to electromagnetic noise. It was therefore necessary to shield the coaxial cables connecting the pressure probe with the vacuum chamber feed-through by a combination of copper tubing and flexible copper mesh. The shielding is wrapped in insulating tape and connected to Earth ground.

The probes were designed to withstand the extreme conditions of a plasma environment (thermal loads and electromagnetic noise) and to have a high frequency response. The central element of the pressure probe is a disk of piezoceramic material (PZT-5A) mounted to a backing road with a conducting epoxy (see Fig. 8.24). The disk and the backing road are encased in a conducting shell, separated by a mylar foil around the circumference to prevent electric contact with the piezoceramic disk. The necessary electric contact between the front of the piezoceramic disk and the conducting shell is provided by a thin layer of silver paint. The whole unit is placed in a quartz tube, which has a flat fused end. The quartz tube provides electric and thermal protection and at the same time allows stress waves to be transmitted to the piezoceramic disk.

In the occurrence of pressure, a charge difference builds up across the element and is manifested as a voltage transmitted through the connecting coaxial cable to the oscilloscope.

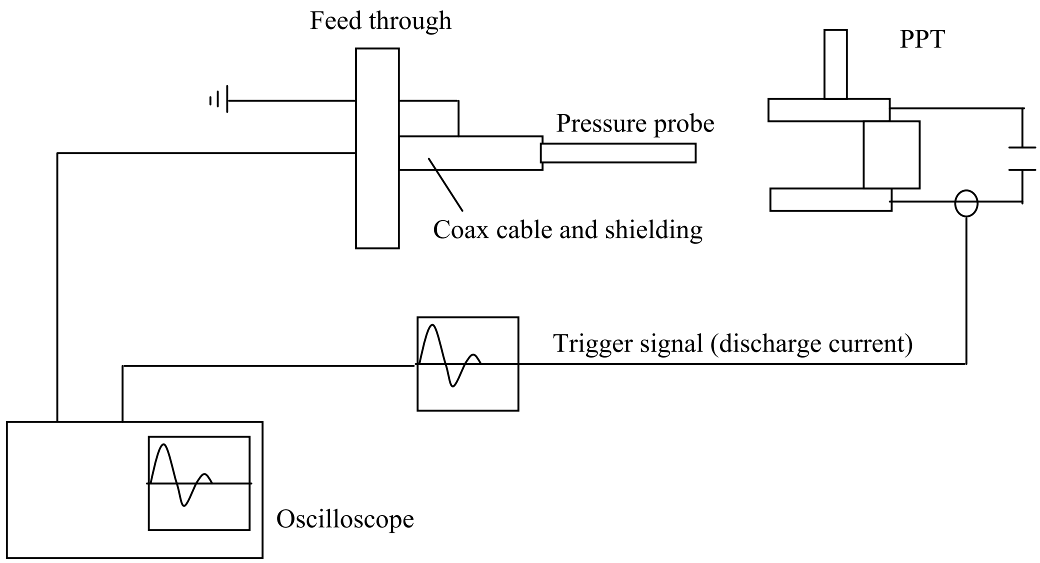

Fig. 8.21: Schematic of the experimental set up for the pressure probe measurements

It is well known that the plume of a PPT consists of an initial front of ionized particles possessing a relative high velocity. By impact on the pressure probe they induce stress waves into the probe and subsequently generate noise, foreclosing the weaker pressure signal to be measured. Several methods were explored to eliminate the effects of the induced stress waves. A buffer on the front of the probe showed the best results. In general a buffer consists of a layer of soft material protected by a non-ablating material.

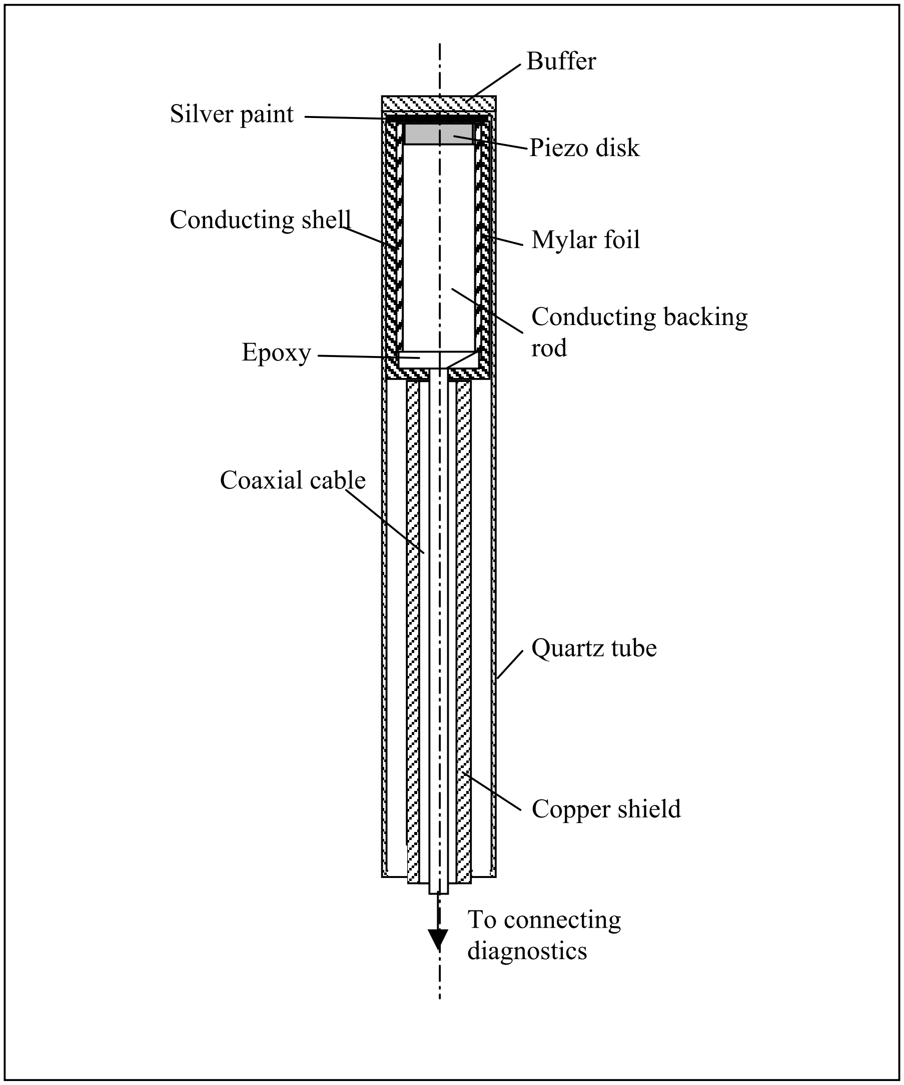

Fig. 8.22: Cross section of the pressure probe

The filter properties of this buffer are very sensitive to the combination of the damping properties of the soft material and the mass of the ablation protection. An empirical study was conducted, revealing that a combination of several layers of a insulating tape and a protecting 1 mm thick disk of boron nitrite performed best. The boron nitrite disk is bonded to the damping material with silicon glue. Silicon glue is also used to attach the buffer onto the probe.

Due to concerns about a possible deterioration of the buffer or the silicon glue, a verification measurement was performed. After about a total of 6 hours of usage of the probe, the probe was relocated to a former position and a measurement under identical conditions was performed. The results show no change with respect to the time of arrival or time of end of the signal and only marginal changes in the magnitude, which are well below the normal shot-to-shot variations.

8.3.3 Data Acquisition and Procedure

Prior to a measurement the thruster was operated for several minutes such that it can reach thermal equilibrium. The pressure probe was mounted on the probe support (see Chapter 5.5). The measurements were in general performed only on the thruster's axis. The already discussed shot-to-shot variations during PPT operation are also observable in the pressure probe measurements. As before, all the data presented in this chapter are averaged values of 5 - 8 successive measurements. The shot-to-shot variations and the result of the averaging process are illustrated in Fig. 8.25. As in the previous chapter, the discharge current triggers the oscilloscope and provides the time reference for the pressure probe measurements (see Fig. 8.23). Mass bits per discharge for Teflon were 11.9μg (10J), 27.5 μg (20J), and 35.3 μg (30J), and for water 1.64 μg independent of the discharge energy.

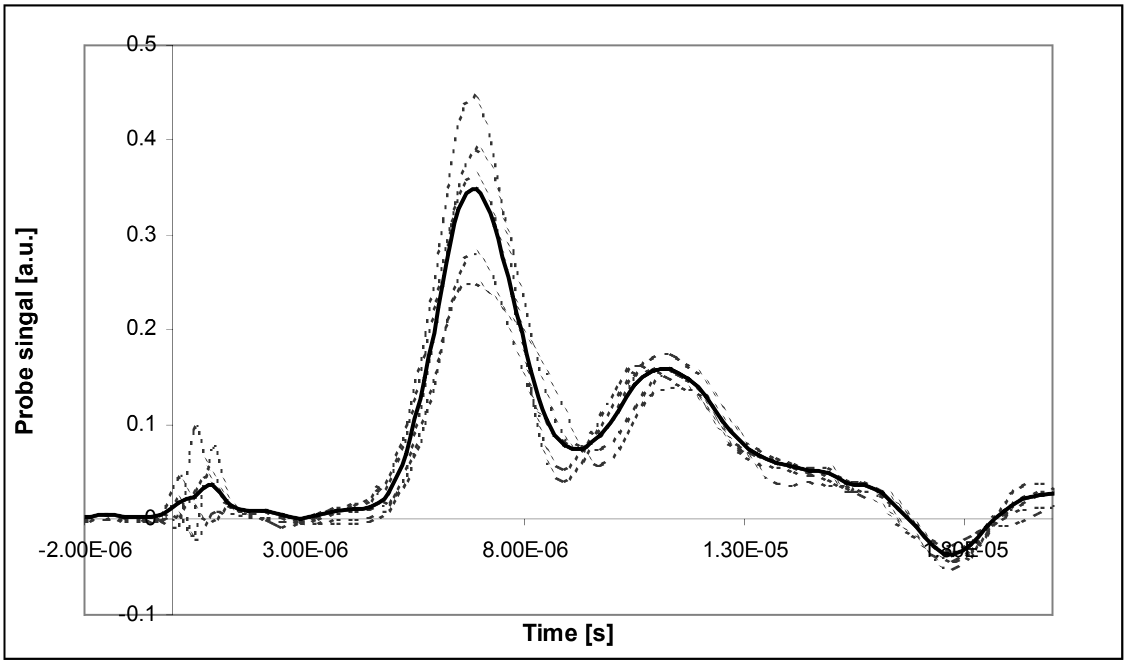

Fig. 8.23 : Shot-to-shot variations (dotted lines) and the resulting average (solid line) for Teflon at 10.16 cm distance and 30 J discharge energy

8.3.3.1 Noise Investigation

Pressure probe measurements can be complicated by three kinds of extraneous signals: noise generated by stress waves introduced into the probe structure, electromagnetic noise, and mechanical noise. As discussed above, the buffer on the probe reduced the impact of stress waves in the probe to an insignificant level. The electromagnetic noise originates from sources like the spark plug (frequencies in the gigahertz range) and the main PPT discharge (frequencies in the megahertz range). The mechanical noise is due to impact of parts of the plume on the pressure probe support. Since the probe is mounted rigidly on the probe support, any impact on the probe support would show up as a negative pressure in the probe signal (the probe acts like an accelerometer in this case). It was important to investigate the magnitude of the noise introduced by these two sources and how they are superimposed on the main impact pressure signal. Two simple experiments were conducted to investigate the total noise (the sum of electromagnetic and mechanical noise) and the electromagnetic noise. To measure the total noise, the probe head was covered by a cap which was closed on one side, such that the sensing head was not exposed to the incoming plume. The signal measured with such a configuration should be only due to electromagnetic noise and plasma impacting on the probe support. The electromagnetic noise was measured by additionally placing a plastic sheet in front of the thruster such that the expelled plasma is deflected and cannot reach either the probe or the probe support. A signal measured with such a configuration should be only due to electromagnetic noise. Fig. 8.26 illustrates schematically the two different setups. Fig. 8.27 shows a comparison between the pressure probe signal and the two kinds of noises. The measurement shown in Fig. 8.27 was obtained for a configuration, which was assumed to generate a high level of noise, precisely for Teflon at 30 J discharge energy and at 10.16 cm distance from the thruster on the thruster's axis. It is evident that in general neither electromagnetic noise nor mechanical noise contributes in a significant way to the pressure signal. The only exception here is the time of discharge initiation. It is clear that the pick up seen in the first 1 μs is due to electromagnetic noise. A noise investigation was in general performed at locations where the noise was assumed to increase (e.g. a higher exposure of the probe support to the plume or at locations closer to the thruster). However, in none of the cases the noise was found to be significant.

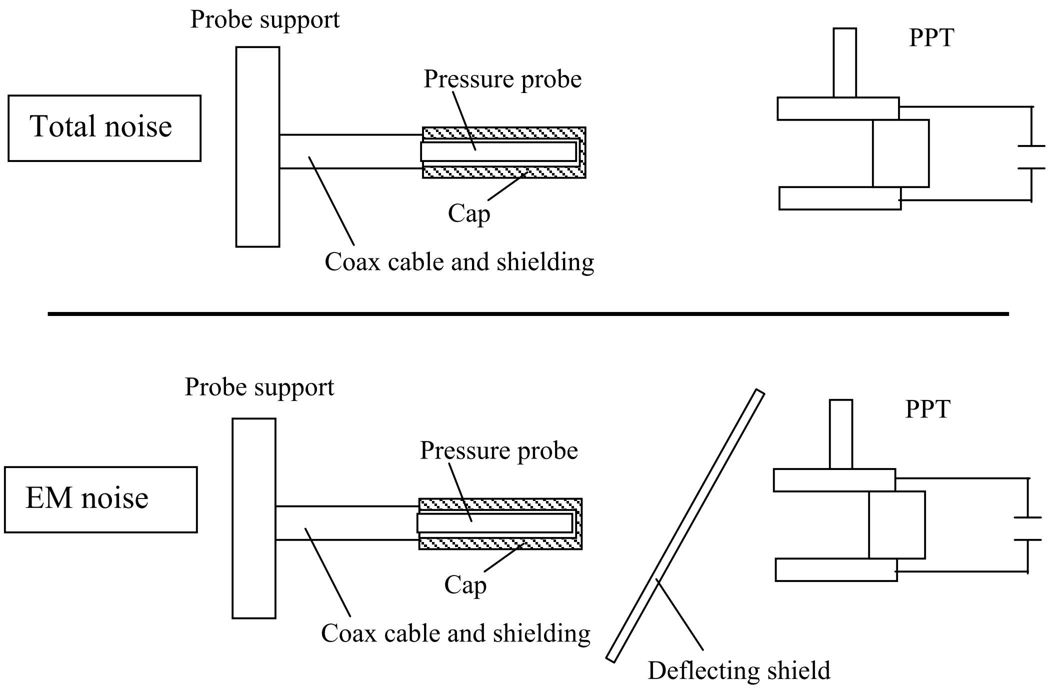

Fig. 8.24: Experimental set up for evaluation of noise in the pressure probe measurements

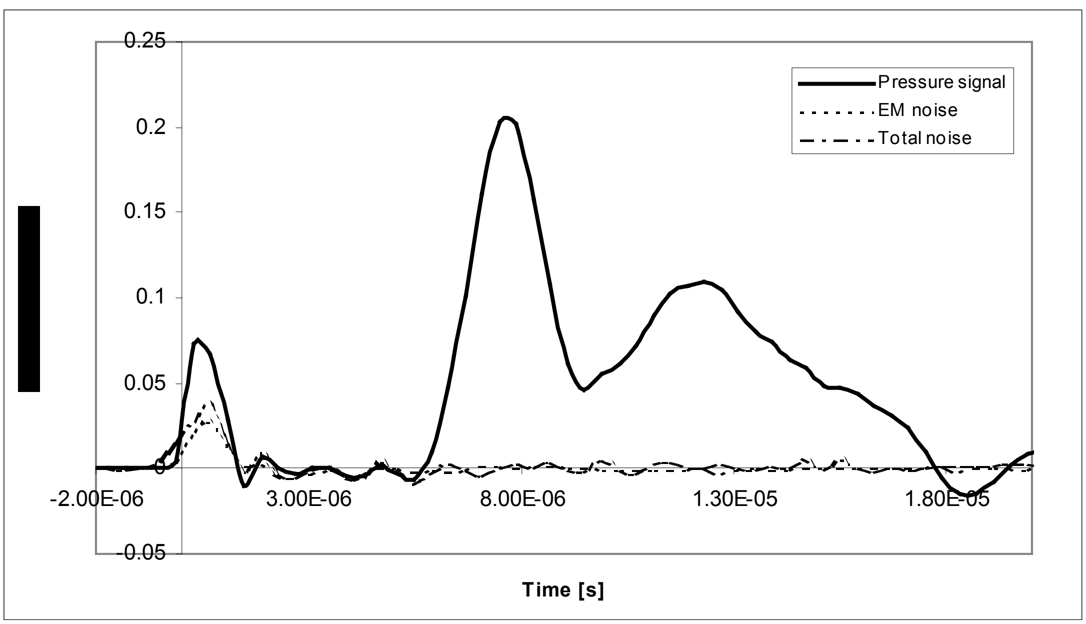

Fig. 8.25: Evaluation of the influence of noise on the pressure probe signal (Teflon, 30 J, 10.16 cm)

8.3.3.2 Pressure Probe Calibration

The ejected plasma plume of a PPT consists of an unsteady, high velocity, rarefied plasma with a time varying mass flux of highly inhomogeneous mass and velocity distributions. The calibration of the pressure probe is complicated by the lack of a facility able to reproduce in a controlled fashion conditions similar to those existing in the plume of a PPT. A two-step procedure was therefore used for the calibration of the probe. In the first step, the probe response was compared to the well-known conditions behind a reflected shock in a shock tube. In the second step, which will be discussed in Chapter 9.2, the measurements in the plume were compared to impulse bit measurements conducted at the thrust stand at NASA Glenn Research Center. While the first step is providing the general probe response to an incoming mass flux, the second allows a correlation of the probe's output in transient plasma flow conditions identical to the one existing in the plume of a PPT. An additional correction factor (see Chapter 9) accounts for stagnation pressure losses due to thermal effects and losses in the shock and viscous interaction at the sensing location.

A shock tube with a 0.9 m long driver section and a 0.9 m long driven section was utilized to calibrate the pressure probe's output. The pressure probe was rigidly mounted at the far end of the driven section such that the buffer is flush with the end wall of the driven section. A thin aluminum foil separated the two sections. The driver gas (Nitrogen) was stored in a commercial high pressure gas cylinder. A pressure reduction valve connected the high pressure gas cylinder with the driver section and reduced the pressure to 2 bar. Upon opening the valve, the driver gas was allowed to fill the driver section and eventually break the aluminum foil separating the driver and driven section (burst mode). As a result, a shock wave propagates into the driven section, towards the pressure probe. Upon arriving at the end wall of the driven section, the shock is reflected. The conditions behind the reflected shock are well known and provide therefore means to calibrate the probe by comparing the probes output signal with the analytic results[57]. A calibration constant, c, of 1.7 x 10^{-4} V/(N/m^2) was obtained in this fashion.

8.3.4 Experimental Results and Reduction of Data

8.3.4.1 Impact Pressure Measurements

Impact pressure measurements were conducted at several different locations downstream of the thruster's exit plane: 5.05 cm, 10.16 cm, and 15.24 cm. Figs. 8.29 and 8.30 compare the impact pressures measured in the case of the Teflon thruster with those of the water thruster. The measured peak impact pressure in the water case is nearly a factor of 4, for the 30 and 20 J case, and in the 10 J case a factor of 2 smaller than the one in the Teflon case. Additionally, the characteristic second peak is for water much weaker or not existent at all. This is attributed to the over-damped discharge current waveform in the water case as discussed in Chapter 6.

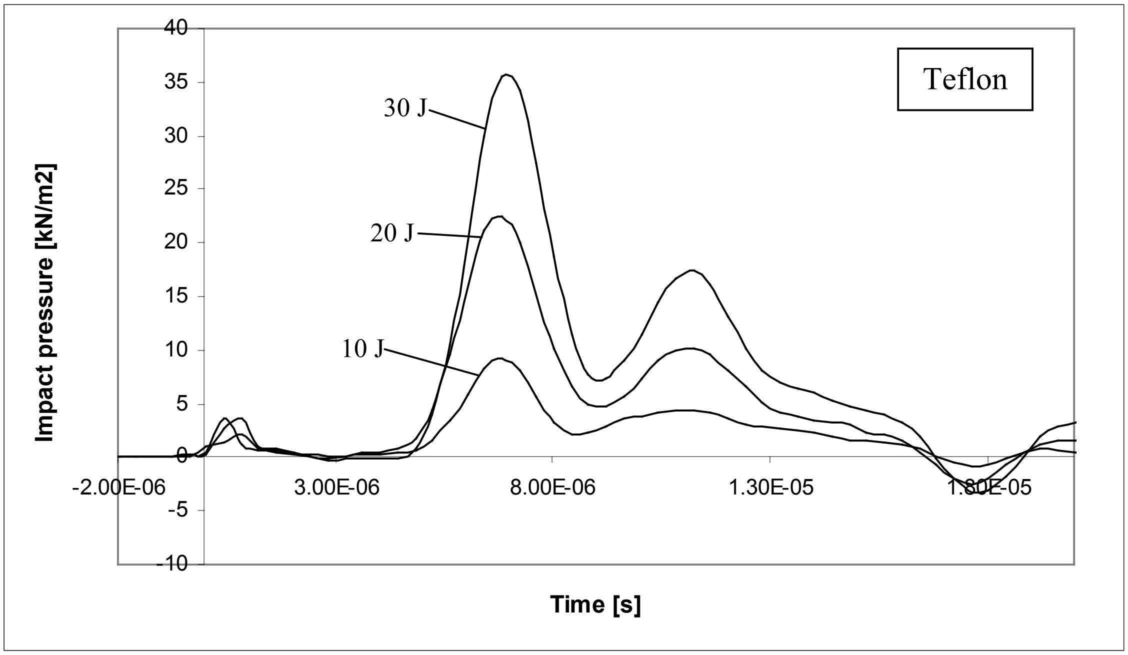

Fig. 8.26: Impact pressure for the Teflon thruster as a function of the discharge energy (on the centerline at 5.08 cm distance)

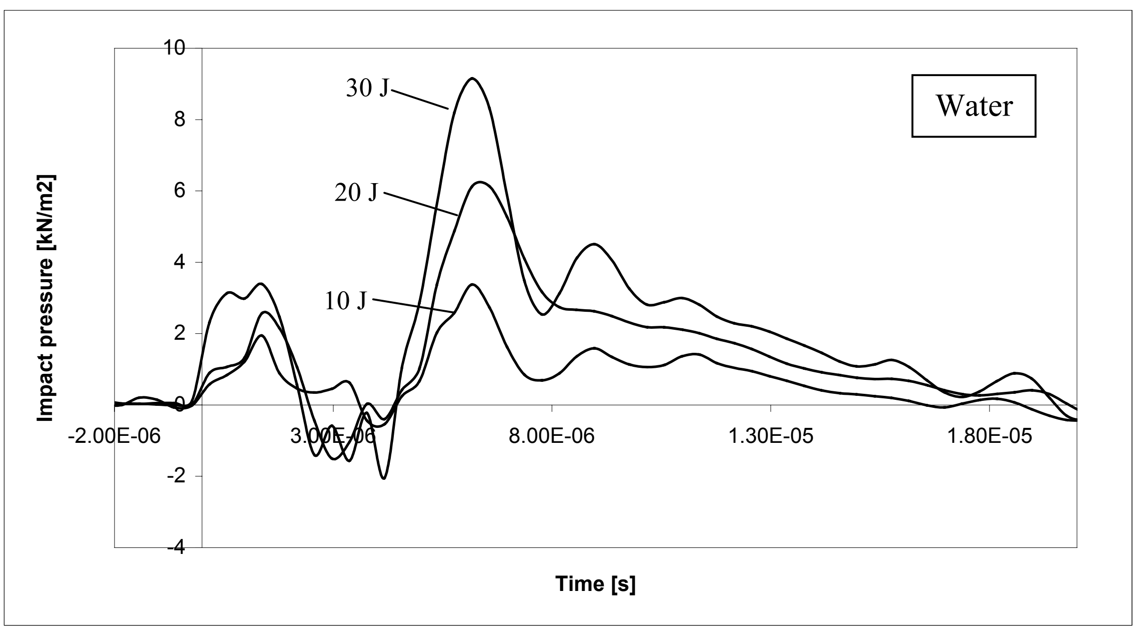

Fig. 8.27: Impact pressure for the water thruster as a function of the discharge energy (on the centerline at 5.08 cm distance)

8.3.4.2 Time-of-Flight Measurements

Similar to Langmuir probe, pressure probes can be employed for TOF evaluations. The fundamental difference between those measurements is that pressure probes register mass flux in general and are not limited to charged particles, as it is the case with Langmuir probes. Consequently, pressure probe measurements in the thruster's plume provide additional information about the composition of the plume and the discharge and acceleration processes in Pulsed Plasma Thrusters.

Measurements were conducted at three different downstream locations: 5.08 cm, 10.16 cm, and 15.24 cm. As before, all the results shown in the following are averaged values over 5 – 8 successive measurements in order to cope with the shot-to-shot variations. Fig. 8.31 depicts the results for the Teflon thruster at the three different locations. Fig. 8.32 shows the same for the water case, with the exception of the 15.24 cm case. At this location the signal was below the noise level and allowed no conclusive statements with regard to time of onset, etc. The respective discharge currents are included in both figures to allow a comparison between the time histories of the discharge itself and the registered mass flux.

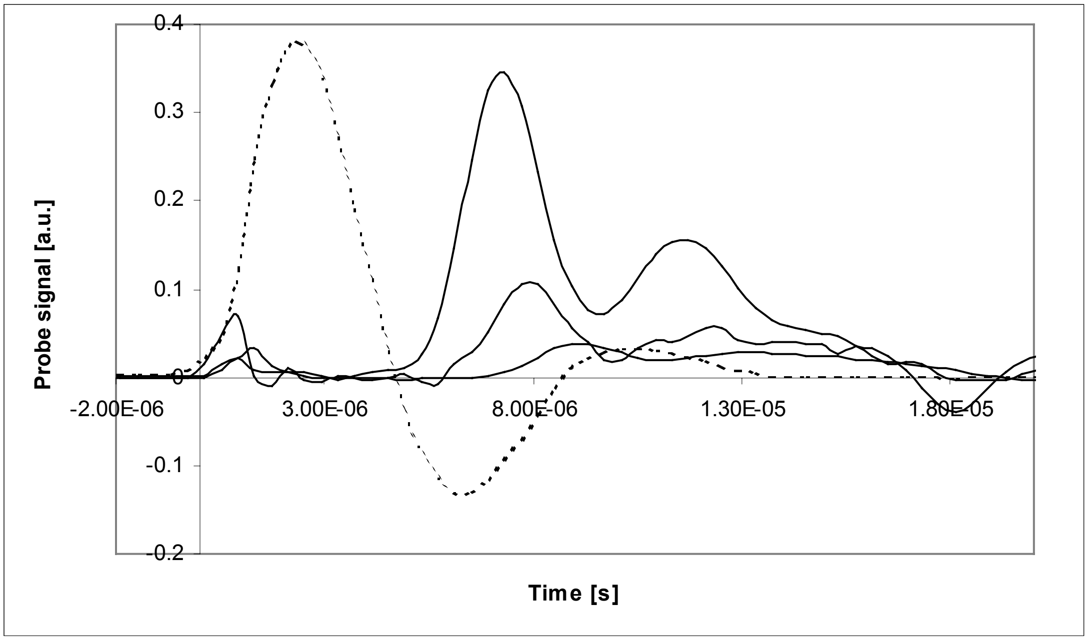

Fig. 8.28: Pressure probe signal for different distances (20 J, Teflon) (solid lines) with the discharge current (dotted line) for comparison

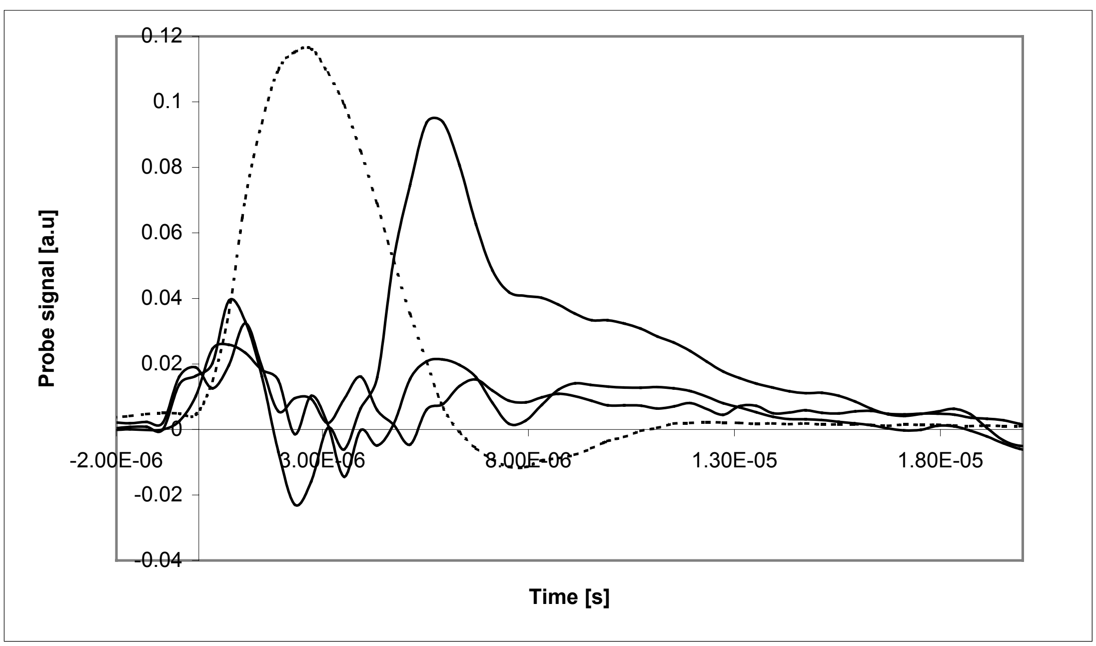

Fig. 8.29: Pressure probe signal for different distances (20 J, water) (solid lines) with the discharge current (dotted line) for comparison

Several general features are clearly recognizable in both figures: (i) the onset of registered mass flux occurs later with increasing distance to the thruster, (ii) the signal magnitude decreases with increasing distance to the thruster, attributed mainly to the expansion of the plume, and (iii) the total signal length increases slightly with increasing distance to the thruster. Comparing the measurements for Teflon with those for water, it is obvious that the signal for the Teflon thruster is about a factor 3 higher and arrives later than the respective signals for the water thruster.

As mentioned above, the plasma plume consists of a variety of particles with a range of particle masses and velocities. However, similar to the Langmuir probe measurements, the mass flux signal shows distinctive features, like the onset of the signal and various peaks, which can be utilized to evaluate an averaged value for the particle velocities. For this purpose it is useful to nondimensionalize each signal with its respective peak value as shown in Fig. 8.33.

Table 8.3 summarizes the result of this analysis. Since the signal strength for the water case at a 20 J discharge energy was relative low, Table 8.3 includes also the 30 J case. The main error in evaluating plume velocities in this manner is introduced by the general shot-to-shot variations with regard to the time of occurrence of the onset, or a peak of about ± 0.2 μs. When evaluating the velocity by comparing the time of occurrence at two locations, this translates to an error in time difference Δt of ±0.4 μs. Analysis of the data showed that any velocity variations in the plume are smaller than the error bars. Additionally, for Teflon it was not possible to observe velocity changes when changing the discharge energy. However, comparing the bulk plume velocities for Teflon and water, the trends indicate higher plume velocities for water.

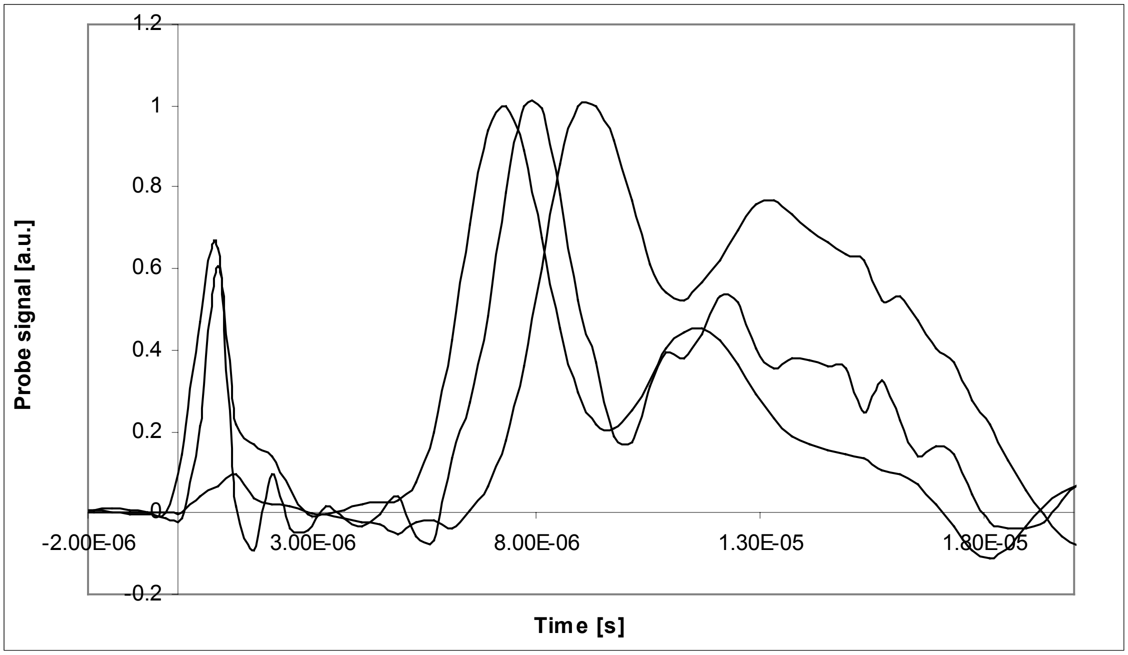

Fig. 8.30: Pressure probe signal for different distances (20 J, Teflon) nondimensionalized by their respective peak values

	Discharge energy [J]	Δs [cm]	Δt [μs]		V [km/s]	
			Teflon	**Water**	Teflon	**Water**
Onset	20	5.08 – 15.24	2.0	**1.6**	50.8 $\pm^{25\%}_{20\%}$	**63.5** $\pm^{33\%}_{20\%}$
	30	5.08 – 15.24	2.0	**0.8**	50.8 $\pm^{25\%}_{20\%}$	**127** $\pm^{100\%}_{33\%}$
1st peak	20	5.08 – 15.24	2.0	**0.0**	50.8 $\pm^{25\%}_{20\%}$	**N/A**
	30	5.08 – 15.24	2.0	**0.0**	50.8 $\pm^{25\%}_{20\%}$	**N/A**
2nd peak	20	5.08 – 15.24	1.6	**N/A**	63.5 $\pm^{33\%}_{20\%}$	**N/A**
	30	5.08 – 15.24	2.0	**N/A**	50.8 $\pm^{25\%}_{20\%}$	**N/A**

Table 8.3: Particle velocities in the plasma plume based on the pressure probe measurements

CHAPTER 9

ANALYSIS OF EXPERIMENTAL RESULTS AND COMPARISON WITH ACCELERATION MODELS

9.1 Analysis of Conductivity and Electron Temperature

Utilizing the current and voltage characteristic, the electron temperature and plasma conductivity can be estimated. The total voltage drop V_{total} across the gap between the electrodes is given by the one-dimensional approximation of Ohm's law

$$V_{total} = V_{fall} + \int \left(\frac{j}{\sigma} + uxB + \frac{\Omega}{\sigma|B|} \cdot (jxB) \right) dl \tag{9.1}$$

with the current density j, the plasma conductivity σ, the electrode fall voltage V_{fall}, and the Hall parameter Ω. The current density and the magnetic field in the discharge channel are in a first approximation constant and are given by

$$j = \frac{I}{w \cdot l} \ , \ B = \frac{\mu_0 \cdot I}{2\pi \cdot l} \tag{9.2}$$

with the width, w, and length, l, of the discharge channel.

Equation 9.1 can be simplified by neglecting ion slip and the Hall effect (j x B). Integrating Eq. 9.1 over time, the conductivity can be expressed as

$$\sigma = \left(V_{total} - V_{fall} - \frac{u_z \mu_o I}{2\pi} \right)^{-1} \cdot \frac{I}{w} \tag{9.3}$$

with the width, w, and length, l, of the electrodes, and the axial velocity u_z. The fall voltage under conditions as in a PPT can be approximated to be 30 V. The velocity u_z can be obtained in two fashions depending on the assumption of what part of the plasma inside the discharge channel carries the current: (i) assuming that the initial front carries the main current, u_z can be evaluated based on the Langmuir probe measurements, (ii) assuming that a slower portion behind the initial front carries the current, the velocity can be approximated as sonic velocity. For the first, the distance between the locations of the discharge initiation and Langmuir probe (5.08 cm +2.54 cm (length of the discharge channel)), divided by the time delay between discharge initiation and onset of the probe signal allows one to approximate the velocity of the initial front. The sonic velocity is given by

$$a = \sqrt{\gamma \cdot R \cdot T} \tag{9.4}$$

with the ratio of specific heats, γ, the specific gas constant, R, and the temperature, T. In the following, γ was assumed to equal 5/3 for water and Teflon. The specific gas constant is given by R = $\Re$/M, with the universal gas constant $\Re$ = 8314 J/kg-mol-K. The molecular weight of Teflon was based on observed averaged molecular weight[31], while it was assumed that water was fully dissociated. Temperature measurements in the discharge channel itself are not available. It was therefore chosen to use results obtained by the Langmuir probe measurements at 5 cm downstream of the thruster's exit plane: $T_{e,Teflon}$ = 8.7 eV and $T_{e,\ H2O}$ = 3.0 eV. Table 9.1 summarizes the velocities obtained with these two methods:

	Current sheet velocity	
	Langmuir probe TOF	Sonic velocity assumption
Water	58.6 km/s	9.0 km/s
Teflon	38.1 km/s	6.7 km/s

Table 9.1: Evaluation of the current sheet velocity based on sonic velocity assumption and on experimentally evaluated exhaust velocities

The conductivities for the Teflon and the water case for both assumptions were evaluated with Eq. 9.3 and are summarized in Table 9.2. Both assumptions result in a significantly smaller conductivity for water in agreement with the experimental observations.

	Conductivity	
	Langmuir probe TOF	Sonic velocity assumption
Water	1610 1/Ωm	1150 1/Ωm
Teflon	5050 1/Ωm	2670 1/Ωm

Table 9.2: Evaluation of the conductivity based on sonic velocity assumption and on experimentally evaluated exhaust velocities

In general, the conductivity parameter describes the ability of a given plasma to carry a net current into the direction of the electric field against random thermal motion and collision. A smaller value for the conductivity means therefore that either not enough charge carriers are available in the case of water or that yet unknown effects prevent currents of the same magnitude as observed in the case of Teflon.

The electron temperature inside the discharge channel can be approximated by utilizing those conductivity values and the Spitzer's model[58] for the relation between conductivity and electron temperature given as

$$\sigma = \frac{\gamma_E \cdot T_e^{3/2}}{38 \cdot Z \cdot \ln \Lambda} \qquad (9.5)$$

with the electron temperature in °K (1eV =11600 °K), the ionic charge Z, a correction factor[58], γ_E (to include electron-electron encounters), and $\ln(\Lambda) = 10$. Table 9.3 summarizes the result for the assumption of an ionic charge of 1 and $\gamma_E = 0.582$. Assuming Z = 2 would increase the obtained temperatures by a factor of roughly 1.4.

The general trend in electron temperature obtained by this method is the same as found in the Langmuir probe measurements, namely, higher temperatures for the Teflon case. The reason for the discrepancy between the experimental evaluated values and the ones calculated above is attributed to mainly two reasons. First, the Spitzer model assumes a Lorentz gas condition, and second, the electron temperature as calculated above is associated with the plasma still in the acceleration channel, while the measurements with the Langmuir probe were conducted downstream of the thruster's exit plane.

	Electron Temperature	
	Langmuir probe TOF	Sonic velocity assumption
H_2O	0.89 eV	0.7 eV
Teflon	1.9 eV	1.2 eV

Table 9.3: Comparison between electron temperature based on the current sheet velocity assumptions

9.2 Analysis of the Magnetic Field Measurements

Based on the magnetic fields $B_y(z,t)$ from Chapter 8.2, the time resolved enclosed currents for locations downstream of the thruster's exit plane were evaluated with the following equation:

$$I_{enclosed}(z,t) = \frac{2 \cdot \pi \cdot z \cdot B_y(z,t)}{\mu_o} \tag{9.6}$$

Figs. 9.1 and 9.2 compare the enclosed current in the Teflon case with the water case for 1.5 cm and 5. 08 cm distance from the thruster's exit plane. The discharge current was included in both figures for time reference.

A comparison of the enclosed currents for Teflon and water shows a much higher percentage of the discharge current extends downstream in the water case than it is seen for the case of Teflon. Comparing the time history of the enclosed currents with the respective discharge currents offers an explanation for this observation: The magnitude of the enclosed current at a certain time is related to the magnitude of the discharge current. The results of all the diagnostic methods described above indicate higher current sheet velocities in the water case. Ergo, the current sheet in the water case arrives earlier at a downstream location when the discharge currents are still relative high.

A better indication of the arrival time of the current sheet is obtained by taking the time derivative of the magnetic field. According to Faraday's law

$$-\frac{d\vec{B}}{dt} = \nabla x \vec{E}$$

which can be simplified for a one-dimensional case to

$$-\frac{dB}{dt} \propto \frac{j}{\sigma}$$

Figs. 9.3 and 9.4 show the time derivative of the magnetic fields (Chapter 8.2.4.1) for water and Teflon, respectively. A comparison shows two distinct differences between the water and Teflon case: (i) the earlier onset of the current density in the water case indicates a higher current sheet velocity, and (ii) the front of the water exhaust plume is confined in a smaller volume than it is the case for Teflon. These results are in accordance with results obtained from the Langmuir probe and pressure probe.

Comparing Figs. 9.3 and 9.4, it is also evident that for water, compared to the Teflon case, relative larger currents flow through the current sheet even after leaving the volume between the electrodes. This indicates that while for Teflon the acceleration process is close to being terminated after the main component of the plasma exited the thruster, the water plasma is still further accelerated. However, this acceleration process cannot be efficient due to a curvature of the current and the subsequent increase of an off-axis component of the plasma velocity.

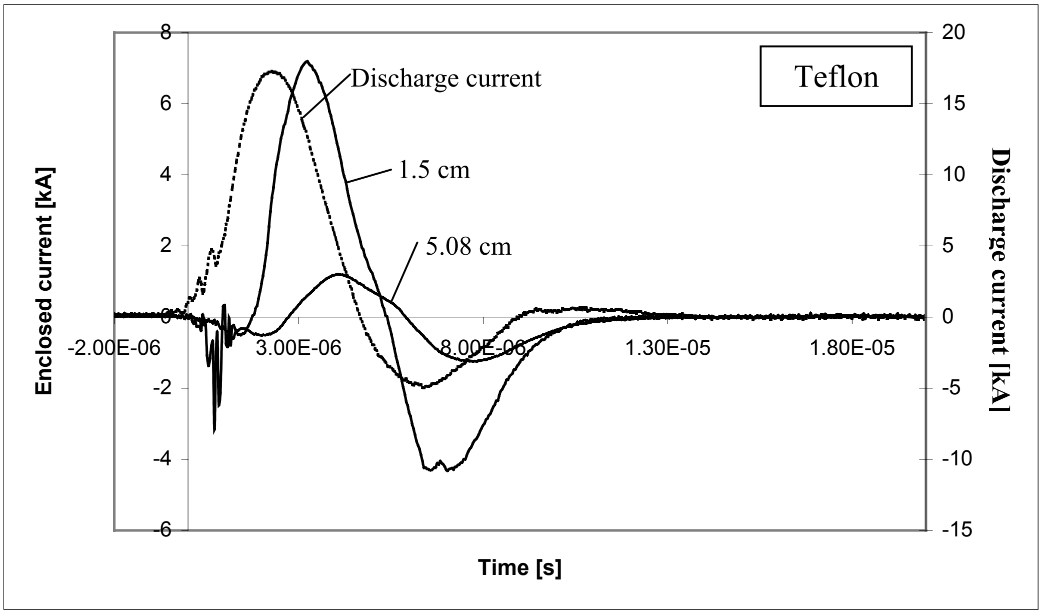

Fig. 9.1: Enclosed currents for Teflon, 20 J, at 1.5 cm and 5.08 cm, along with the discharge current (gray line)

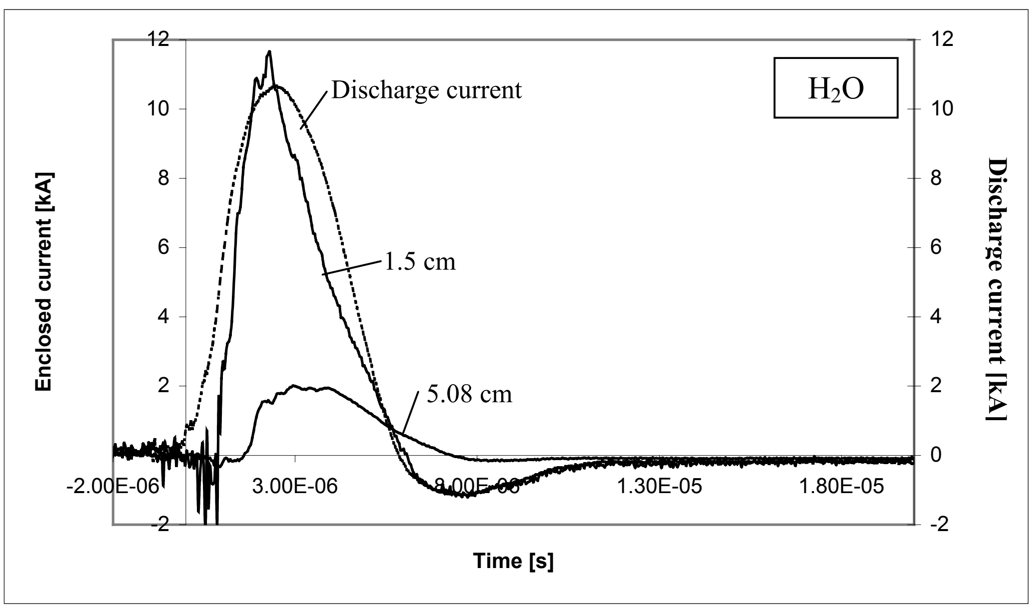

Fig. 9.2: Enclosed currents for water, 20 J, at 1.5 cm and 5.08 cm, along with the discharge current (gray line)

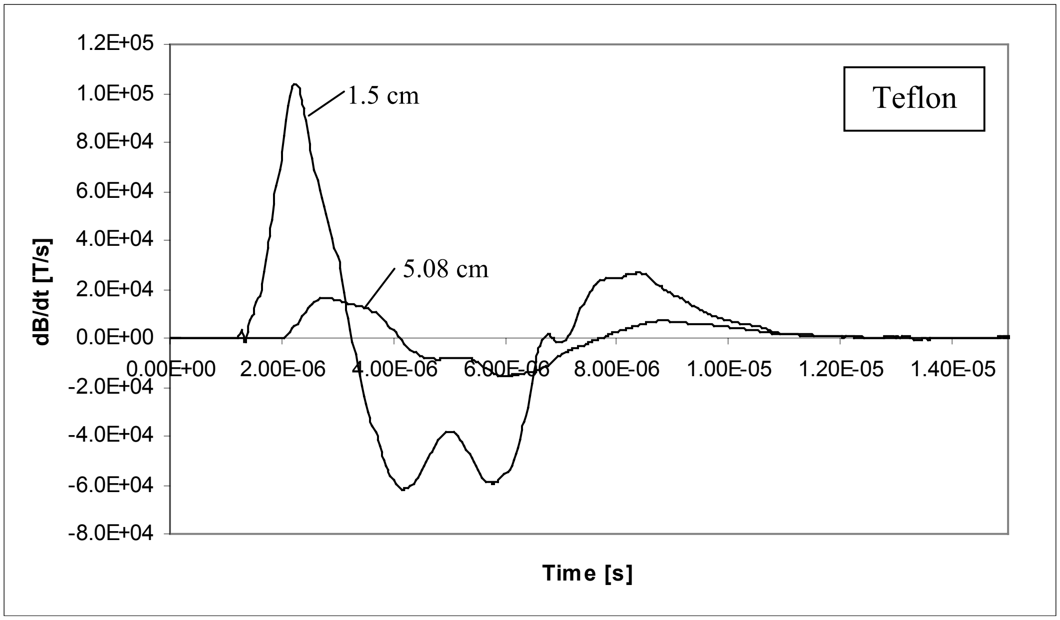

Fig. 9.3: Time derivative of the magnetic field for the Teflon case at two downstream locations

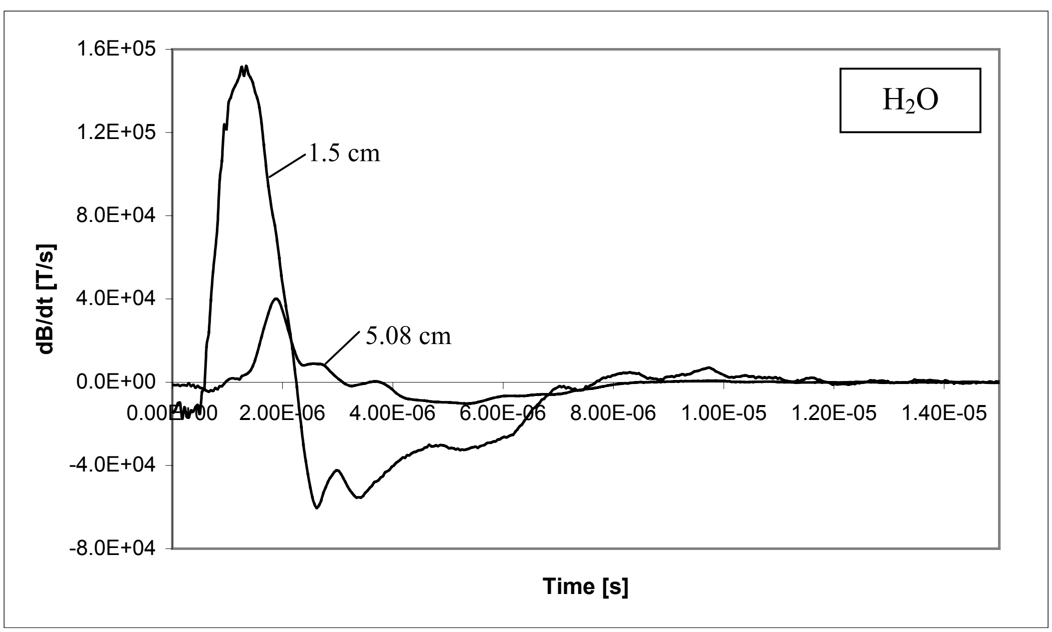

Fig. 9.4: Time derivative of the magnetic field for the water case at two downstream locations

9.3 Analysis of the Plume Structure

Further insight into the general acceleration processes can be gained by comparing the time histories of the measurements in the plume, specifically with the Langmuir probe, the magnetic field probe, and the pressure probe. Such a comparison is presented in Figs. 9.5 and 9.6 for Teflon and water, respectively. Both of these figures depict measurements conducted at 5.08 cm downstream of the thruster's exit plane and for a discharge energy of 20 J. The respective discharge currents were included for time references. Fig. 9.5 compares the time histories for the different diagnostic methods for the case of the Teflon thruster. The magnetic field probe picks up a signal around 2μs after discharge initiation. The delay is a clear indication of the electromagnetic nature of the thruster since it indicates the existence of a relative dense and ionized plasma.

The pressure probe signal shown is adjusted for the stress signal delay through the buffer on the front face of the pressure probe. The duration of this delay was approximated to be 2 μs, based on an estimated stress wave velocity of 1000 m/s through the 2 mm thick buffer. The corrected time history is depicted in Fig. 9.5 (d) and Fig 9.6 (d) (dotted lines).

In Fig. 9.5 for Teflon, the Langmuir probe and the pressure probe measurement show clearly two peaks, indicating two waves of plasma exiting the thruster. The decline in signal strength between the first and second peak of the Langmuir signal is larger than the one of the pressure signal, indicating a lower degree of ionization in the second wave.

It is interesting to note that the second peak connects with a reversal of current direction in the PPT discharge.

The Langmuir probe and the magnetic field probe suggest a more confined plasma front in the case of water. The Langmuir probe signal for water rises faster and does not exhibit the second peak as in the case of Teflon. Interestingly, the magnetic field measurements do not show a reversal of the magnetic field as was seen with Teflon. Both observations are due to the characteristic history of the discharge current in case of water, which does exhibit only a slight current reversal. Comparison of the time histories of all the measurements clearly show in the case of water an earlier onset in accordance with the higher exhaust velocities evaluated earlier (Chapter 8.1.4.2 and 8.3.4.2).

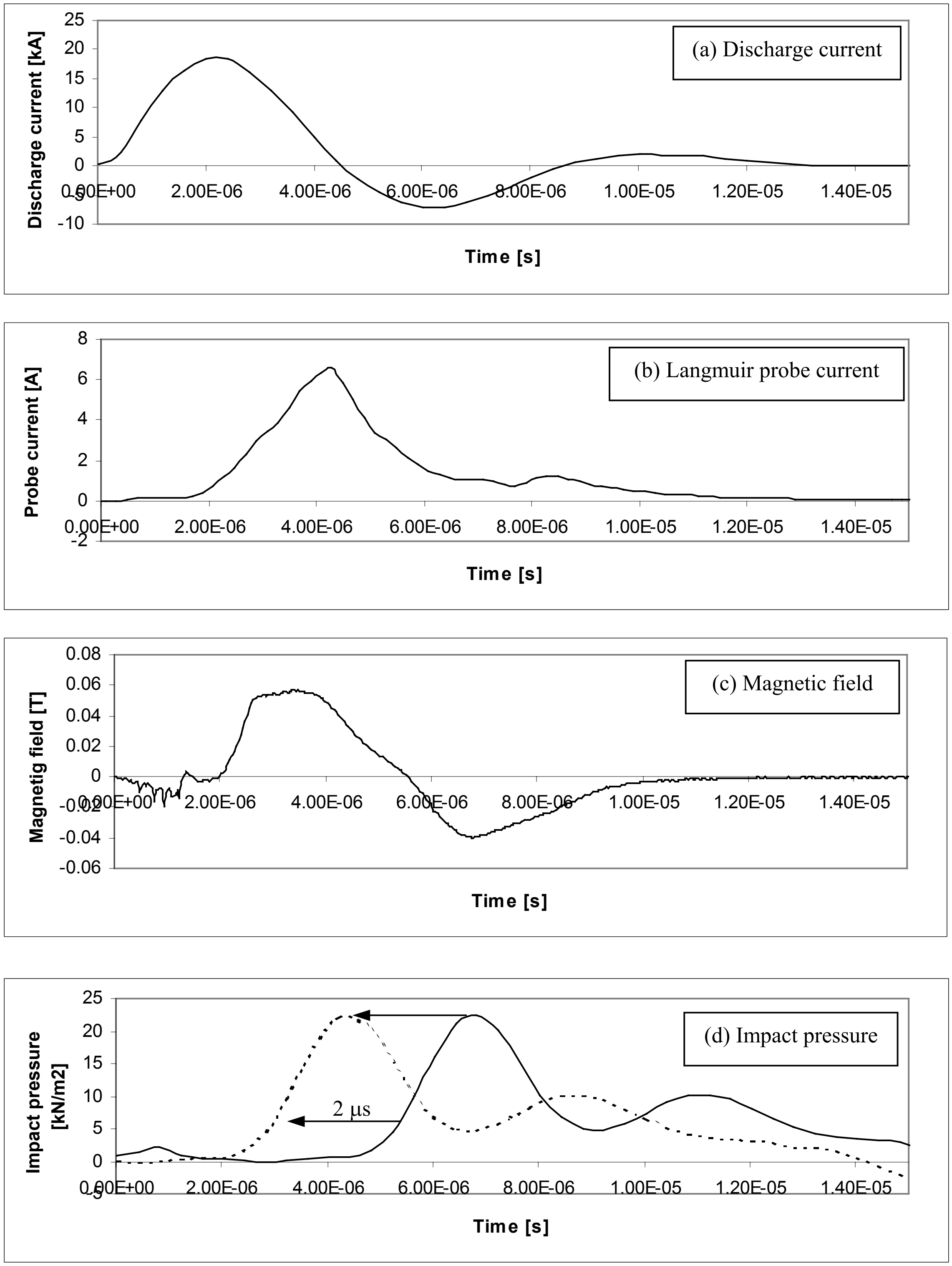

Fig. 9.5: Comparison of the time history of the Langmuir probe, magnetic field probe, and pressure probe measurements for Teflon at 5.08 cm downstream of the thruster's exit plane along with the discharge current for time reference

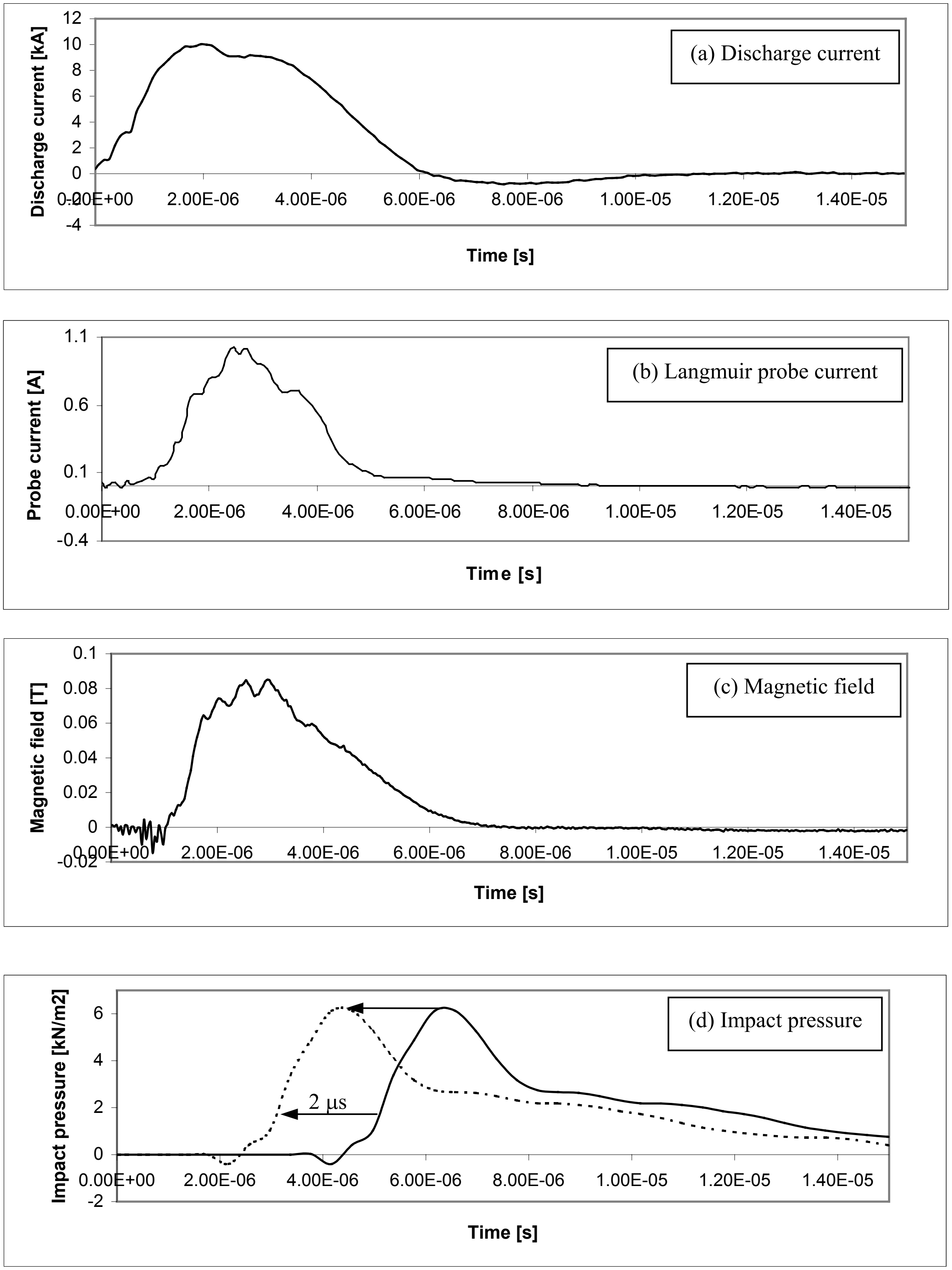

Fig. 9.6: Comparison of the time history of the Langmuir probe, magnetic field probe, and pressure probe measurements for water at 5.08 cm downstream of the thruster's exit plane along with the discharge current for time reference

9.4 Impulse Bit Evaluation from Thrust Stand Measurements

For purposes of establishing an absolute reference for system performance in the context of accepted procedures in the research community, the PPT thruster configuration for Teflon propellant was transported to the NASA Glenn Research Center, Cleveland, OH, and installed in their space thruster test facility for the purpose of making thrust stand measurements. Such data would allow absolute identification of integrated system performance and subsequent comparison with detailed local diagnostics.

Impulse bit measurements at the NASA Glenn Research Center were performed on a torsional-type thrust stand[59]; the thruster and thrust stand were located in a 1.5 m diameter by 4.5 m long oil diffusion pumped vacuum facility (VF-3) with a typical facility base pressure of 2×10^{-6} Torr. The thruster configuration is identical to the one used in tests at The Ohio State University.

For the single impulse bit measurements, the reported values represent an average of ten pulses. The steady-state thrust was measured while the thruster was operating continuously for approximately five minutes at a frequency of 1.17 Hz. Single impulse bit and steady-state thrust measurements were performed for the PPT at energy levels of 10, 20, and 30 Joules. The results of these tests are summarized in Table 9.4.

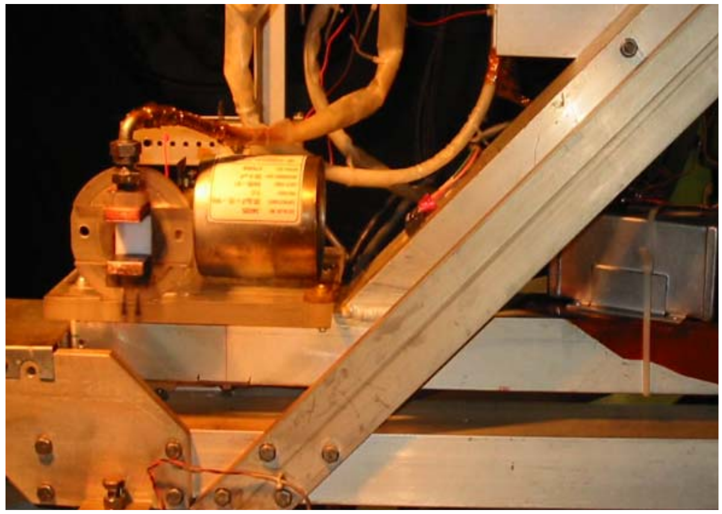

Fig. 9.7: Teflon PPT installed on the thrust stand

Discharge Energy [J]	Impulse bit [μN-s]
10	122
20	273
30	440

Table 9.4: Results of the impulse bit measurement of the Teflon thruster on the thrust stand at NASA Glenn Research Center

9.5 Impulse Bit Evaluation Based on Impact Pressure Measurements

The calibration process described in Chapter 8.3 relates the probe response to a cold gas pressure environment. This is fundamentally different from the situation in the plume of a PPT. Evaluation of the pressure in the plasma exhaust using only a cold gas calibration would not account for several effects. Further steps are necessary for a more accurate correlation between the probe signal and the pressure in the plasma exhaust.

The impulse bit I_{bit} of a PPT is related to the probe response (impact pressure p_{impact}) in the following fashion:

$$I_{bit} = C\iint\left(\frac{1}{c}\,p_{impact}\right)dt\,dA_{cs} \tag{9.7}$$

with the cross section A_{cs} of the plasma plume and a correction factor C. The correction factor C is necessary to accommodate several factors, of which many cannot be evaluated in a straightforward fashion. C includes the effects of thermal losses in the probe, losses due to a shock in front of the probe, and simply the fact that the plume is highly inhomogeneous[60,61]. An accurate analytical evaluation of the impact of all these losses, and therefore the evaluation of the exact value of C would be beyond the scope of the present work. However, a global correction factor incorporating all the above mentioned effects can be determined.

The impulse bits for several energy levels of the Teflon thruster are known from measurements conducted on the thrust stand of the NASA Glenn Research Center (Table 9.4). To correlate these values with the pressure probe results of Teflon, it is necessary to evaluate the pressure in a cross section A_{cs} of the plasma plume. However, the main contribution of the mass flux is concentrated in a relative small area of the cross section. Further, following an integration of pressure signals over the cross section area, later was equated to an effective area, A_{eff}, and impact pressure on the center line (see Fig. 9.8).

Pressure measurements were conducted along a horizontal and vertical axis at a distance of 10.16 cm from the thruster's exit plane to evaluate A_{eff}. Starting from the thruster's axis and going outward in 1.5 cm intervals, the measurements were performed until the magnitude of the extraneous signal made further measurements impossible. The measurements were performed with the Teflon thruster and a discharge energy of 30 J. Figs. 9.9 and 9.10 depict measurements performed on the horizontal axis and vertical axis respectively.

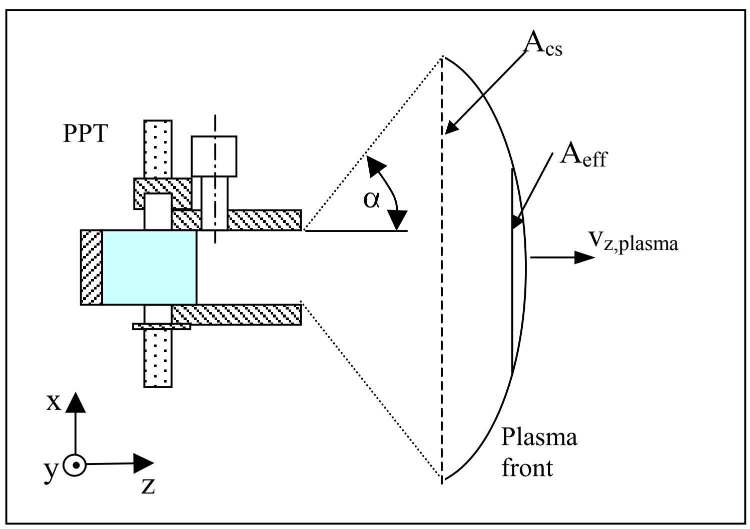

Fig. 9.8: Schematic of the expanding plasma front and the related areas

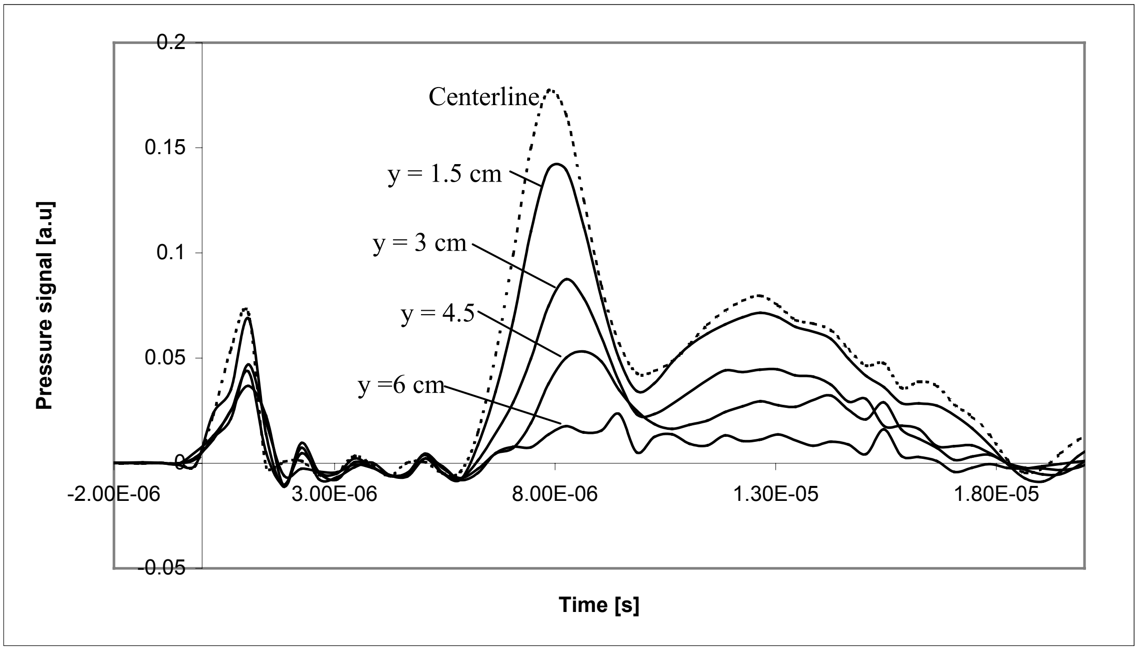

Fig. 9.9: Horizontal pressure distribution in the exhaust plume (Teflon, 30 J)

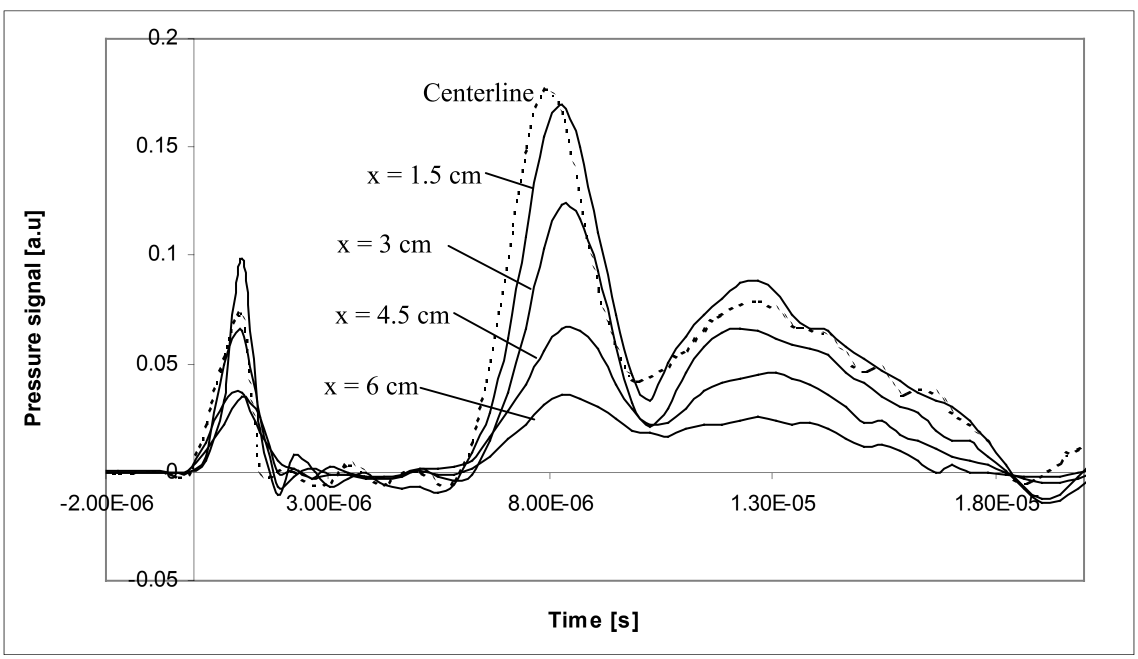

Fig. 9.10: Vertical pressure distribution in the exhaust plume (Teflon, 30 J)

It is evident from the rapid decrease in signal magnitude for increasing off-axis distances that the main flux is indeed concentrated in a relative well-defined area. In a first approximation, the effective area is defined to be equal to 8 x 10^{-3} m^2. The impulse bit, based on the pressure measurements on the centerline, $I_{bit,pp}$, can be evaluated with the following equation

$$I_{bit,pp} = A_{eff} \int \left(\frac{1}{1.7x10^{-4}} p_{centerline} \right) dt \tag{9.8}$$

The correction factor C is then equal to the ratio of the impulse bit as measured at the NASA GRC and $I_{bit,pp}$.

$$C = \frac{I_{bit,GRC}}{I_{bit,pp}} \tag{9.9}$$

This calculation was performed for the 10, 20, and 30 J case, and the obtained correlation numbers C are summarized in Table 9.5. The uniformity of the results for C over several discharge energies is evidence for the accuracy of the impulse bit evaluation with the pressure probe. This method can be regarded as accurate by including all effects, even though the impulse bits were obtained with impact pressure measurements at a single location in the exhaust plume.

A calibration factor of 1.51 x 10^{-5} V/(N/m^2) was evaluated (based on an average value of 11.2 for C and the probe calibration from Chapter 8.3.3.2) and will be used below as part of the evaluation of the performance of the thruster using water as propellant.

Discharge Energy [J]	Impulse bit NASA GRC [μN-s]	Impulse bit Pressure probe [μN-s]	Correction factor C
10	122	10.25	11.9
20	273	25.23	10.8
30	440	39.6	11.1

Table 9.5: Comparison between impulse bit values obtained at NASA GRC thrust stand and those derived from the pressure probe measurements, along with indicated calibration for each set of experimental data

9.6 Evaluation of the Mach Number

Knowledge of local sheet velocities and sonic velocities allow evaluation of the local Mach numbers as given in the following equation:

$$M = \frac{u}{a} = \frac{u}{\sqrt{\gamma \cdot R \cdot T}} \tag{9.10}$$

Assuming the sheet velocities, u, and sonic velocities, a, as given in Table 9.1, a Mach number of 5.6 and 6.5 for Teflon and water respectively was evaluated. The supersonic flow condition in the plume indicates a relative strong shock in front of the impact pressure probe and explains therefore partially the magnitude of the above discussed correction factor. Furthermore, since the Mach number for water is slightly higher than for Teflon (and therefore indicates higher losses), it is assumed that the correction factor for water should be higher than the values evaluated for Teflon and listed in Table 9.5. This would also indicate that the impact pressure evaluation based on the impact probe measurements underestimates the correct value in case of water.

9.7 Analysis of Acceleration Mechanism

The impulse bit of a PPT consists of an electromagnetic and a gas dynamic component. It can be analytically expressed in the following way:

$$I_{bit} = I_{bit,MHD} + I_{bit,GD} \tag{9.11}$$

$$I_{bit} = \frac{1}{2} \cdot L' \cdot \int I^2 dt + \left[\frac{8(\gamma - 1)}{\gamma^2 (\gamma - 1)} \cdot \Delta m E_o \right]^{0.5} \tag{9.12}$$

where L' is the inductance per length of the electrodes given by

$$L' = \mu_o \frac{h}{w} x \tag{9.13}$$

with the electrode gap h, electrode width w, and the displacement x of the current sheet from its initial position. Upon realizing that the initial energy E_o is given by

$$E_o = R \int I^2 dt \tag{9.14}$$

one can distinguish a thruster working predominately in the electromagnetic regime from one which is accelerating the plasma gas-dynamically simply by the fact that for the first, the impulse bit depends linearly on the energy E_o, while the second shows a square root dependency of E_o. The electromagnetic component of the thruster can be approximated by neglecting the second term on the RHS of Eq. 9.12 and utilizing the discharge current values for the Teflon thruster and the water thruster as depicted in Figs. 6.8 and 6.9. The result of this calculation is depicted in Fig. 9.11. The solid lines represent the result of $\int I^2 dt$, while the dotted lines represent the impulse bits obtained with the pressure probe (Chapter 6.4).

The results depicted in Fig. 9.11 allow several conclusions: (i) it is evident from the linear relationship between energy and impulse bit that both thrusters operate in a predominately electromagnetic mode, (ii) the good agreement (in terms of trends) between the impulse bit measurements obtained with the pressure probe and the discharge current measurements supports the validity of the pressure probe measurements, and (iii) the shape of the graphs supports the proportionality of $\int I^2 dt$ to I_{bit} as suggested by Eq. 9.12 (neglecting the thermal contribution). This is especially true for the Teflon case, but also in a first approximation for the water case. The proportionality constant is equal to the inductance per length and is evaluated to be L'_{Teflon} = 0.7 μH/m and L'_{H2O} = 0.88 μH/m (averaged values). The different slope and slight downwards shift of the graph representing the experimentally evaluated impulse bit for water with regard to the $\int I^2 dt$ graph might be attributed to the fact that the semiempirical Eq. 9.12 was developed for an ablative PPT. The mass bits in such a thruster are a function of the discharge current, while in the water thruster the mass bit is fixed.

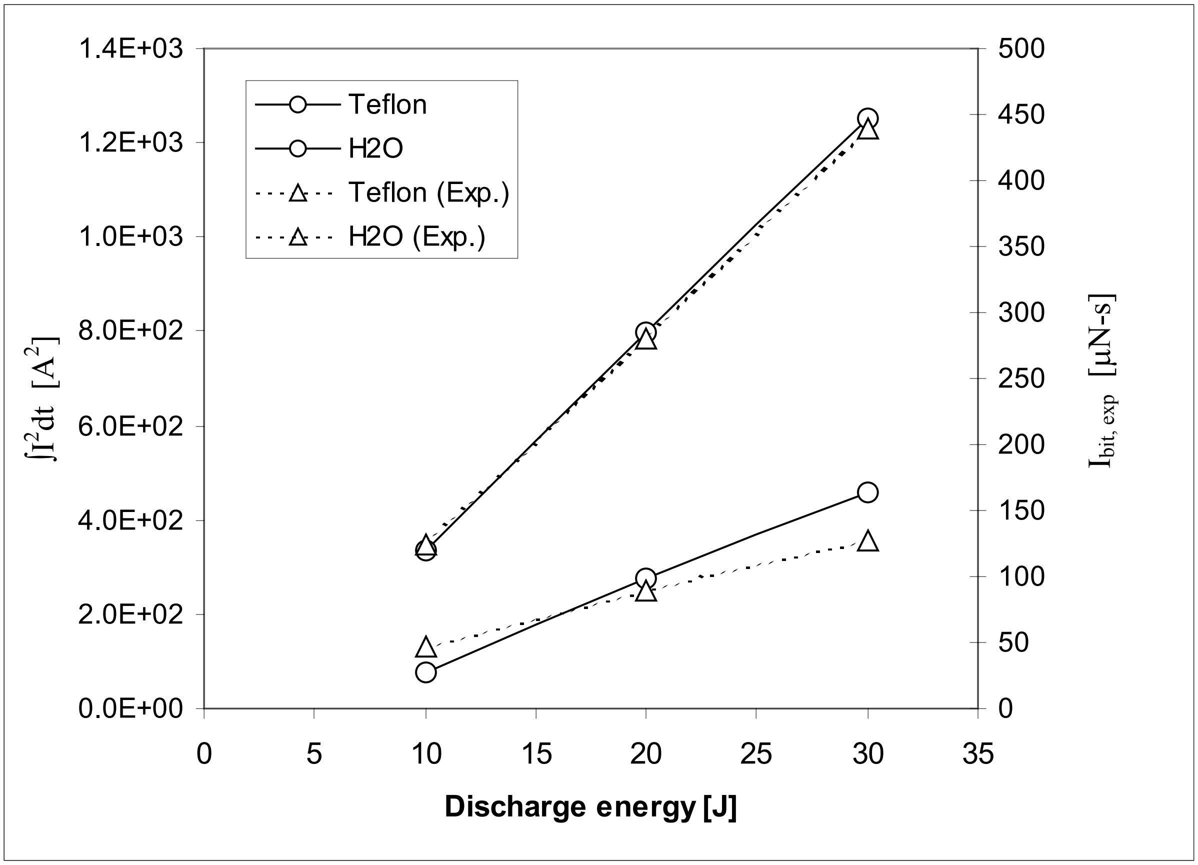

Fig. 9.11: Integration of the square of the discharge current (solid lines) in comparison to the values derived from the impact pressure measurements (dotted lines)

The significance of this result becomes clear when utilizing the voltage-current relation as given in eq. 6.1 to evaluate the power sinks as follows:

$$P = I \cdot V = I^2 \cdot R + \frac{d}{dt}\left(\frac{1}{2} L \cdot I^2\right) + \frac{1}{2} I^2 \cdot \dot{L}' \qquad (9.15)$$

The three terms on the RHS represent the rate of resistive heat generation, rate of energy stored in the magnetic fields, and the rate of work done on the moving plasma sheet. It is obvious that it is desirable to maximize the last term.

Since L_c and L_L (see Fig. 6.1) are constant, $\dot{L}'$ is given by

$$\dot{L}' = \mu_o \frac{h}{w} \dot{x} \tag{9.16}$$

Due to the fact that both thrusters employed the same electrode geometry (width, w, and gap, h), it can be concluded that the rate of change of inductance is higher in the water case, suggesting a better energy coupling into the plasma. However, the significant lower discharge currents in the water case reverse this effect again and the rate of work done on the moving plasma sheet is not maximized.

The conducted plasma diagnostic consistently indicated higher exhaust velocities. Integrating Eq. 9.15 over time allows an interesting comparison between the Teflon and water case. From 30 J, initially stored in the capacitor, nearly 17 J are dumped into resistive heating of the plasma in the Teflon case, as compared to 18 J in the water case. The major part of this energy can be considered as loss since it results in undirected thermal motion. However, since about the same energy is left in both cases and the mass bit participating in the discharge is for water in the 30 J case a factor of 21 smaller, a much higher amount of energy per unit mass is available. This results in the observed higher exhaust velocities.

9.8 Performance Evaluation and Comparison with the Analytic and Numerical Models

Thruster performance can be evaluated with the mass bit known from Chapter 7 and the above presented impulse bit values based on the impact pressure measurements. The following standard equations are utilized to calculate the specific impulse I_{sp} and efficiency η:

$$I_{sp} = \frac{I_{bit}}{\overline{m}_{bit} \cdot g} \tag{9.17}$$

$$\eta = \frac{I_{bit}^2}{2 \cdot E \cdot \overline{m}_{bit}} \tag{9.18}$$

with earth's gravitational acceleration, g= 9.81 m/s^2, the discharge Energy, E, and the average mass bit, $\overline{m}_{bit}$. The results of these calculations are summarized in Table 9.6.

In general, the performance parameters for the thruster using Teflon compare very well to similar thruster types. For comparison, the EO-1 has a specific impulse of 1400 s at 56 J discharge energy with a thruster efficiency of 8%. The unusually low ablation rate for the 10 J case is attributed to an observed slight carbonization of the Teflon ablation surface (see Chapter 7).

The specific impulse and the efficiencies for water are several factors higher than for Teflon. This result is attributed to a more efficient coupling of energy into the plasma, the lower average mol weight for water (6g/mol) compared to the average mol weight of Teflon (31 g/mol), and to the controlled supply of the mass bit in the case of the water thruster, avoiding therefore the significant late time mass losses inherent in Teflon thrusters.

The impulse bit values given in Table 9.6 are based on the impulse bit measurements and the correction factor calculated for Teflon (Chapter 9.5). As outlined in Chapter 9.6, the higher Mach number for the water case indicates a higher correction factor for water. This would imply that the impulse bit values for water, as given in Table 9.6, underestimate the correct value.

Discharge energy [J]	Impulse bit, GRC [μN-s]		Impulse bit, Pressure probe [μN-s]		Mass bit [μg/discharge]		Specific impulse [s]		Efficiency	
	Teflon	Water	Teflon	Water	Teflon	Water	Teflon	Water	Teflon	Water
10	122	--	124	47	11.9	~ 1.64	1060	2920	6.5	6.7
20	273	--	281	90	27.5	~ 1.64	1040	5600	7.2	12.3
30	440	--	440	128	35.3	~ 1.64	1270	7960	9.1	16.6

Table 9.6: Thruster performance for the water and Teflon mode

Fig. 9.12 summarizes the thrust-to-power ratios for the Teflon and water thruster as a function of the specific impulse as predicted by MACH2, the analytic model, and those found experimentally. Also included is the degree of ionization as predicted by MACH2 and assumed by the analytic model respectively.

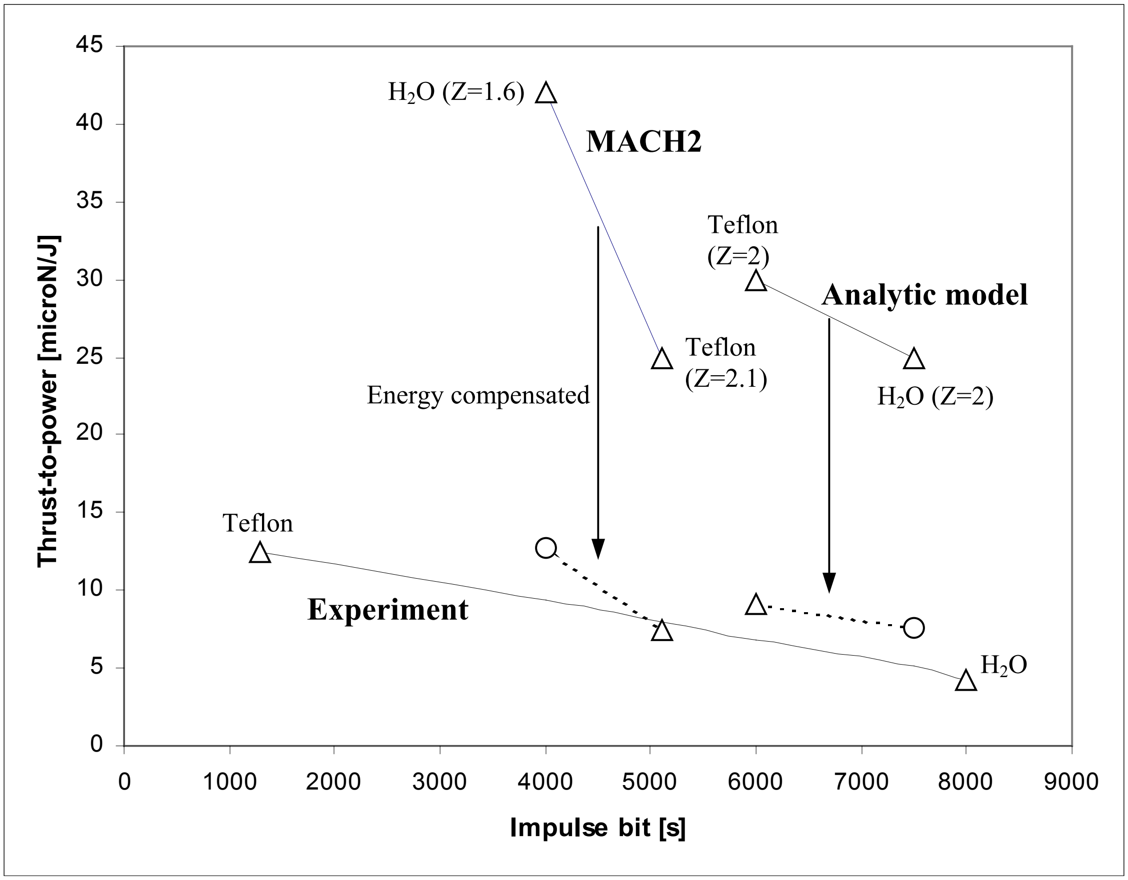

Fig. 9.12: Comparison of thrust-to-power rations prediction from MACH2 and the idealized analytic model with experimental results

Certain important "operational" conditions in the theoretical calculations, such as discharge energy and current waveform, differ significantly from those present in the experiments. For example, while the discharge energies for the experiments in the present work varied between 10 and 30 Joules, they were in excess of 100 Joules for the MACH2 and the analytic model calculations. However, exploiting the linear dependency of the thrust-to-power ratios to the discharge energy, the results from the analytic and numeric calculations can be scaled down to the energies present in the experiment (see Fig. 9.12)

The experimental values for water and Teflon show an anticipated trend, namely higher specific impulse for the lower average molecular weight propellant. A comparison between the specific impulse values for water and Teflon demonstrates the potential of the water fed Pulsed Plasma Thruster. Water shows an improvement in specific impulse of more than a factor 6 compared to the Teflon case. This translates into a significant reduction of the required amount of propellant or, alternatively, into an increase of lifetime expectancy for a satellite system.

The results from MACH2 and the analytic model agree with each other for Teflon, but not for water. As discussed earlier, this is partially attributed to the inadequacy of assumptions made in the development of the analytic model (see discussion in Chapter 4). The high thrust-to-power ratio/low specific impulse predicted by MACH2 for water in comparison to that for Teflon might be attributed to the numerical modeling of the propellant feed. MACH2 models the water "ablation" in a fashion similar to the case of Teflon, only with different material properties.

As mentioned above, a comparison between both the numerical and analytic results with the experimental ones is complicated by significantly different conditions. A more detailed and accurate comparison between experimental results and those predicted by MACH2 would require changing the input parameters for MACH2, such as the discharge current waveform and discharge energy, to match the present experiment.

9.9 Summary

A comprehensive investigation of a Pulsed Plasma Thruster using water as propellant has been conducted. The dominant acceleration processes were identified and compared to a thruster using the traditional Teflon propellant. Magnetic field measurements have proven the electromagnetic nature of the PPT using water. By employing an impact pressure probe, the impulse bit of the water PPT was evaluated. The accuracy of this unique method was verified with a Teflon thruster by comparing impulse bit measurements conducted on a thrust stand at the NASA Glenn Research Center with the impulse bit derived from impact pressure measurements in the plume. These measurements again confirm the electromagnetic nature of the water PPT.

It was found that the observed lower discharge currents for the water thruster, in comparison with the Teflon thruster, are due to a decrease in plasma conductivity. However, in spite of the lower discharge currents, it was shown that the exhaust velocities for the water thruster exceeded those of the Teflon thruster. Evaluation of the rate of change in magnetic field and the associated current density has shown that the current sheet in the case of the water thruster has significant higher velocities, explaining the observed higher exhaust velocities. A comparison of the energy deposited into resistive heating of the plasma for water and Teflon showed that much more energy per unit mass of propellant is utilized for means of acceleration in the case of water, explaining partially the experimentally evaluated higher exhaust velocities.

The following simple calculation demonstrates the improved propellant utilization efficiency of the water thruster: the indicated peak exhaust velocities for Teflon and water are on average around 50 km/s and 80 km/s, respectively. Using these velocities and the evaluated impulse bits, one can evaluate the mass bits necessary to produce the observed impulse bit. For Teflon (30 J discharge energy) this results in a necessary mass bit of 9μg/discharge. This is only 25% of the total mass loss per discharge, a result which correlates well with estimates, made previously[9] and indicates poor propellant utilization efficiency. On the other hand, repeating this calculation for water, one obtains a value of 2 μg/discharge, agreeing well with the measured mass flow of 1.64 μg/discharge and indicating therefore vastly improved propellant utilization efficiency.

A performance evaluation for the water thruster was conducted and compared with the thruster using Teflon as propellant. A significant increase in specific impulse, combined with efficiencies nearly a factor of 2 higher than for the Teflon thruster, emphasizes the potential of water as propellant for Pulsed Plasma Thrusters in general and the value of the developed water PPT in particular.

CHAPTER 10

CONCLUSIONS

Experimental efforts were initiated to investigate physical phenomena and the performance of a Pulsed Plasma Thruster utilizing water as propellant. A hybrid Pulsed Plasma Thruster was designed, fabricated, and subsequently investigated. This thruster type can utilize alternatively water or Teflon without major changes in thruster geometry or circuitry.

A unique propellant feed system was developed in order to supply the discharge with the necessary amount of propellant. The feed system employs a Passive Flow Control (PFC) concept based on the diffusion of the water propellant through a porous ceramic inlay. Studies have been performed to investigate different porous materials with regard to their suitability and the influence of their geometry on the obtained mass flow rate.

Synchronization issues between triggering the main discharge and supplying the propellant were avoided by supplying the water into the vicinity of the spark plug, from where it is delivered into the acceleration channel upon triggering the spark plug.

Extensive diagnostics were performed to investigate unambiguously the influence of utilizing water as propellant for a PPT by direct comparison of the measurement results obtained for Teflon with those obtained with water.

A unique method to evaluate the impulse bit of the PPT by measuring the impact pressure in the plume was developed. The accuracy of this method was verified by direct comparison with impulse bits measured on a thrust stand at the NASA Glenn Research Center. Magnetic field measurements and the performed analytics have clearly shown that the water thruster is indeed an electromagnetic thruster. Time-of-Flight measurements employing Langmuir probes and pressure probes have shown that the velocity of the expelled water plasma is a factor of 1.5 to 2 higher than observed in the Teflon case, although the discharge currents in the water case are around 40% lower.

Evaluation of the plasma conductivity disclosed the reason for the low discharge currents inherent in the water thruster: the water discharge exhibits a plasma conductivity about a factor of 3 - 4 lower than in the case of Teflon. The reasons for the lower conductivity are yet unknown and require further investigation.

In spite of the lower discharge currents, the measurements of all the employed diagnostic methods show consistently higher exhaust velocities obtained with water in comparison with Teflon, due to a more efficient deposition of energy into kinetic energy. This, along with the apparent prevention of late time mass losses, results in a superior performance of the water-fed Pulsed Plasma compared to a Teflon thruster.

CHAPTER 11

FUTURE WORK RECOMMENDATIONS

Accurate mass bit evaluations are essential for evaluation of the thruster performance. The above discussed evaluation of the water mass bit was not performed during thruster operation. During thruster operation, thermal effects might change the mass flow rate and therefore the mass bit. It is therefore important to develop a procedure allowing the evaluation of the water mass bit during operation. Also, the mass flow rate evaluation showed that the processes in the porous are more complicated than suggested by the simple one dimensional form of Darcy’s law. For a better understanding of the flow processes through porous materials and optimization of the PFC element, further investigations are necessary.

As discussed above, impulse bits were evaluated on the basis of pressure probe measurements. Although the impulse bits for the Teflon case, evaluated from the pressure probe measurements, agree very well with those measured on a thrust stand at the NASA GRC, it has to be emphasized that this was not done for the water thruster. As the existence of different Mach numbers in the plume of the Teflon and the water thruster already suggests, it is reasonable to assume that changes in the plasma composition (water vs. Teflon) may require a different correction factor for the pressure probe measurements. Future measurements of the impulse bit of the water thruster on a thrust stand are therefore an important issue for correlation with the pressure probe measurements and a more accurate evaluation of the water thruster performance.

The hybrid thruster geometry was chosen such that it allows a comparison with other existing PPT systems, rather than for an optimized performance for the propellants. Several measurements indicate that for the water propellant this geometry is surely not optimized. In particular, the evaluation of the discharge current density distribution showed that the acceleration process is still ongoing even after the bulk part of the plasma passed through the thruster's exit plane. This indicates, of course, an inefficient acceleration, which could be easily improved by employing longer electrodes. Further promising changes would include a variation of the electrode gap to width ratio and the location of propellant injection.

REFERENCES

[1] Jahn, R.G., Physics of Electric Propulsion, McGraw- Hill Book Company, New York, 1968

[2] Sackheim, R. and Byers, D., “Status and Issues Related to in-Space Propulsion Systems”, Journal of Propulsion and Power, Vol. 14, No. 5, 1998

[3] Guman, W.J. and Nathanson, D.M., “Pulsed Plasma Microthruster Propulsion Systems for Synchonous Orbit Satellite, Journal of Spacecraft”, Vol. 7, No. 4, pp 409-415, Dec. 1970

[4] Guman, W.J. and Williams, T.E., “Pulsed Plasma Microthruster for Synchronous Meterorological Satellite (SMS)”, AIAA-73-1066, Nov. 1973)

[5] Brill, Y., Eisner, A. and Osborn, L., “The Flight Application of a Pulsed Plasma Microthruster; The Nova Satellite”, AIAA-82-1956, July 1982)

[6] Ebert, W.L., Kowal, S.J. and Sloan, R.F., “Operational Nova Spacecraft Teflon Pulsed Plasma Thruster System”, AIAA-89-2497, July 1989

[7] Benson, S.W., Arrington, L.A., Hoskins, W.A. and Meckel, N.J., “Development of a PPT for the EO-1 Spacecraft”, AIAA-99-2276, June 1999

[8] Guman, W.J. and Peko, P.E., “Solid-Propellant Pulsed Plasma Microthruster Studies”, Journal of Spacecraft and Rockets, Vol. 6, No. 6, pp 732-733, 1968

[9] Vondra, R.J., Thomassen, K.I. and Solbes, A., “Analysis of Solid Teflon Pulsed Plasma Thruster”, Journal of Spacecraft, Vol. 7, No. 12, Dec. 1970

[10] Vondra, R.J. and Thomassen, K.I., “Performance Improvements in Solid Fuel Microthruster”, J. of Spacecraft, Vol. 9, No. 10, 1972

[11] Solbes, A. and Vondra, R.J., “Performance Study of a Solid fuel-Pulsed Electric Microthruster”, J. of Spacecraft and Rockets, Vol.10, No. 6, pp 406-410, 1973

[12] Palumbo, D.J. and Guman, W.J., "Effects of Propellant and Electrode Geometry on Pulsed Ablative Plasma Thruster Performance", J. of Spacecraft, Vol.13, No. 3, March 1976

[13] Spanjers, G.G., McFall, K.A., Gulczinski III, F.S. and Spores, R.A., "Investigation of Propellant Inefficiencies in a Pulsed Plasma Thruster", AIAA-96-2723, JPC, July, 1996

[14] Spanjers, G.G., Lotspeich, J.S., McFall, K.A. and Spores, R.A., "Propellant Losses Because of Particulate Emission in a Pulsed Plasma Thruster", Journal of Propulsion and Power, Vol. 14, No. 4, July-August 1998

[15] Arrington, L.A., Haag, T.W., Pencil, E.J. and Meckel, N.J., "A Performance Comparison of Pulsed Plasma Thruster Electrode Configuration", IEPC-97-127, 25th IEPC, 1997

[16] Spanjers, G.G., Malak, Leiweke, R.J. and Spores, R.A., "Effect of propellant Temperature on Efficiency in the Pulsed Plasma Thruster", Journal of Propulsion and Power, Vol. 14, No. 4, July-August 1998

[17] Okada, M., Okawa, Y. and Tachibana, T., "Double Discharge Operation for Pulsed Plasma Thrusters", IEPC-01-156, 27th IEPC, Oct., 2001

[18] Antonsen, E.L., Burton, R.L. and Englman, S.F., "Herriott Cell Interferometry for Unsteady Density Measurements in Small Length Scale Thruster Plasmas" AIAA-00-3431, Huntsville, AL, 2000

[19] Antonsen, E.L., Burton, R.L., Spanjers, G.G. and Spores, R.A., "Microsecond Timescale Surface Temperature Measurements in Micro–Pulsed Plasma Thrusters", AIAA-03-5167, 39th JPC, Huntsville, Alabama, July 2003

[20] Leiweke, R.J., Turchi, P.J., Kamhawi, H. and Myers, R.M., "Experiments with Multi-Material Propellants in Ablation-Fed Pulsed Plasma Thrusters", AIAA 95-2916, 31st JPC, San Diego, 1995

[21] Pencil, E.J., Kamhawi, H., Arrington, L.A. and Warren, W.A., "Evaluation of Alternate Propellant for Pulsed Plasma Thruster", IEPC-01-147, 27th IEPC, Pasadena, CA, 2001

[22] Ziemer, J.K., Choueiri, E.Y. and Birx, D., "Trends in Performance Improvements of a Coaxial Gas-Fed Pulsed Plasma Thruster", IEPC-97-040, 25th International Electric Propulsion Conference, Cleveland, OH, 1997

[23] Ziemer, J.K., Choueiri, E.Y. and Birx, D., "Comparing the Performance of Co-Axial and Parallel-Plate Gas-Fed PPTs", IEPC-99-209, 26th International Electric Propulsion Conference, Kitakyushu, Japan, 1999

[24] Ziemer, J.K. and Petr, R.A., "Performance of Gas_Fed Pulsed Plasma Thruster Using Water Vapor Propellant", AIAA-2002-4273, 38th JPC, July, 2002

[25] Koizumi, H. Kakami A., Furuta, Y., Komurasaki, K. and Arakawa, Y., "Liquid Propellant Pulsed Plasma Thruster", IEPC-03-087, 28th International Electric Propulsion Conference, Toulouse, France, 2003

[26] Kakami, A., Koizumi, H., Komurasaki, K. and Arakawa, Y., "Performance Study on Liquid Propellant Pulsed Plasma Thruster", 39th Joint Propulsion Conference, Huntsville, AL, 2003

[27] Winter, B.A., "U.S. Space Station Freedom Waste Gas Disposal System Trade Study", Journal of Propulsion and Power, pp. 873-877, Vol.8, No.4, July-Aug. 1992

[28] Wilms, J., Hinueber, A., Nentwig, G. and Auweter-Kurtz, M. "Conceptual Design of a Synergistic Propulsion System for the International Space Station", IEPC-01-170, 27th IEPC, California, USA, 2001

[29] Tacina, R.R., "Space Station Freedom Resistojet System Study", Journal of Propulsion and Power, pp. 694-702, Vol.5,No.6, Nov-Dec. 1989

[30] Lewis, J., Matthews, M.S., Guerrieri, M.L., Resources of Near-Earth Space, University of Arizona Press, 1993

[31] Hirata, M. and Murakami, H., "Exhaust Gas Analysis of a Pulsed Plasma Engine", IEPC 84-52, 1984, Tokyo

[32] Yiangos George Mikellides, "Theoretical Modeling and Optimization of Ablation-Fed Pulsed Plasma Thrusters", Dissertation, The Ohio State University, 1999

[33] Corey, R.L., "Numerical Analysis of the Effect of Propellant Material Properties on Pulsed Plasma Thruster Performance" Thesis, The Ohio State University, 2000

[34] Scharlemann, C.A., Corey, R., Mikellides, I.G., Turchi, P.J. and Mikellides, P.G., "Pulsed Plasma Thrusters Variations for Improved Mission Capabilities", AIAA-00-3260, 36th AIAA Joint Propulsion Conference, July 2000, Huntsville, Alabama

[35] Peterkin, R.E. and Frese, M.H., "MACH2: A Reference Manual", 5th edition, July 1992, Weapons Laboratory, Kirtland Air Force Base, NM

[36] Mikellides, P.G., Turchi, P.J. and Roderick, N.F., "Theoretical Modeling of Magnetoplasmadynamic Arcjets" IEPC-93-189, 23rd International Electric Propulsion Conference, Seattle, WA, Sep. 1993

[37] Leiweke, R.J. and Mikellides, P.G., "An Ablation Algorithm for the Non-Ideal MHD Code, MACH2", Report sponsored by NASA Glenn Research Center, Electric Propulsion Lab, Cleveland, Dec. 1996

[38] Kamhawi, H. and Turchi, P.J. Design , Operation, and Investigation of an Inductively-Driven Pulsed Plasma Thruster, AIAA 98-3804, 34th Joint Propulsion Conference, Cleveland, OH, 1998

[39] Antropov, N., Diakonov, G., Lapayev, O. and Popov, G., "Laboratory Investigation of Pulsed Plasma Thrusters with Gas Valves", Micropropulsion for Small Spacecrafts, Progress in Astronautics and Aeronautics, Vol. 187, American Institute of Aeronautics and Astronautics Inc., 2000

[40] Scharlemann, C.A. and York, T.M., "Investigation of a PPT Utilizing Water as Component Propellant", IEPC-03-112, International Electric Propulsion Conference, March 2003, Toulouse, France

[41] Scharlemann, C.A. and York, T.M. "Pulsed Plasma Thruster Using Water Propellant, Part I: Investigation of Thrust Behavior and Mechanism" AIAA-03-5022, 39th AIAA Joint Propulsion Conference, Huntsville, Alabama, July 2003

[42] Eckbreth, A.C., "Current Pattern and Gas Flow Stabilization in Pulsed Plasma Accelerators" Dissertation, Princeton Universtiy, 1969

[43] Berkery, J.W. and Choueiri, E.W., "Characterization of Current Sheet Evolution in a Pulsed Electromagnetic Accelerator", IEPC-03-307, International Electric Propulsion Conference, Toulouse, France, 2003

[44] Burton R. and Bushman S., "Probe Measurements in a Coaxial Gas Dynamic PPT", AIAA-99-2288, June 1999

[45] Guman, W.J. and Begun, M., "Exhaust Plume Studies of a Pulsed Plasma Thruster",,AIAA-78-704, 13th IEPC, San Diego, California, 1978

[46] Eckman, R., Gatsonis, N.A., Myers, R.M. and Pencil,, E.J., "Experimental Investigation of the LES 8/9 Pulsed Plasma Thruster", IEPC-97-126, IEPC, 1997

[47] Kamhawi, H., Pencil, E. and Haag, T., "High Thrust-to-Power Retangular Pulsed Plasma Thruster" AIAA-2002-3975, Joint Propulsion Conference, Indianapolis, Indiana, 2002

[48] Byrne, L.T., "Langmuir Probe Measurements in the Plume of a Pulsed Plasma Thruster", Master Thesis, Worcester Polytechnic Institute, 2002

[49] Johnson E.O, Malter, L., Physical Review, Vol. 80, 1950

[50] Huddlesstone, R.H. and Leonard, S.L, Plasma Diagnostic Techniques, Academic Press, New York, 1965

[51] Chen, F.F., Plasma Physics and Controlled Fusion, 2nd ed., 1984 Plenum Press

[52] Analysis of Solid Teflon Pulsed Plasma Thruster, R. J. Vondra, K. Thomassen and A. Solbes, Journal of Spacecraft, Vol. 7, No. 12, Dec. 1970

[53] Hargus, W.A. and Cappelli, M.A., "Pressure Measurements in the Plume of a Low Power Arcjet Nozzle", AIAA-95-2818, 31st JPC, 1995

[54] Netwig, G., "Experimental and Theoretical Investigation on an Arc Heated Water Steam Plasma", Proceedings of 14th International Symposium on Plasma Chemistry, Prague, Czech Republic, 1999

[55] T.M. York, "Stress Dynamics in High Speed Piezoelectric Pressure Probes", Review of Scientific Instruments, Vol. 41, No. 4, April 1970

[56] Michels, C.J. and York, T.M., "Pressure Measurements in the Exhaust of a Pulsed Megawatt MPD Arc Thruster", AIAA-71-196, 1971

[57] Anderson Jr., J.D., Modern compressible flow, 2nd edition, McCraw-Hill, 1990

[58] Haag, T. W., "Thrust Stand for Pulsed Plasma Thrusters," Rev. Sci. Instrum., 68 (5), 1997

[59] Spitzer, Jr., L, Physics of Fully Ionized Gases, Interscience Publishers, Inc., New York, 1956

[60] Pullin, D.I., Davis, J. and Harvey, J.K., "Monte Carlo Calculations of the Rarefied Transition Flow Past a Bluff Faced Cylinder", Paper 133, 10th International Symposium on Rarefied Gas Dynamics, Aspen, CO, July 1976

[61] Boyd, T.J.M. and Sanderson, J.J., The Physics of Plasmas, Cambridge University Press, 2003